

Magnetic nanostructures by atom optics

Citation for published version (APA):

Smeets, B. (2005). *Magnetic nanostructures by atom optics*. [Phd Thesis 1 (Research TU/e / Graduation TU/e), Applied Physics and Science Education]. Technische Universiteit Eindhoven. <https://doi.org/10.6100/IR597973>

DOI:

[10.6100/IR597973](https://doi.org/10.6100/IR597973)

Document status and date:

Published: 01/01/2005

Document Version:

Publisher's PDF, also known as Version of Record (includes final page, issue and volume numbers)

Please check the document version of this publication:

- A submitted manuscript is the version of the article upon submission and before peer-review. There can be important differences between the submitted version and the official published version of record. People interested in the research are advised to contact the author for the final version of the publication, or visit the DOI to the publisher's website.
- The final author version and the galley proof are versions of the publication after peer review.
- The final published version features the final layout of the paper including the volume, issue and page numbers.

[Link to publication](#)

General rights

Copyright and moral rights for the publications made accessible in the public portal are retained by the authors and/or other copyright owners and it is a condition of accessing publications that users recognise and abide by the legal requirements associated with these rights.

- Users may download and print one copy of any publication from the public portal for the purpose of private study or research.
- You may not further distribute the material or use it for any profit-making activity or commercial gain
- You may freely distribute the URL identifying the publication in the public portal.

If the publication is distributed under the terms of Article 25fa of the Dutch Copyright Act, indicated by the "Taverne" license above, please follow below link for the End User Agreement:

www.tue.nl/taverne

Take down policy

If you believe that this document breaches copyright please contact us at:

openaccess@tue.nl

providing details and we will investigate your claim.

Magnetic Nanostructures by Atom Optics

PROEFSCHRIFT

TER VERKRIJGING VAN DE GRAAD VAN DOCTOR AAN DE
TECHNISCHE UNIVERSITEIT EINDHOVEN, OP GEZAG VAN
DE RECTOR MAGNIFICUS, PROF.DR.IR. C.J. VAN DUIJN,
VOOR EEN COMMISSIE AANGEWEEZEN DOOR HET COLLEGE
VOOR PROMOTIES IN HET OPENBAAR TE VERDEDIGEN OP
WOENSDAG 26 OKTOBER 2005 OM 16.00 UUR

DOOR

BART SMEETS

GEBOREN TE LOMMEL, BELGIË

DIT PROEFSCHRIFT IS GOEDGEKEURD DOOR DE PROMOTOREN:

PROF.DR. K.A.H. VAN LEEUWEN

EN

PROF.DR. H.C.W. BEIJERINCK

COPROMOTOR:

PROF.DR. P.VAN DER STRATEN

Druk: Universiteitsdrukkerij Technische Universiteit Eindhoven

Ontwerp omslag: Paul Verspaget

CIP-DATA LIBRARY TECHNISCHE UNIVERSITEIT EINDHOVEN

Smeets, Bart

Magnetic nanostructures by atom optics / door Bart Smeets. -

Eindhoven : Technische Universiteit Eindhoven, 2005 . - Proefschrift.

ISBN 90-386-2331-3

NUR 926

Trefw.: atoombundels / deeltjesoptica / laserkoeling / lithografie / magnetische dunne lagen / nanotechnologie

Subject headings: atomic beams / particle optics / laser cooling / lithography / magnetic thin films / nanotechnology

Contents

1	Introduction	3
1	Lithography	3
2	Magnetic nanostructures	4
3	Principles of atom lithography	4
4	Laser cooling	6
5	The choice of element	9
6	Contents of this thesis	12
7	Outlook	12
2	Experimental setup	17
1	Laser setup	18
2	Vacuum setup	24
3	Conclusions	27
3	Laser frequency stabilization using an Fe-Ar hollow cathode discharge cell	29
1	Introduction	30
2	Hollow Cathode Discharge Cell	31
3	Absorption Spectroscopy	32
4	Laser locking by polarization spectroscopy	34
5	Conclusions	38
4	Laser cooling simulation based on the semiclassical approach	41
1	Introduction	42
2	Theory	43
3	Implementation of the semiclassical model	46
4	Results	48
5	Concluding remarks	50
5	Laser collimation of an Fe atomic beam on a leaky transition	55
1	Introduction	56
2	Experimental setup	57
3	Simulations	60
4	Results and Discussion	63
5	Conclusions	66

6	Fe nanolines without laser cooling	69
1	Introduction	70
2	Theory	70
3	Simulation	73
4	Experimental setup	74
5	Results	76
6	Magnetic properties of nanolines	79
7	Conclusions	81
7	Efficient blue light generation in Rb	85
1	Introduction	86
2	Theoretical framework	87
3	Setup	88
4	Results and discussion	89
5	Conclusions	93
	Summary	95
	Samenvatting	97
	Dankwoord	99
	Curriculum Vitae	100

Chapter 1

Introduction

1 Lithography

Fifty years ago, a computer was a room-sized device; nowadays, we carry our computer with many orders magnitude increase in computing power and storage capacity around in a small bag. All this is due to the continuous effort to develop techniques that decrease the size of electronic components [1].

The most successful technique is optical lithography. Using a light beam a pattern in a mechanical mask is transferred to a substrate through a multistep process of exposing a resist layer, developing the resist, and plasma etching. Nowadays, structures as small as 45 nm can be produced this way [2]. Although very demanding on optics and special UV light sources, optical lithography allows large-scale production of nanoscale patterns, making it the workhorse for the semiconductor industry. However, structure size is diffraction-limited by the wavelength of the light used. To make even smaller patterns in the future, EUV light sources emitting light at 13 nm and EUV optics are developed. The development of such systems constitutes very challenging and costly efforts [3].

In general, charged-particles lithography has been developed, using electrons or ions to write the desired pattern. Because the de Broglie wavelength of these particles is sub-nanometer, these techniques can be used to write even smaller structures, only limited by the Coulomb repulsion forces between the charged particles. The throughput is much lower compared to optical lithography, making it unsuitable for large scale production. Nevertheless, special applications like the use of e-beam lithography in the production of patterned masks used in optical lithography, make charged-particle lithography essential. In the early 90s, neutral atoms were used for the first time for nanostructure fabrication [4]. This was a consequence of the fast development of new ways to manipulate neutral atoms with light. Neutral atoms do not suffer from Coulomb repulsion. Although the de Broglie wavelengths of thermal atoms are much longer than those of keV ions, they are considerably below a nanometer. In neutral atom lithography, the patterning of the atom beam is not achieved by a mechanical mask like in optical lithography but through a structured light field. Two approaches have been used in atom lithography. First, atoms with internal energy (metastable atoms) can be used to expose resists layers in a way very similar to optical lithography [5]. Second, the atoms in the patterned beam can be simply deposited on a surface, thus directly growing nanostructures. This

technique is called direct-write atom lithography, or laser-focused deposition. The proof of principle was provided with sodium [6, 7]. But soon, a number of technologically interesting elements were used: chromium [8–11], aluminum [12], ytterbium [13], and experiments are ongoing with gallium [14], indium [15], and silicon [16]. Direct-write atom lithography is attractive, as it allows sub-100 nm structures to be fabricated in a single-step process in a simple setup. Furthermore, using a standing light wave as a mask, it allows periodic structures to be grown with unparallel accuracy. A unique possibility offered by direct-write atom lithography is structured doping, in which a patterned atomic beam is codeposited together with a second unperturbed atomic species in order to obtain nanostructured doping concentration. The technique as used so far also has considerable limitations, e.g., with a simple standing light wave as structuring light field only regular line or dot grids are possible and throughput is very low. However, the advantages can be exploited in niche applications like novel devices with structured doping, calibration samples for atomic force microscopes, etc.. In our group, working on laser manipulation of atomic beams, we have chosen to produce magnetic nanostructures with atom lithography.

2 Magnetic nanostructures

Miniaturization of magnetic structures has led to the discovery of several fascinating and technologically relevant physical effects. Information storage industries are exploiting these new phenomena to sustain the ongoing increase in storage capacity of magnetic media. Also, new fundamental physics can be explored on these small scales. For example, giant magnetoresistance, current-induced switching, and spin-injection have led to the exciting possibility to use the electron spin in information storage and processing, or spintronics. It is highly desirable not only to produce nanostructures but also to fabricate arrays of nanostructures over macroscopic areas. Ordered magnetic nanostructures are particularly interesting to study, since one can not only study their individual properties but also their collective behavior in a well-defined and reproducible way. They are also important technologically in applications like magnetic random access memory (MRAM) and recording media.

Fabrication of arrays of nanostructures with an unprecedented periodicity over macroscopic scales is exactly what can be done with atom lithography. An advantage of atom lithography is the ability to dope a layer with a nanoscale-modulated concentration of other elements [17], allowing for the production of novel structures with spatially modulated magnetic properties. For a review on magnetic nanostructures, see [18].

3 Principles of atom lithography

In atom lithography, an atomic beam is patterned by a light field. The atoms are focussed by certain regions of the light field onto a substrate, transferring the pattern. The fundamental principle of laser focussing is illustrated in Fig. 1.1. A collimated beam of atoms is forced to travel through an intense standing light wave. The atoms will interact with the electric field if the frequency of the light is detuned close to the resonance frequency

of the atoms. The energy of this electric dipole interaction is given by:

$$U_{dip} = -\frac{\alpha(\omega)}{2\epsilon_0 c} I, \quad (1.1)$$

with I the light intensity, and $\alpha(\omega)$ the dynamic polarizability at the frequency ω of the light. Only close to an atomic resonance α is large enough in order for the dipole energy to have an effect; however, if ω is too close to an atomic resonance spontaneous emission (resonance fluorescence) occurs and Eq. 1.1 is not valid anymore.

The light intensity of a standing light wave, which is produced by two counter-propagating Gaussian laser beams in the x -direction, is given by:

$$I(x) = I_0 \sin^2(kx) e^{-\frac{2(y^2+z^2)}{\omega^2}}, \quad (1.2)$$

with $k = 2\pi/\lambda$ the wavenumber of the light. The standing wave contains regions where the intensity of the light changes rapidly over small distances. These intensity gradients lead to energy gradients and thus to forces on the individual atoms. Depending on the detuning of the light, atoms are attracted towards regions of low light intensity ($\Delta > 0$) or high intensity ($\Delta < 0$).

As a consequence, the standing light wave acts as an array of microlenses. Atoms entering the standing light wave are focused on a focal plane beyond the standing light wave. A substrate may be placed in the focal plane and the increased atomic deposition rate at the focal spots results in the growth of a structure with the periodicity of the standing light wave.

The first proposal of laser focussing an atomic beam was made by Balykin and Lethokov back in 1987 [19]. The first experimental realization was in 1992 by Timp *et al.* [6] with sodium, closely followed by the NIST group, which made the first chromium lines [8].

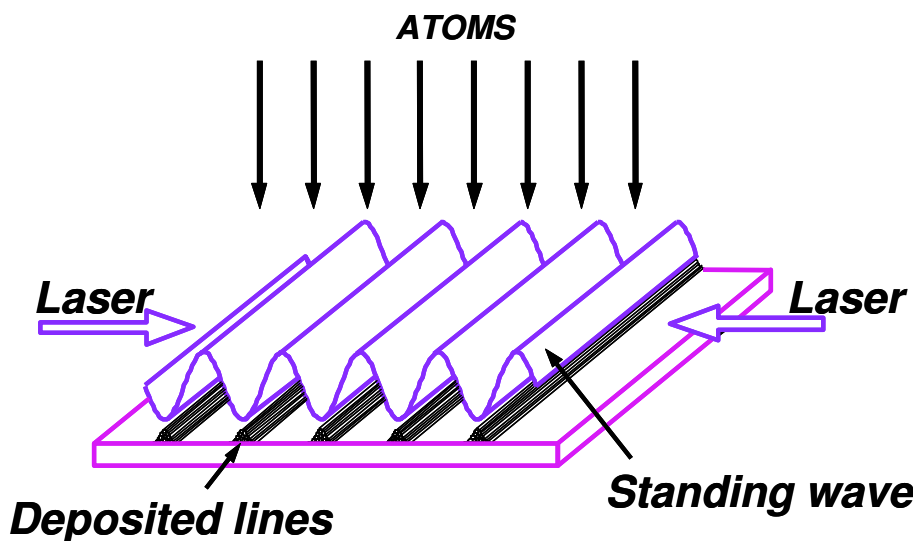


Figure 1.1: Individual atoms are travelling through a standing light wave. They are focused to the regions with lowest intensity. [8]

Structures formed with a 1D standing light wave have a period of half the wavelength of the light used. More complex laser fields can generate structures with a smaller periodicity. With a $\pi^x\pi^y$ laser field structures with a periodicity of $\lambda/8$ were realized [20]. By interfering more than two laser beams, also 2D structures were obtained [21–23].

In analogy with light optics, tight focusing requires a locally collimated beam, i.e., the angular spread of atoms arriving at a specific position on the lenses must be small. Transverse collimation of an atomic beam can be obtained by two slits. Any desired degree of collimation can be obtained this way, but flux loss is unavoidable. Laser cooling provides a solution by cooling the atomic beam in the direction perpendicular to the atomic beam. In this approach, a strong degree of collimation can be achieved without flux loss, since the transverse velocity spread of the atom is actively decreased to very small values by the laser cooling process. Laser cooling has been applied to achieve sufficient beam collimation in all direct-write atom lithography experiments so far.

4 Laser cooling

Because of the importance of beam collimation in the lithography experiment, a large part of this thesis will deal with laser cooling of neutral iron atoms. Laser cooling is a well known technique to collimate atomic beams and cool trapped atoms. Achievements like Bose Einstein condensation of atoms (BEC), atom interferometers, and ultracold plasmas would not be possible without the use of laser cooling [24]. The simplest idea behind laser cooling is that resonant light can exert a dissipative force on neutral atoms. Intuitively this can be illustrated in the following way (Fig. 1.2). An atom moving in a light field absorbs a photon, the momentum of the photon is transferred to the atom, giving it an extra momentum of $\hbar\mathbf{k}$. Here \mathbf{k} is the wavevector of the photon with $|k| = 2\pi/\lambda$. After some time the excited atom will decay back to the ground state, spontaneously emitting a photon in an arbitrary direction, with the atom absorbing the recoil momentum. The ground state atom can then be excited again. After many of these cycles, the recoil momenta of the spontaneous emitted photons average to zero. This leaves the atom with the momentum kicks of the absorbed photons, which are directed along the laser beam. The force is then equal to the momentum of the photon $\hbar k$ times the absorption rate.

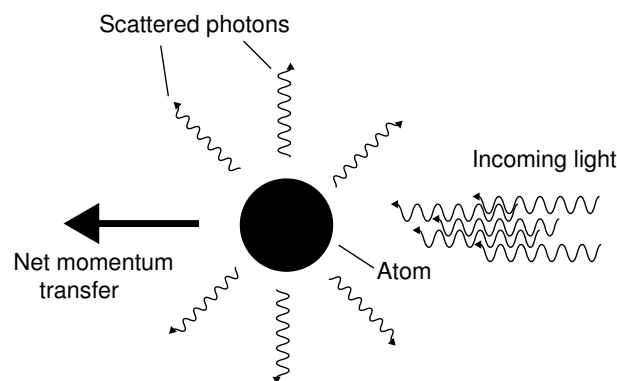


Figure 1.2: Principle of light forces. Absorbed photons from the laser beam are spontaneously re-emitted in random directions. The net momentum transfer is in the direction of the laser beam.

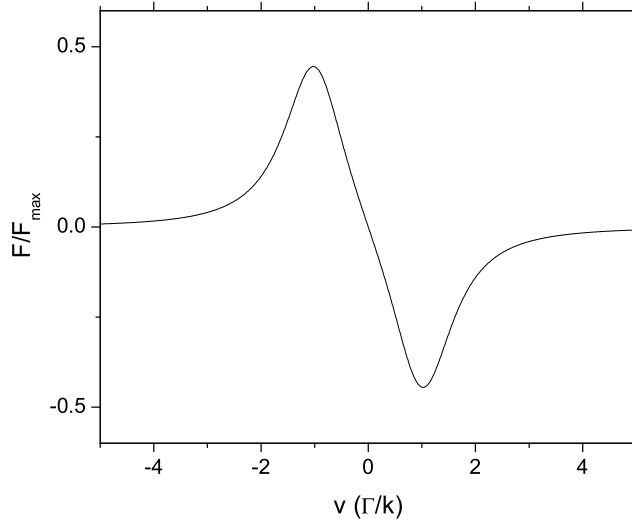


Figure 1.3: The total force on an atom resulting from two counter-propagating red-detuned laser beams as a function of the transverse velocity of the atom.

Since the maximal absorption rate is half the natural linewidth, the maximum average force exerted on the atom in this way is $F = \hbar k \Gamma / 2$ with $\Gamma = 1/\tau$ and τ the lifetime of the excited state.

When an atom moves, it sees the laser frequency Doppler shifted by $\delta = -\mathbf{k} \cdot \mathbf{v}$ with \mathbf{v} the velocity of the atom. In the case of iron with an excited state lifetime of 62 ns and a laser wavelength of $\lambda = 372$ nm, it takes a velocity change of 1 m/s to take the atom out of resonance with the light. This velocity dependence is the basis of laser cooling. This was first proposed by Wineland and Dehmelt [25], and by Hänsch and Schawlow [26]. An atom moves in a standing wave, which consists of two counter-propagating laser beams of slightly red-detuned light. It sees the counter-propagating light wave (with respect to its own motion) more blue-detuned, thus closer to resonance compared to the co-propagating light wave. This gives a dispersively shaped profile of force versus velocity (Fig. 1.3):

$$F = F_+ + F_-, \quad (1.3)$$

where F_+ and F_- are the forces from both of the light waves, given by:

$$F_{\pm} = \pm \hbar k \frac{\Gamma}{2} \frac{s}{1 + s + (2\delta_{\pm}/\Gamma)^2}, \quad (1.4)$$

with $s = I/I_0$ the saturation parameter.

Near zero velocity, the atom experiences a slowing force proportional to its own speed, which strongly damps the motion of the atom with a friction coefficient α . Due to the friction the width of the velocity distribution of an ensemble of atoms in such a laser field will be seriously narrowed. When this distribution is Gaussian, in the one-dimensional case a temperature $T = M \langle v^2 \rangle / k_B$ can be attributed to the ensemble. When the velocity

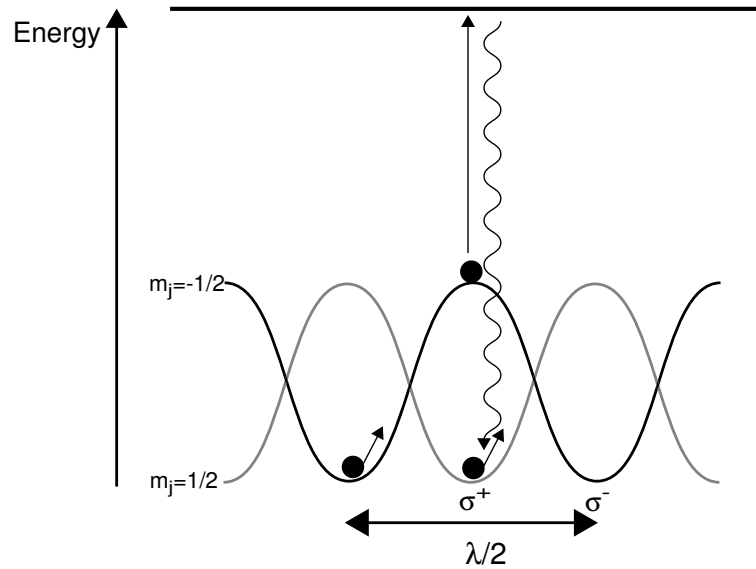


Figure 1.4: In a light field of two counter-propagating light beams with orthogonal linear polarization, the light shifts of the ground states depend strongly on the position of the atom due to the spatial polarization gradient.

distribution narrows, the temperature decreases and the atoms are cooled. This cooling is limited by the heating from the random spontaneously emitted photons, which is described by a diffusion coefficient D in velocity space. The lowest temperature that can be reached is called the Doppler temperature and is given by $k_B T_D = 2D/\alpha = \hbar\Gamma/2$.

At first, experiments on laser cooling confirmed this limit [27]. However, in following experiments much lower temperatures were measured [28]. For the explanation of these results the existing Doppler cooling theory was inadequate. Soon, new theoretical models were developed which could explain these sub-Doppler temperatures [29]. Both for the experimental realization of such low temperatures and for the theoretical framework, Cohen-Tannoudji, Chu, and Phillips received the Nobel Prize in 1997. The basic physical effect behind these ultra-low temperatures is the energy shift of the electronic levels in an atom due to a resonant light field. This light shift is called the AC Stark shift $\hbar\Omega = \sqrt{\omega_R^2 + \Delta^2}$, with ω_R the Rabi frequency, which is proportional to the square root of the laser intensity. A gradient in laser intensity can thus exert a force on atoms. When the atom has more than two levels, e.g., in case of magnetic degeneracy of the ground and excited state of the atom, these forces can be used to cool atoms. The light shifts of each magnetic sublevel in a polarized light field not only depends on the intensity but also on the local polarization of the light. Hence, a spatial polarization gradient will exert a force on the atoms in such a light field. One well known case is the $\pi^x\pi^y$ configuration. The counter-propagating light fields have orthogonal linear polarization and the polarization changes from σ_+ to σ_- in half a wavelength. This is illustrated in Fig. 1.4. For a $J=1/2$ to $J=3/2$ transition in a σ_+ light wave, which induces $\Delta m=1$ transitions, the magnetic sub-level $m=1/2$ is the most light shifted: its coupling with the excited state is the largest. For a detuning below resonance an atom in that state has the lowest internal energy. When the atom moves the polarization will change, hence, the internal energy

will increase. Since the total energy is constant, this can only happen at the expense of kinetic energy; the atom is slowed down. At this point, there is a chance that the atom is pumped to the excited state and decays back to the other $m = -1/2$ ground state in the region of σ_- light. This state now has the lowest energy, and the energy difference has been carried away by the spontaneously emitted photon. By repeating this process many times, the atom is further decelerated. Since the friction coefficient of this force is independent of laser intensity and the diffusion by spontaneous emission increases linearly with laser intensity, the temperature can be decreased indefinitely in a model where the velocity changes are infinitely small. However, when the width of the momentum distribution is comparable to the momentum of a single photon recoil, the discreteness of the velocity changes prevents further decrease in temperature. This limit is called the recoil limit. The cooling described above is called Sisyphus cooling.

Another well known cooling scheme uses two counter-propagating laser beams of orthogonal circular polarization, where the extra force arises from an imbalance in the radiation pressure from both beams [29]. For all these mechanisms, the recoil limit is the ultimate cooling limit.

5 The choice of element

We have chosen to apply direct-write atom lithography to a ferromagnetic element (see Section 2). At room temperature, the choice is mainly limited to three elements: Fe, Co, and Ni. Their properties are listed in Table I.

Crucial in atom lithography is the ability to laser cool and focus the atoms. For this purpose an atomic transition should be present which is easily accessible with current lasers. Cobalt fails to meet this criterium. A continuous wave laser with a wavelength of 240 nm is very difficult to make. Furthermore a huge amount of intensity is needed since this transition in Co is very strong. Also, Co has hyperfine structure, which limits the percentage of atoms that interact with the light: only 12% of the atoms at a temperature of $T=2000$ K are in the true ground state. Comparing Fe and Ni, Fe has the advantage that the atomic transition can be accessed by a frequency doubled Titanium:Sapphire laser, where for Ni a frequency doubled dye laser must be used, which imposes more technical difficulties. On the other hand, the atomic transition in Fe has a leak, which means atoms are pumped out of the ground state during interaction with the light. The material properties are in favor of Fe, since the melting point of Fe is almost 100 K higher than the melting point of Ni while it reaches 10^{-1} Torr vapor pressure at a slightly lower temperature than Ni. Therefore, we have accepted the disadvantage of the leaky transition and chosen Fe to perform our experiment.

In Fig. 1.5 the fine-structure of the relevant energy levels of Fe is shown. For laser cooling and focusing the ${}^5D_4 \rightarrow {}^5F_5$ optical transition at a wavelength of $\lambda=372$ nm is used. From the excited state, decay is also possible to the metastable 5F_5 , 5F_4 , and 3F_4 states emitting light at a wavelength of $\lambda=501.3$ nm, 512.9 nm, and 671.2 nm, respectively. The total leak rate is $1/244$ the total decay rate of the excited state. At a temperature of $T=2000$ K, the atoms are thermally excited mainly to all 5D states: only 50 % of the atoms remain in the 5D_4 state.

Table I: Properties of the ferromagnetic elements Fe, Co, and Ni.

	Fe	Co	Ni
magnetic properties			
atomic magn. moment (μ_B)	4	3	2
bulk phase magn. moment (μ_B)	2.2	1.7	0.6
bulk phase crystal structure	bcc	hcp	fcc
Curie temperature (K)	1044	1393	628
isotopes			
Z	26	27	28
most abundant	^{56}Fe 92%	^{59}Co 100%	^{58}Ni 68%
other isotopes	^{54}Fe 6% ^{57}Fe 2%		^{60}Ni 26% ^{62}Ni 4% ^{61}Ni 1% ^{64}Ni 1%
material properties			
melting point (K)	1811	1768	1728
boiling point (K)	3134	3200	3168
T(K) @ 10^{-1} Torr vapor pressure	1920	1960	1970
surface energy (J/m^2)	2.9	2.7	2.5
atomic properties			
electron conf.	$3d^6 4s^2$	$3d^7 4s^2$	$3d^8 4s^2$
ground state conf.	5D_4	$^4F_{9/2}$	3F_4
ground state J	4	9/2	4
nuclear spin I	0 (^{56}Fe)	7/2 (^{59}Co)	0 (^{58}Ni)
ground state population @ 2000 K	50%	12%	70%
atomic transition from ground state			
transition	$^5D_4 \rightarrow ^5F_5$	$^4F_{9/2} \rightarrow ^4G_{11/2}$	$^3F_4 \rightarrow ^3G_5$
wavelength (nm)	372.0	240.5	323.4
Γ upper state (Mrad/s)	16.2	360	7.3
saturation intensity I_s (W/m^2)	62	5156	43
leak rate	1:243	0	0

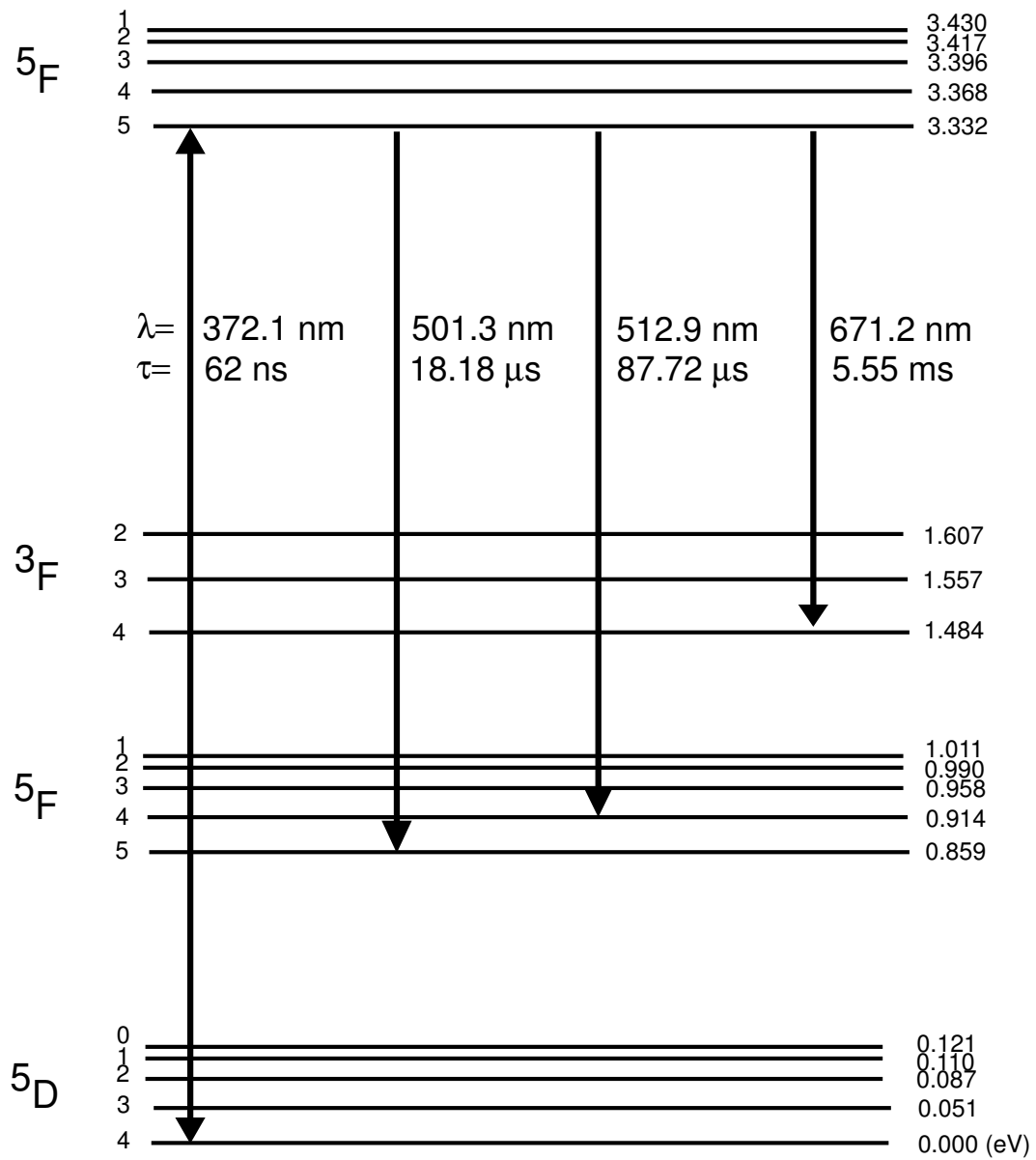


Figure 1.5: Energy-level diagram of Fe, showing the fine-structure of the relevant states.

6 Contents of this thesis

In this thesis all necessary steps on the road to fabrication of nanostructures with atom lithography and the fabrication itself are investigated. This includes locking of the ultra-violet laser, laser cooling, and the actual production of magnetic nanolines.

In Chapter 2, the experimental setup is discussed. For the production of Fe nanostructures with atom lithography in a clean environment an ultra high vacuum system is constructed. This system includes a high temperature atomic beam source and a specially designed sample holder and load-lock system. A UV laser system is installed to cool and focus the Fe atoms, including a frequency doubler.

The UV laser needs to be locked to the correct atomic transition in Fe. In Chapter 3 the locking of the UV laser by polarization spectroscopy using an Fe-Ar hollow cathode discharge is discussed. Neutral iron atoms with a high enough density to perform spectroscopy are sputtered from the cathode surface. By means of polarization spectroscopy, a Doppler-free dispersive signal is generated on which the laser is locked.

In Chapter 4, the theme is semiclassical calculations of laser cooling. The velocity distribution follows from the numerical integration of the Fokker-Planck equation. This method is compared with Quantum Monte-Carlo and rate equation calculations. The validity of the method is investigated for high recoil parameters.

Measurements on the laser collimation of a thermal iron beam are described in Chapter 5. Laser cooling on the 372 nm $^5D_4 \rightarrow ^5F_5$ transition of ^{56}Fe is complicated due to leaks to metastable states. The effect of the leak on the collimation and the obtained flux is investigated. Measurements are compared with different simulations.

In Chapter 6 we show that it is also possible to produce nanolines without laser cooling, despite the (qualified) success of the laser cooling experiments, as well as preliminary production of nanolines with a laser-cooled beam [30]. In fact, it is the first time atom lithography is reported without use of laser cooling techniques to collimate the atomic beam. We simply rely on the geometrical collimation properties of the Fe atomic beam in our vacuum setup. This result is of considerable importance for the field of atom lithography as it opens the way for the production of nanostructures of a wide variety of non-laser cooled elements. Preliminary measurements of the magnetic properties of the produced Fe nanolines are discussed.

In Chapter 7, a novel up-conversion process based on atomic coherence is investigated. The experiment is performed at the University of Melbourne. Efficient blue light generation is obtained by lasing-without-inversion in Rb, reaching much higher blue output power than previously reported. This is a potential mechanism for producing new wavelength coherent light sources, especially in the blue and ultraviolet region.

7 Outlook

In Ref. [31] and this thesis the development of an experimental setup for the fabrication of nanostructures by atom lithography is described. During the past four years every aspect of the experimental setup is studied in depth, making it clear that the spectroscopic properties of iron are not ideal for atom-optics experiments like laser cooling. With

this in mind, the most important result we achieved is the production of iron nanolines without use of laser cooling techniques. This clears the road for atom lithography of other technologically interesting elements like gallium, indium, and silicon, which are, as iron, very hard to laser cool. Serious effort has been put in to obtain collimated atomic beams of these elements, including multiple-step frequency doubling and the use of repumping lasers. We showed that the fabrication of nanostructures with atom lithography can be done without all these experimentally demanding steps.

By skipping the laser cooling stage, time spent on developing the experiment can decrease from more than four years to a time schedule that leaves room to do research on fundamental applications of atom lithography. Development of the laser cooling stage can be done afterwards to improve the quality of the nanostructures.

The most promising application is definitely structured doping, where two or more species are deposited at the same time, but only one 'feels' the standing light wave and is density modulated on nanometer scale over macroscopic areas with unprecedented periodicity. In particular, we are interested in structured doping of ferromagnetic elements with iron. The development of highly periodic magnetic doping would result in magnonic crystals, nanometer scale spin filters [32], etc., and would be of great interest in magneto-electronic applications.

References

- [1] G.L. Timp, editor. *Nanotechnology*. Springer-Verlag, Heidelberg (1999).
- [2] specifications for ASML TWINSCAN XT:1700i.
- [3] International Technology Roadmap for Semiconductors (ITRS), <http://www.itrs.net/Common/2004Update/2004Update.htm>.
- [4] D. Meschede and H.J. Metcalf, *J. Phys. D: Appl. Phys.* **36** R17 (2003).
- [5] K. S. Johnson, J. H. Thywissen, N. H. Dekker, K. K. Berggren, A. P. Chu, R. Younkin, and M. Prentiss, *Science* **280**, 1583 (1998).
- [6] G. Timp, R.E. Behringer, and D.M. Tennant, J.E. Cunningham, *Phys. Rev. Lett.* **69**, 1636 (1992).
- [7] V. Natarajan, R.E. Behringer, and G. Timp, *Phys. Rev. A* **53**, 4381 (1996).
- [8] J.J. McClelland, R.E. Scholten, E.C. Palm, and R.J. Celotta, *Science* **262**, 877 (1993).
- [9] U. Drodofsky, J. Stuhler, B. Brezger, Th. Schulze, M. Drewsen, T. Pfau, and J. Mlynek, *Microelectron. Eng.* **35**, 285 (1997).
- [10] R. Gupta, J.J. McClelland, Z.J. Jabbour, and R.J. Celotta, *Appl. Phys. Lett.* **67**, 1378 (1995).
- [11] U. Drodofsky, J. Stuhler, Th. Schulze, M. Drewsen, B. Brezger, T. Pfau, and J. Mlynek, *Appl. Phys. B: Photophys. Laser Chem.* **65**, 755 (1997).

- [12] R.W. McGowan, D.M. Giltner, and S.A. Lee, *Opt. Lett.* **20**, 2535 (1995).
- [13] R. Ohmukai, S. Urabe, and M. Watanabe, *Appl. Phys. B*, **77**, 415 (2003).
- [14] S.J. Rehse, K.M. Bockel, and S.A. Lee, *Phys. Rev. A* **69**, 063404 (2004).
- [15] H. Leinen, D. Glässner, H. Metcalf, R. Wynands, D. Haubrich, and D. Meschede, *Appl. Phys. B*, **70**, 567 (2000).
- [16] T. Fujii, H. Kungai, K. Midorikawa, and M. Obara, *Opt. Lett.*, **25**, 14571459 (2000).
- [17] Th. Schulze, T. Muther, D. Jurgens, B. Brezger, M.K. Oberthaler, T. Pfau, J. Mlynek, *Appl. Phys. Lett.* **78**, 1781 (2001).
- [18] J.I. Martin, J. Nogués, Kai Liu, J.L. Vicent, I.K. Schuller, *J. Magn. Magn. Mater.* **256**, 449 (2003).
- [19] V.I. Balykin and V.S. Lethokov, *Opt. Comm.* **64**, 151 (1987).
- [20] R. Gupta, J.J. McClelland, P. Marte, and R.J. Celotta, *Phys. Rev. Lett.* **76**, 4689 (1996).
- [21] R. Gupta, J.J. McClelland, Z.J. Jabour, and R.J. Celotta, *Appl. Phys. Lett.* **67**, 1378 (1995).
- [22] U. Drodofsky, J. Stuhler, Th. Schulze, M. Drewsen, B. Brezger, T. Pfau, and J. Mlynek, *Appl. Phys. B* **65**, 755 (1997).
- [23] E. Jurdik, G. Myszkiewicz, J. Hohlfeld, A. Tsukamoto, A. J. Toonen, A. F. van Etteger, J. Gerritsen, J. Hermsen, S. Goldbach-Aschemann, W. L. Meerts, H. van Kempen, and Th. Rasing, *Phys. Rev. B* **69**, 201102 (2004).
- [24] H.J. Metcalf and P. van der Straten, *Laser Cooling and Trapping*, Springer-Verlag New York (1999).
- [25] D.J. Wineland and H. Dehmelt, *Bull. Am. Phys. Soc.* **20**, 637 (1975).
- [26] T.W. Hänsch and A.L. Schawlow, *Opt. Comm.* **13**, 68 (1975).
- [27] S. Chu, L. Hollberg, J.E. Bjorkholm, A. Cable, and A. Ashkin, *Phys. Rev. Lett.* **55**, 48 (1985)
- [28] P. Lett, R. Watts, C. Westbrook, W.D. Phillips, P. Gould, and H. Metcalf, *Phys. Rev. Lett.* **61**, 169 (1988).
- [29] J. Dalibard and C. Cohen-Tannoudji, *J. Opt. Soc. Am. B* **6**, 2023 (1989).
- [30] E. te Sligte, B. Smeets, K. M. R. van der Stam, R. W. Herfst, P. van der Straten, H. C. W. Beijerinck, and K. A. H. van Leeuwen, *Appl. Phys. Lett.* **85**, 4493 (2004).
- [31] E. te Sligte, *Atom Lithography of Iron*, Ph.D. thesis, TU/e (2005).

- [32] K.N. Altmann, N. Gilman, J. Hayoz, R.F. Willis, and F.J. Himpsel, Phys. Rev. Lett. **87**, 137201 (2001).

Chapter 2

Experimental setup

In this chapter an overview of the experimental apparatus is given. To produce nanostructures by atom lithography, the demands on both the laser setup as well as the vacuum part are high. A UV laser is needed with an output power of at least 100 mW and frequency stabilized to within 0.2 MHz of an adjustable frequency close to the atomic resonance. To deposit high quality Fe layers and structures, a high-intensity Fe atomic beam is produced and the deposition is performed under UHV conditions. A more detailed description of different parts of the setup is given in other chapters of this thesis.

1 Laser setup

In order to laser cool and focus Fe atoms, a laser system capable of producing at least 100 mW at 372 nm is needed. Since no commercial laser has this capability at the moment, we opted for frequency doubling a commercially available Coherent 899-21 Titanium:Sapphire laser tuned to 744 nm.

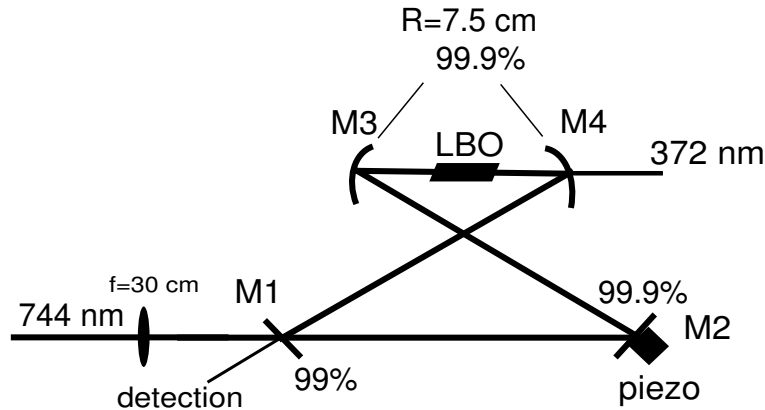


Figure 2.1: A schematic view of the frequency doubler. The length of the folded cavity is approximately 61.5 cm. The LBO crystal is placed in between two curved mirrors with radius of curvature $R=7.5$ cm. The input beam is coupled into the cavity by a $f=30$ cm lens. For best mode matching, the cavity should be placed such that the waist of the focused input beam is in between mirrors M1 and M2. At that position, the input beam is also focused exactly in the center of the LBO crystal between mirrors M3 and M4. The LBO-crystal is Brewster cut to minimize reflections. Mirror M2 is mounted on a piezo stack for scanning the cavity over 10 FSR or approximately 5 GHz.

1.1 Frequency doubling

In this wavelength range the best choice for a frequency doubling crystal is definitely Lithium Triborate (LBO). An LBO-crystal of length 10 mm has a power conversion efficiency η , defined by:

$$\eta = \frac{P_{\omega}^2}{P_{2\omega}} \quad (2.1)$$

of $1.5 \times 10^{-4} \text{ W}^{-1}$ [1], with P_{ω} the power in the fundamental frequency and $P_{2\omega}$ the power in the second harmonic. Since a Ti:S laser typically produces 1 W at 744 nm, 0.15 mW UV light can be obtained in this way which is a factor of 10^3 less than what we need. To overcome this problem, the LBO crystal is placed inside a ring cavity. In Fig. 2.1 a schematic view of the frequency doubler is shown [2]. The cavity has a finesse of approximately 200. In theory, we obtain an intra-cavity power of 100 times the input power, which would enable us to produce a factor 100^2 more UV-power (Eq. 2.1). A more realistic example is given in Fig. 2.2, measured with our frequency doubler. Here, the power conversion efficiency has increased to $\eta=0.22 \text{ W}^{-1}$ using a ring cavity. To avoid moisture sticking on the crystal it is heated to approximately 50 °C. An oxygen atmosphere surrounds the crystal during pumping, suppressing the diffusion of oxygen out of the LBO-crystal while pumping it at high intra-cavity light intensity.

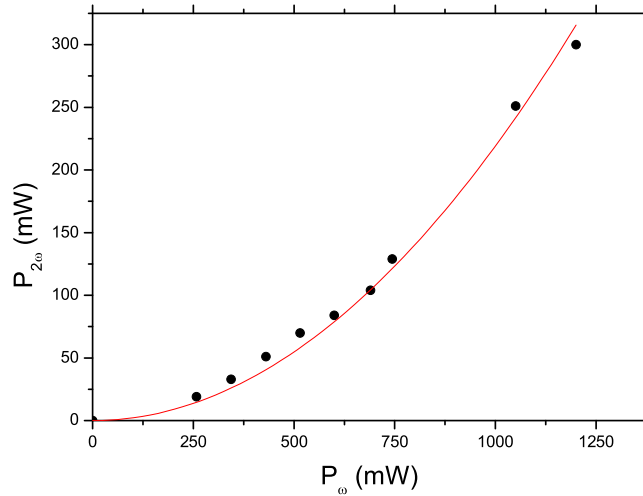


Figure 2.2: The UV-output power as a function of the IR-input power of the cavity enhanced frequency doubling.

1.2 Locking

Locking the frequency doubler

In order to build up intra-cavity power, the cavity needs to be resonant with the pumping laser. A common method used for locking a cavity is Pound-Drever-Hall (PDH) locking [3]. This technique is based on the dependence of the cavity reflection on the laser frequency. On resonance, the reflected light intensity is minimal. When the laser frequency is phase-modulated, the frequency difference from resonance can be determined by measuring the phase shift of the reflected power compared to the modulation. When both signals are in phase the laser is tuned above cavity resonance, when they are out of phase the laser is tuned below cavity resonance. Mixing the modulation and reflected power signal results in a dispersive error signal. This explanation holds for low-frequency modulation, in the PDH-scheme the mechanism is different but the result is the same. The laser can be locked to a cavity or the other way around: the cavity on the laser frequency. It is the latter option we use since the laser frequency needs to be scanned independently while keeping the doubling cavity locked to its frequency.

In our case the input light is phase-modulated with 20 MHz creating small sidebands, which are coupled into the cavity together with the unperturbed frequency. The modulation is created by an electro-optical modulator (EOM) which consists of a crystal of which the refractive index is modulated by applying an electric field. This modulation of the refractive index influences the phase of the light travelling through. The spectrum of the modulated signal shows the fundamental and two adjacent sidebands spaced from the carrier by the modulation frequency. Mixing the reflection from mirror M1 (see Fig. 2.1) with the modulation frequency results in a dispersive error signal, which is used for locking by a PI-controller. In Fig. 2.3 the cavity transmission with sidebands and the

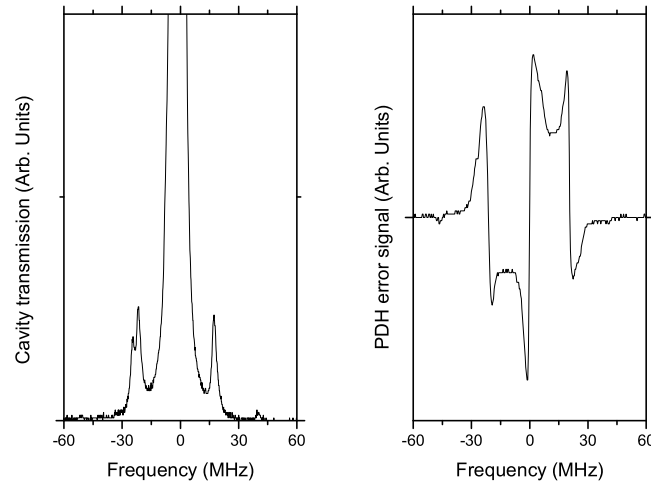


Figure 2.3: Cavity transmission (*left*) and error signal (*right*). The frequency is scanned by moving mirror M2 using the piezo stack.

resulting error signal are shown.

A second locking scheme, which we currently use, is called Hänsch-Couillaud (HC) locking [4]. In this scheme a cavity is locked without the use of any modulation making the electronics much simpler. HC-locking is based on polarization rotations inside the cavity. In the HC-scheme, a linear polarizer is placed inside a confocal cavity. Its transmission axis forms a small angle with the polarization of the incoming laser beam. We can decompose the electric field vector of the incoming light in a component parallel to the transmission axis of the polarizer and a component perpendicular to this axis. Since the perpendicular component is not transmitted, it is simply reflected by the first mirror. The parallel component sees a cavity with almost no loss and experiences a frequency dependent phase shift upon reflection. The phase shift between the components will make the resulting reflected beam elliptically polarized. The ellipticity is measured by a $\lambda/4$ -wave plate and a polarizing beamsplitter (PBS) cube. By rotating the fast axis of the wave plate under 45° with respect to the axis of the PBS, the elliptically polarized light, which essentially is a superposition of two counterrotating circularly polarized light beams with different amplitudes, is decomposed into two orthogonal polarized light beams, which are spatially separated by the PBS-cube. The intensity of both beams is measured with a photodiode. The subtraction of the photodiode outputs results in a dispersive signal. In our cavity, no linear polarizer is present. However, since an LBO-crystal has different refractive indices for two perpendicular polarization orientations, a linear polarized light beam travelling through the crystal with a small polarization mismatch with respect to this orientation will become elliptically polarized. Analyzing the reflection from mirror M1 with a $\lambda/4$ -wave plate and a polarizing beam splitter cube (PBS), a dispersive signal is obtained, which can be used for locking. Although both PDH- and HC-schemes lock the cavity equally well, the advantage of the HC-locking scheme is that no frequency

modulation is needed to provide an error signal. Typically we can lock our cavity such that output power fluctuations are lower than 5 %.

Laser locking on an atomic reference

For optimal laser cooling and focusing, the laser should remain on the same frequency with a stability below the natural linewidth of iron ($\Gamma=2.58(2\pi)$ MHz) during the course of the experiment, which can take a couple of hours. Commonly, spectroscopy on gas cells is used to lock lasers. These gas cells are heated to obtain a high enough neutral atom density. For alkali-atoms this works well, since they have high vapor pressures at modest temperatures. For iron, reaching sufficient density would mean heating a gas cell to temperatures as high as 1500 °C, which would impose serious technical difficulties. As an alternative we opted for a hollow cathode discharge cell. Such a cell consists of a hollow cathode made of iron. An argon discharge is created and the ions sputter neutral iron atoms from the surface of the cathode creating an Fe vapor. A more in depth discussion can be found in Chapter 3.

The technique used for locking lasers on atomic transitions is saturated absorption spectroscopy. Since an atomic vapor in a gas cell has a certain temperature, absorption of light by the atoms suffers from Doppler broadening. This means that when scanning the frequency of the laser over the resonance frequency of the atoms the resolution is not limited by the natural linewidth of the atomic transition, but by the Doppler broadened linewidth, which can be more than a factor of 100 times larger than the natural linewidth. Saturated absorption spectroscopy can overcome this broadening. A laser with a frequency ω_l addresses atoms with a velocity component v in the direction of the laser beam given by $kv = \omega_l - \omega_a$, with ω_a the atomic resonance frequency and k the wavevector of the light. A counterpropagating laser beam addresses atoms with a velocity v' given by $kv' = \omega_a - \omega_l$. Both laser beams only excite the same velocity group at $v = v' = 0$. At that point the laser is exactly on resonance, $\omega_l = \omega_a$. Due to the fact that both laser beams excite the same atoms, these atoms become saturated which manifests itself in less absorption of the laser beams. When measuring the intensity of one of the laser beams with a photodiode, this saturation shows up as less absorption, thus higher intensity. Since this only happens when the laser is exactly on resonance with a resolution on the order of the natural linewidth of the atom, this saturation can be clearly distinguished from the Doppler broadened absorption profile.

Most of the locking techniques are based on this saturated absorption scheme. A common technique is called polarization spectroscopy, where the counterpropagating laser beams have different polarizations using, e.g., a linearly and a circularly polarized beam. The electric field vector of the linear polarized laser beam can be decomposed in two counterrotating circularly polarized electric fields. Because both circularly polarized components experience different saturation (only one component has a likewise polarization as the saturating beam), the polarization axis of the linear polarized laser beams rotates and becomes slightly elliptical when tuned close to resonance. This rotation and ellipticity can be analyzed with a polarizing beam splitter (PBS) cube. The advantage of polarization spectroscopy is that a dispersive signal is obtained without use of modulation and demodulation techniques. The locking of our laser with this technique is described in

detail in Chapter 3 of this thesis.

1.3 Optical system

General

In Fig. 2.4 a layout of the laser setup is shown. Our Ti:S-laser is pumped by an Ar⁺-laser capable of producing more than 20 W output power. The Ar-ion laser (Coherent Innova 200) lases on two strong lines at 514.5 nm and 488.0 nm. The Ti:S laser (Coherent 899-21) has a tuning range from 700 nm to 1100 nm depending on the optics set used, with the top performance between 750 nm and 800 nm. For our purposes the Ti:S laser is tuned to 744 nm. The laser is coupled to the doubling cavity, which is locked by the Hänsch-Couillaud scheme. To lock the laser on the 372 nm transition in Fe, polarization spectroscopy on a hollow cathode discharge is performed. The laser beam used for laser cooling is expanded by a cylindrical optics telescope consisting of three curved mirrors from a laser beam of waist 1 mm to a beam size of 100×5 mm. Laser cooling is described in detail in Chapter 5. The other part of the laser beam passes through an acousto-optical modulator (AOM). The first order emerging from the AOM is frequency shifted by 150 MHz and is used for creating the standing wave applied to deposit nanostructures (Chapter 6). The fundamental order is used for detection of atoms by light induced fluorescence (LIF).

Light induced fluorescence

The atomic beam is imaged by observing the fluorescence induced by an intense laser beam, which saturates all atoms in the beam 1100 mm downstream from the nozzle of the atomic beam source. The photon scattering rate is given by [5]:

$$\Gamma_p = \frac{\Gamma}{2} \frac{s_0}{1 + s_0 + 4\left(\frac{\delta - \mathbf{k} \cdot \mathbf{v}}{\Gamma}\right)^2}, \quad (2.2)$$

with Γ the natural linewidth, s_0 the on-resonance saturation parameter, $\delta = \omega_l - \omega_a$ the detuning from resonance, \mathbf{k} the wavevector of the light, and \mathbf{v} the velocity of the atoms. The highest scattering rate for all velocity groups is $\Gamma/2$, when $s_0 \gg 4\left(\frac{\delta - \mathbf{k} \cdot \mathbf{v}}{\Gamma}\right)^2$. Since the full-angle divergence of the atomic Fe beam at that point in the vacuum setup is geometrically limited to approximately 4 mrad, and the average longitudinal velocity of the atoms is close to 1000 m/s, the spread in $\mathbf{k} \cdot \mathbf{v}$ amounts to $5(2\pi)$ MHz, which is double the natural linewidth of Fe. When we align the laser perpendicular to the atomic beam and tune it close to resonance $\delta = 0$, all velocity groups are addressed by the laser when $s_0 \gg 4\left(\frac{\delta - \mathbf{k} \cdot \mathbf{v}}{\Gamma}\right)^2 \approx 16$. In our setup s_0 is typically on the order of 1000. The intensity of the resulting fluorescence is than only dependent on the density in the atomic beam. Spatial information is obtained by imaging the fluorescence using a CCD-camera (Apogee Alta U47).

Standing wave light mask

The alignment of the standing light wave is crucial in an atomic lithography experiment and a detailed study of this topic can be found in Ref. [7]. In Fig. 2.5 an example of a well-

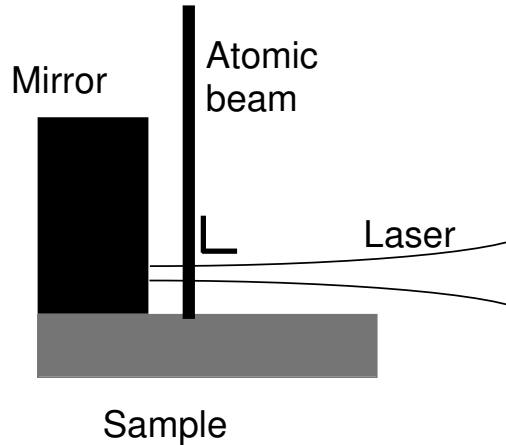


Figure 2.5: A well-aligned deposition setup. The atomic beam should be perpendicular to the standing wave. The substrate should be parallel to the standing wave. The focus of the laser should be positioned on the surface of the mirror to minimize wavefront imperfections.

aligned setup is shown. First of all, the standing wave should be aligned perpendicular to the atomic beam and parallel to the substrate on which we deposit. This is obtained by mounting the mirror, on which the incoming laser beam reflects, perpendicular to the substrate. This results in a standing wave parallel to the substrate within 0.5 mrad. The atomic beam alignment is defined by two apertures: one is the hole in the skimmer and the other is in a dummy sample. With light induced fluorescence we check if the atomic beam passes through the second aperture. Then the vacuum is opened and a HeNe-laser is placed at the position of the atomic beam source. This laser beam is aligned through both apertures and the reflection of the area around the hole in the dummy sample is overlapped with the incoming HeNe-laser beam. This procedure results in an atomic beam which is perpendicular to the substrate within 0.3 mrad.

To create a standing light wave, the UV-laser beam is focused to a beam waist of $50 \mu\text{m}$ ($1/e^2$ intensity radius) by a 200 mm lens. The waist is positioned on the surface of the mirror to obtain the same wavefront curvature for the incoming and reflecting beam by moving the lens such that their sizes are equal at a fixed distance from the mirror. The Rayleigh length of this focus is 16 mm. Since the atomic beam passes the mirror at a distance of 1 mm, wavefront curvature is not a problem.

2 Vacuum setup

In this Section, the most important features of the vacuum setup are summarized. The vacuum system is described in detail in Ref. [7]. To grow high quality Fe nanostructures the deposition needs to be performed under UHV conditions. Our vacuum system consists of four differentially pumped sections shown in Fig. 2.6. In Fig. 2.7 a schematic view of the vacuum setup is shown. The first section is the source chamber, where a bright Fe beam is produced. Typical pressures on the order of $10^{-6} - 10^{-5}$ mbar are reached by pumping with a 100 l/s turbo-molecular pump. To produce a high intensity Fe atomic beam, a vapor pressure on the order of 10^{-1} mbar is necessary, which means for Fe a

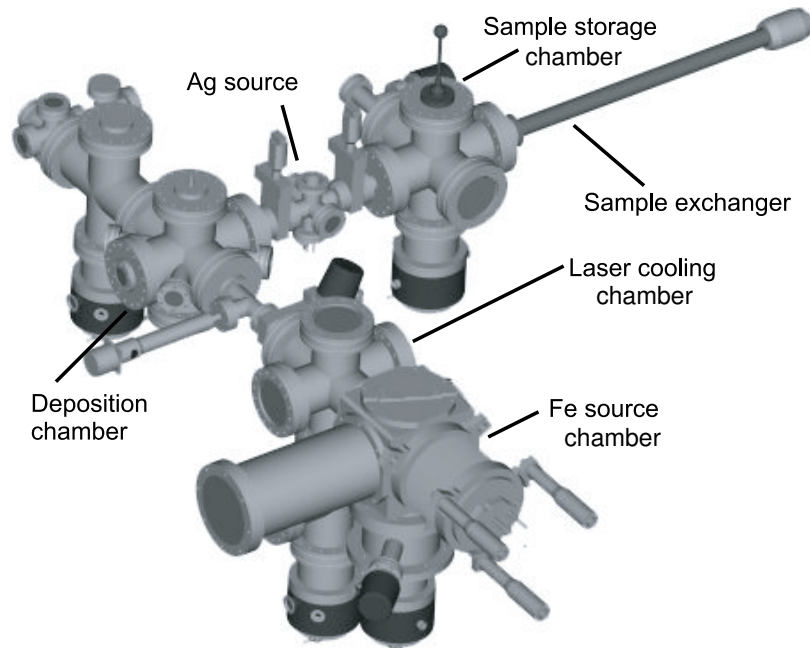


Figure 2.6: Artists impression of the vacuum system. The Fe atoms emerge from the source into the laser cooling section and are deposited in the deposition chamber. The sample holder can be exchanged and stored in a load-lock.

temperature of about 2000 K should be reached. For this purpose an oven is constructed based on a carbon heater [6]. The source is used in thermal mode. A schematic drawing of the oven is shown in Fig. 2.8. To reach a temperature of 2000 K a power of 1000 W has to be supplied to the heater ($R=0.6 \Omega$). As crucible material Al_2O_3 is used which can sustain temperatures up to 2200 K. The Fe beam emerges from a 1 mm diameter nozzle. Tantalum foil is used for heat shielding. The exterior of the oven is water cooled.

The second section is the laser cooling section in which the Fe beam is transversely collimated. Depending on the aperture in-between the source and laser cooling section, pressures on the order of $10^{-8} - 10^{-7}$ mbar are reached using a 250 l/s turbo-molecular pump. Details about the laser cooling setup are given in Chapter 5.

The third section is the deposition chamber, where the sample holder for the atom lithography experiment is mounted. This vessel is separated from the laser cooling chamber by a flow resistance. Pressures on the order of 10^{-8} mbar are obtained by a 250 l/s turbo-molecular pump. In this section the standing light wave for the atom lithography is created. The specially designed sample holder used for this purpose is described in Ref. [7] and in this thesis in Chapter 6.

The sample holder can be exchanged by a magnetic translator and stored in a load lock (Fig. 2.7). A movable storage case with space for four sample holders is constructed. It can be moved up and down under vacuum conditions using bellows. Sample holders are moved in and taken out by the magnetic translator. In Fig. 2.9 the movable storage case and the sample holder are shown. In this load lock pressures of 10^{-8} mbar are reached by using a 230 l/s turbo-molecular pump. A silver evaporation source is included to deposit a capping layer in order to protect the iron from oxidizing. We follow a design of the

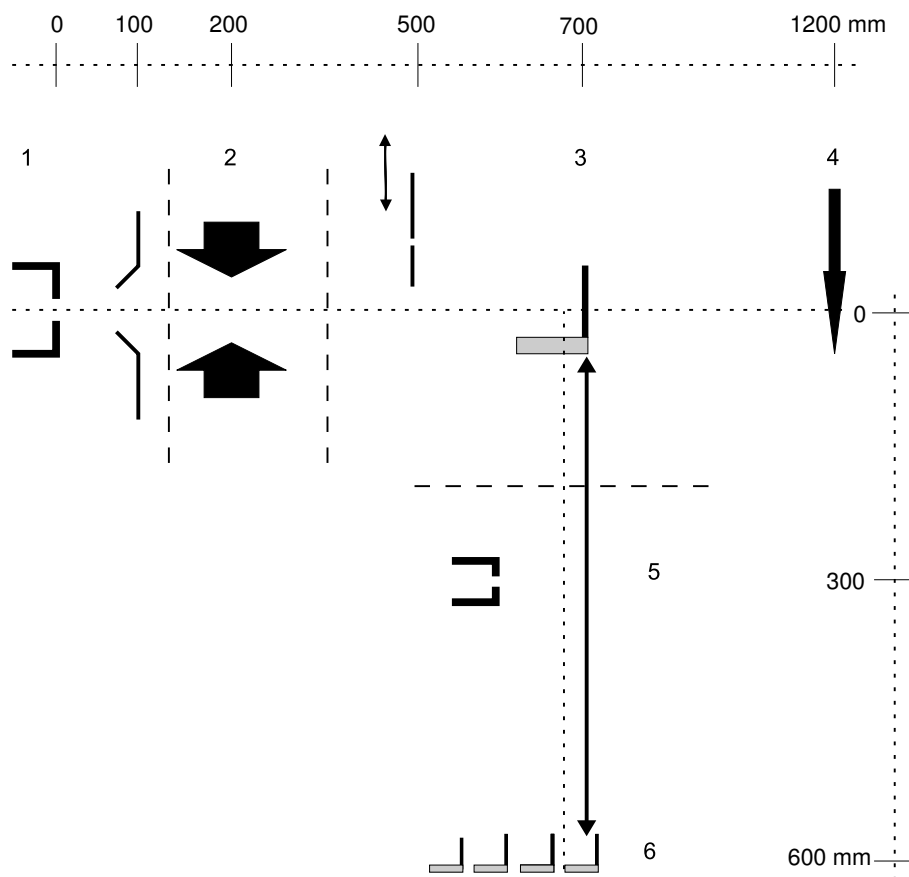


Figure 2.7: Schematic view of the vacuum setup. The differential pump sections are separated by the dashed lines. The Fe atoms emerge from the source (1) into the laser cooling section (2) and are deposited in the deposition chamber (3). The atoms are detected with light induced fluorescence (LIF) (4). The sample holders can be exchanged and stored in a load-lock (6). In between deposition chamber and load-lock the Ag-source is mounted (5). On the top and on the right side, distances are indicated in mm.

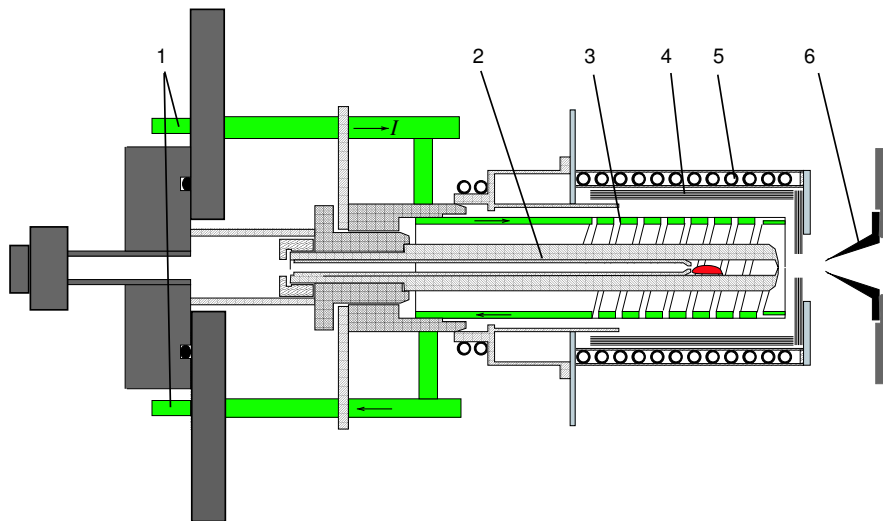


Figure 2.8: The Fe source with copper electrodes (1), Al_2O_3 crucible (2), graphite heater (3), Tantalum heat shielding (4), water cooling (5), and aperture separating source chamber and laser cooling section (6). The source is used in thermal mode.

MMN group from the department of Applied Physics at the TU/e. Silver is contained inside a tungsten crucible, which is heated by 5Ω tantalum filament wound through an alumina spacer. The silver atoms can evaporate from a 2 mm diameter orifice. A K-type thermocouple, spring-pressed to the bottom of the tungsten crucible, measures the temperature. A tantalum heat shield is used and water cooling is applied. The typical operating temperature is 1140 K at a current of 3.5 A through the Ta filament. Deposition speeds of $1.5 \text{ \AA}/\text{min}$ can be reached this way. More details can be found in Ref. [7].

3 Conclusions

In conclusion, a laser system has been constructed, capable of producing up to 300 mW of UV-light at 372 nm by frequency doubling a commercially available Ti:S-laser. Frequency doubling is achieved by an LBO-crystal placed inside a ring cavity. Power conversion efficiencies up to 0.22 W^{-1} are reached this way. The ring cavity can be locked both by the Pound-Drever-Hall as well as by the Hänsch-Couillaud scheme. We have selected the HC-scheme, since it is easier to implement. Laser locking on an atomic reference is performed using polarization spectroscopy. An AOM is used to shift the frequency of the laser by 150 MHz. The frequency-shifted laser beam is used to create the standing light wave for focusing of the atoms.

An UHV-setup is constructed for depositing the Fe nanostructures in a clean environment. A specially designed storage chamber is used to store different samples to ensure deposition of Fe nanostructures on different substrates without opening the vacuum system.

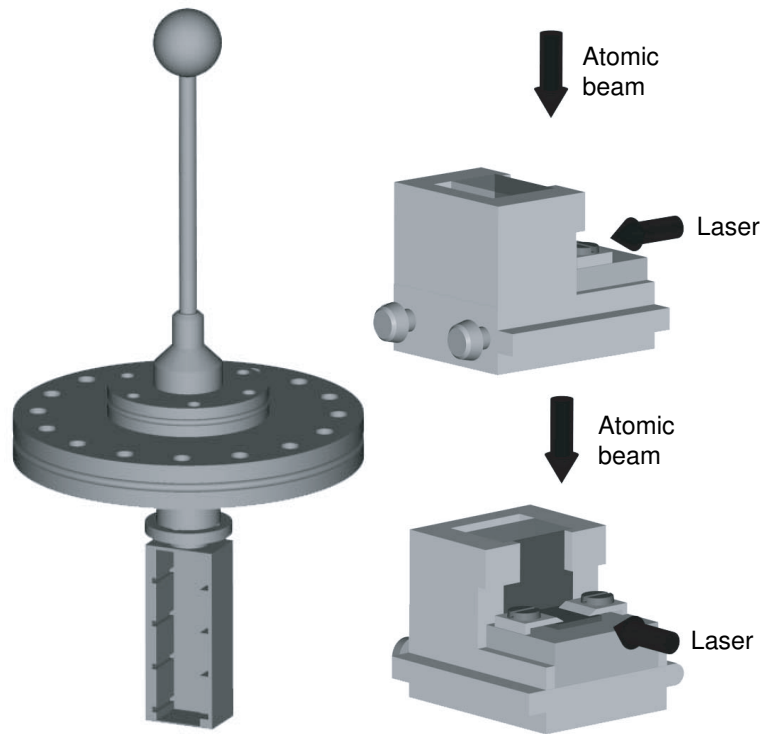


Figure 2.9: *Left*: the storage case for our sample holders. Up to four sample holders can be stored in-vacuo. *Right*: the sample holders. With the two pins on the back of the sample holder, it can be attached to the magnetic translator. The vertical arrows represent the direction of the atomic beam; the horizontal arrows the direction of the laser beam.

References

- [1] R.C.M. Bosch, *Ferromagnetic Nanostructures by Laser Manipulation*, Ph.D. thesis, TU/e (2002).
- [2] The frequency doubler and locking electronics are designed and constructed at the Laser Centre of the Vrije Universiteit Amsterdam, contact: Wim Vassen.
- [3] E. Black, *Notes on the Pound-Drever-Hall Technique*, Internal Technical Note, Laser Interferometer Gravitational wave Observatory Project (LIGO) of CALTECH and MIT (1998).
- [4] T.W. Hänsch and B. Couillaud, *Opt. Comm.* **35**, 441 (1980).
- [5] H.J. Metcalf, and P. van der Straten, *Laser Cooling and Trapping*, Springer Verlag, New York (1999).
- [6] R.C.M. Bosch, H.C.W. Beijerinck, P. van der Straten, and K.A.H. van Leeuwen, *Eur. Phys. J. Appl. Phys.* **18**, 221 (2002).
- [7] E. te Sligte, *Atom Lithography of Iron*, Ph.D. thesis, TU/e (2005).

Chapter 3

Laser frequency stabilization using an Fe-Ar hollow cathode discharge cell

Polarization spectroscopy of an Fe-Ar hollow cathode discharge cell was used to lock a frequency doubled Ti:Sapphire laser to the 372 nm $^5D_4 \rightarrow ^5F_5$ transition of ^{56}Fe . The discharge cell produced a density of 10^{18} m^{-3} ground state ^{56}Fe atoms at a temperature of 650 K, a density comparable to a conventional oven at 1500 K. Saturated absorption spectroscopy and two schemes of polarization spectroscopy were compared with respect to signal-to-background ratio and the effect of velocity changing collisions. The laser was locked within 0.2 MHz for hours by feedback of the dispersive polarization spectroscopy signal.

¹Published as: B. Smeets, R.C.M. Bosch, P. van der Straten, E. te Sligte, R.E. Scholten, H.C.W. Beijerinck, K.A.H. van Leeuwen, *Appl. Phys. B* **76**, 815

1 Introduction

Atom optics experiments often require the ability to lock lasers to the frequency of an atomic transition within an atomic linewidth. To achieve this, a high resolution spectroscopic technique is needed.

In our group, we are investigating direct-write atom lithography of Fe [1]. This technique has been applied successfully to sodium [2, 3], chromium [4–7] and aluminum [8] beams. It has proven to be a very promising technique for the production of regular arrays of nanostructures. In this approach an atomic beam is focused by the interaction with a high intensity, near resonant standing wave. In our experiment, a supersonic Fe atom beam will be used to reduce "monochromatic aberrations" during focusing [9]. Spherical aberration is reduced by collimating the Fe beam to a divergence of $100 \mu\text{rad}$ by laser cooling techniques [10].

The only atomic transition of ^{56}Fe that can be used for laser focusing and cooling is the $^5\text{D}_4 \rightarrow ^5\text{F}_5$ transition, which corresponds to an optical wavelength of 372.099 nm in vacuum [11]. No commercial laser is available at this wavelength with the power needed to focus and collimate the Fe atoms, approximately 500 mW . To meet these specifications, we use a commercially available Ti:S laser, frequency doubled with an LBO crystal placed inside a resonant ring cavity. A schematic of the laser setup is shown in Fig. 3.1.

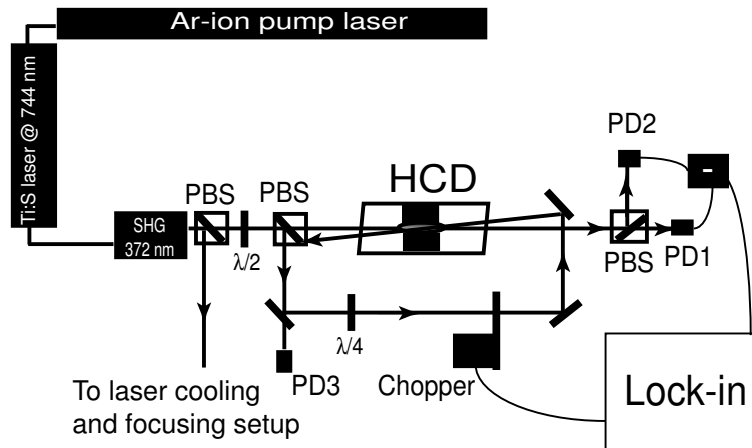


Figure 3.1: Experimental arrangement: An Ar ion laser (Coherent Innova 200) pumped a Ti:S laser (Coherent 899-21), which was frequency doubled with an LBO crystal inside a ring cavity. Part of the doubled beam was used for spectroscopy. Probe and pump beams were split with a polarizing beam splitter (PBS), which in combination with a $\lambda/2$ wave plate also balanced the intensities. The beams were counterpropagating through the hollow cathode discharge. The probe beam was analyzed by 1 or 2 photodiodes (PD1 and PD2) and a Lock-in amplifier referenced to the chopped pump beam. The laser power before absorption was measured by PD3.

In most atom optics experiments, the laser is locked to the atomic transition by using spectroscopy on a vapor cell or an atomic beam. In vapor cells, two Doppler-free spectroscopy schemes are most popular for locking lasers to atomic transitions. One is based on saturated absorption spectroscopy [12], which creates a dispersive locking signal by dithering the laser frequency or the transition frequency. The laser frequency is dithered with an electro-optical (EO) or acousto-optical (AO) modulator in the laser beam, dithering

the transition frequency a modulated magnetic field over the cell. The other Doppler-free locking scheme is based on polarization spectroscopy [12], which creates a dispersive locking signal without use of frequency modulators.

This paper describes the use of polarization spectroscopy on an Fe-Ar hollow cathode discharge cell (sect. 2). The cell and its discharge properties are discussed (sect. 3). Signal-to-background levels of polarization spectroscopy and saturated absorption spectroscopy are investigated, and two different schemes of polarization spectroscopy are used to investigate the effects of velocity changing collisions (VCC) in the polarization spectroscopy signals. The isotope shift for ^{54}Fe and the frequency offset of one of the hyperfine components for ^{57}Fe frequency shift are measured (sect. 4). By integration of the dispersive shaped signal, the laser is locked on the $^5\text{D}_4 \rightarrow ^5\text{F}_5$ transition of ^{56}Fe .

2 Hollow Cathode Discharge Cell

In a regular vapor cell, producing sufficient Fe requires a temperature in the order of 1500 K. As an alternative, we used a hollow cathode discharge cell, in which a high vapor pressure can be reached at lower temperature by sputtering. They are commonly used to perform high-resolution spectroscopy of metal vapors [13–15]. See through hollow cathode discharges are commercially available [16]. However, we followed the design of a Cr hollow cathode discharge of Mlynek’s group at the University of Konstanz [5, 7] (Fig. 3.2).

The cell consisted of a Fe hollow cathode with a length of 20 mm and an inner diameter of 5 mm. Two stainless steel anode rings were mounted at 5 mm from the ends of the hollow cathode to maintain a uniform discharge. The cathode was placed between two pyrex half-tubes, which carried the connectors for the anodes and Ar feed-through. The pyrex tubes were clamped to the cathode block and sealed with o-rings. A continuous flow of Ar was applied to keep the cell clean. The pressure in the cell could be varied from approximately 1 to 2 Torr. The cathode was cooled with water at 17°C .

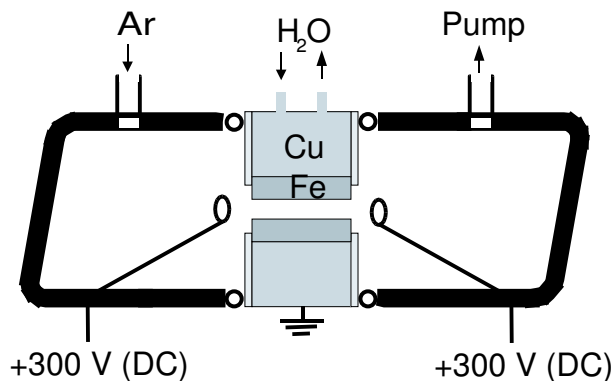


Figure 3.2: Scheme of the hollow cathode discharge cell. The cell consisted of a Fe hollow cathode with a length of 20 mm and an inner diameter of 5 mm. Two stainless steel anode (300 V) rings were mounted, at approximately 5 mm from the ends of the hollow cathode, to maintain a uniform discharge. The cathode was placed between two pyrex half-tubes, which carried the connectors for the anodes and Ar feed-through. The cell was sealed with Viton o-rings. The pressure in the cell could be varied from approximately 1 to 2 Torr. The cathode was grounded and cooled with water at 17°C .

The discharge current was provided by two 300 V-100 mA current stabilized power supplies in parallel. The cathode current was adjusted between 40 mA and 200 mA, for discharge voltages of 260 V to 280 V, at both 1 and 2 Torr Ar pressure.

3 Absorption Spectroscopy

Doppler limited absorption spectroscopy was used to determine the temperature and density of the Fe atoms in the discharge.

At thermal equilibrium, the atoms in the gas cell should follow a Maxwellian velocity distribution. At a temperature T the corresponding Doppler line shape function is given by [17]

$$S(\nu) = \frac{c}{\nu_0} \left(\frac{m}{2\pi kT} \right)^{1/2} \exp\left(\frac{-mc^2(\nu - \nu_0)^2}{2kT\nu_0^2} \right), \quad (3.1)$$

with m the mass of the atoms and ν the frequency of the light, ν_0 the resonance frequency, k the Boltzmann constant and c the speed of light. The absorption of light by the atoms in the cell can be described by the Beer-Lambert relation:

$$I/I_0 = \exp(-aL), \quad (3.2)$$

with I_0 and I the intensity of the incident and transmitted light. The parameter a is the absorption coefficient and L is the interaction length. On resonance the absorption coefficient is

$$a(\nu_0) = n\sigma(\nu_0), \quad (3.3)$$

with $\sigma(\nu_0)$ the absorption cross section on resonance and n the density of the ground state Fe atoms. The semi-classical expression for the absorption cross section on resonance is

$$\sigma = \frac{3}{4} \lambda^2 C_A^2 \Gamma S(\nu_0), \quad (3.4)$$

with λ the wavelength of the atomic transition, $C_A^2 = 0.407$ the weighted average over the relevant Clebsch-Gordan coefficients and Γ the natural line width 2.58 MHz [11] of the ${}^5D_4 \rightarrow {}^5F_5$ transition of Fe. The ground state density can therefore be determined from the intensity ratio of the laser before and after the gas cell and the Doppler line profile on resonance.

To measure the absorption by the Fe atoms the Ti:S laser was scanned over a 4 GHz range, which corresponds to 8 GHz in the UV. Frequency calibration was performed using a Fabry-Perot etalon (FSR=150,0 \pm 0.5 MHz at 744 nm). The intensity of the laser beam was approximately 0.25 times the saturation intensity of 62 $\mu\text{W}/\text{mm}^2$. The laser beam diameter was approximately 1 mm. The laser intensity before and after the gas cell was measured by PD3 and PD1, respectively (Fig. 3.1).

Density and temperature of ground state Fe atoms were measured at three different radial positions and at 1 and 2 Torr Ar pressure. The position range was limited by the size of the laser beam and the hollow cathode inner diameter. The pressure range was limited by the design of the gas inlet system and the discharge current.

The data in Fig. 3.3 show the temperature of the Fe ground state atoms as a function of the discharge current at three radial positions for 1 and 2 Torr Ar pressure. The statistical

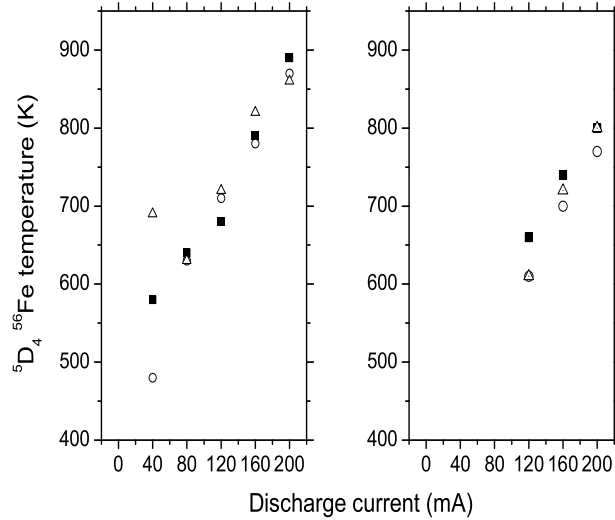


Figure 3.3: Temperature of ground state Fe atoms as function of cathode current for 1 Torr (left) and 2 Torr (right) Ar pressure at three different radial positions: center of cathode (closed boxes), 0.75 mm from center (open circles), and 1.5 mm from center (open triangles).

uncertainty in the temperature is ± 30 K. No significant difference is observed between the temperatures at different radial positions. The large fluctuations at 40 mA were due to instabilities in the discharge. At 2 Torr Ar pressure, the Fe discharge was not stable below 120 mA. Note that the lower temperatures at 2 Torr were due to the larger heat conductivity by the Ar atoms.

Figure 3.4 shows the column density (integrated density times length) as a function of radial position. The statistical uncertainty in the data points is 10^{15} m^{-2} , determined from repeated measurements. Assuming for the sake of simplicity a uniform density along the discharge and an effective length equal to the hollow cathode length ($L=20$ mm), densities were in the order of 10^{18} m^{-3} (10^{-4} Torr) and temperatures around 650 K. An equivalent thermal vapor cell would require a temperature of 1500 K to achieve a similar density. The effect of saturation by the laser light has not been taken into account in the density measurements. A saturation parameter of 0.25 implies approximately 5 percent less total absorption compared to zero incident laser power. The measured density is thus 5 percent lower than the actual density in the cell, which is within the statistical uncertainty.

It is expected that at higher Ar pressures, the Fe density in the middle of the hollow cathode will decrease due to better charge transfer between Fe atoms and Ar ions [18]. Comparing the corresponding 1 Torr and 2 Torr data of Fig. 3.4, the density was significantly lower in the center of the hollow cathode at 2 Torr Ar pressure. No clear systematic deviations from a homogeneous density were observed at 1 Torr.

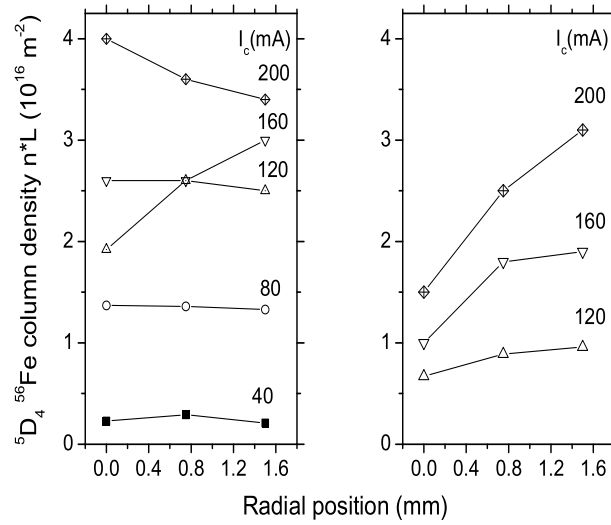


Figure 3.4: Column density as a function of radial position for 1 torr (left) and 2 torr (right) Ar pressure at different cathode currents I_c .

4 Laser locking by polarization spectroscopy

The basic theory of polarization spectroscopy (PS) can be found in [12]. Two laser beams, a linearly polarized probe beam and a circularly polarized pump beam are counter-propagating inside the gas cell. The polarization of the probe beam becomes slightly elliptical with the main axis of the ellipse slightly rotated with respect to the initial polarization direction because of the nonuniform distribution of magnetic sublevels of the Fe atoms in the discharge due to the circularly polarized pump beam. The probe beam is analyzed by a polarizing beamsplitter cube (PBS), of which the principal axis is at 45 or 90 degrees with respect to the polarization of the probe beam. If the cube is at 90 degrees with the probe beam polarization, a non-dispersive signal is observed which is a measure for the change in polarization. With the PBS principal axis at 45 degrees, a dispersive signal can be extracted by subtracting the signals of the light reflected and transmitted by the PBS.

In contrast with saturated absorption spectroscopy, polarization spectroscopy can thus provide a dispersive locking signal without the use of frequency modulation and phase sensitive detection. However, the measured signals are small and detection noise becomes important. To separate the pure polarization spectroscopy signal from the Doppler broadened background, the pump beam was chopped at 2 kHz and a lock-in amplifier was used (Fig. 3.1).

Another advantage of polarization spectroscopy over saturated absorption spectroscopy should be the improved signal-to-background ratio, as the background signal is largely reduced by the use of the PBS and only the change in polarization is observed.

To compare the signal-to-background level of both techniques, we measured both the saturated absorption signal, using a linear polarized probe and a linear polarized chopped

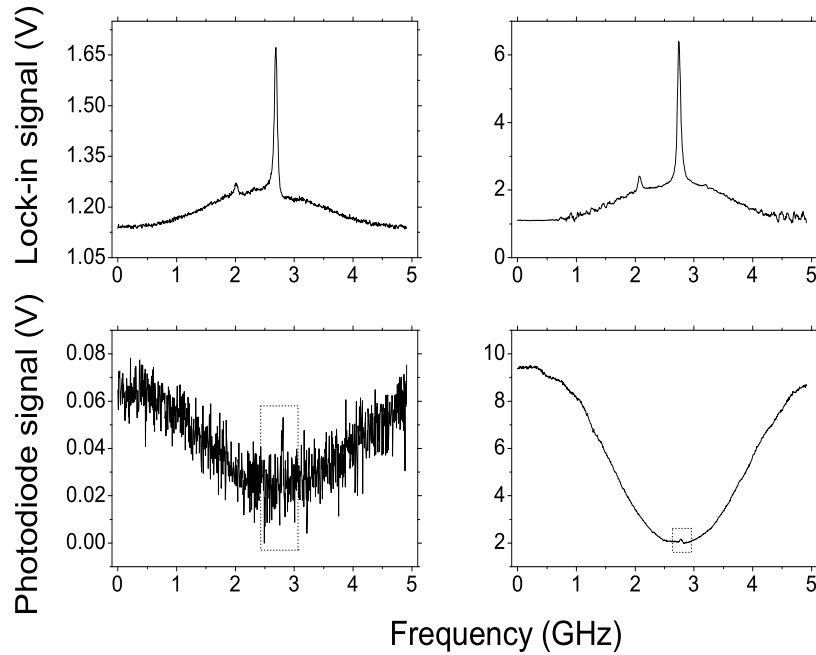


Figure 3.5: Comparison between polarization spectroscopy (left) and saturation spectroscopy (right), measured with (top) and without (bottom) lock-in amplifier. The boxes indicate the Doppler-free polarization and saturated absorption signals. The signal-to-background level for polarization spectroscopy is large compared to saturated absorption spectroscopy. However, the polarization spectroscopy signal is so small that the signal-to-noise level for both techniques are comparable.

pump beam, and the polarization spectroscopy signal with the same set of detectors. Figure 3.5 shows the polarization spectroscopy and saturated absorption spectroscopy signals, with and without the use of lock-in amplifier. The sensitivity of polarization spectroscopy is mainly limited by the detection noise. The ratio between signal and off-resonance background is much larger for polarization spectroscopy than for saturated absorption spectroscopy. However, because of the small absolute value of the polarization spectroscopy signal, detection noise becomes significant. The lock-in signals of both spectroscopic techniques therefore display a comparable signal-to-noise level. Polarization spectroscopy without lock-in amplifier would only be advisable when low-noise detectors are used. Both the polarization and saturated absorption signals suffer from a Doppler pedestal, which is due to velocity changing collisions (VCC). During interaction with the two laser beams, the velocity of the atoms is redistributed by collisions such that the interaction of light with those atoms contributed to the signal at other frequencies.

To overcome the problem of VCC, another polarization spectroscopy scheme was used [19], which is known to be pedestal-free. In this scheme, the probe beam is circularly polarized and the pump beam linearly by placing a $\lambda/4$ wave plate in the probe beam. With the PBS at 90 degrees the non-dispersive laser induced dichroism signal was measured (Fig. 3.6, left). Because of the circular probe, the signals of the transmitted and reflected light from the PBS had to be subtracted. Rotating the PBS to 45 degrees gave the dispersive

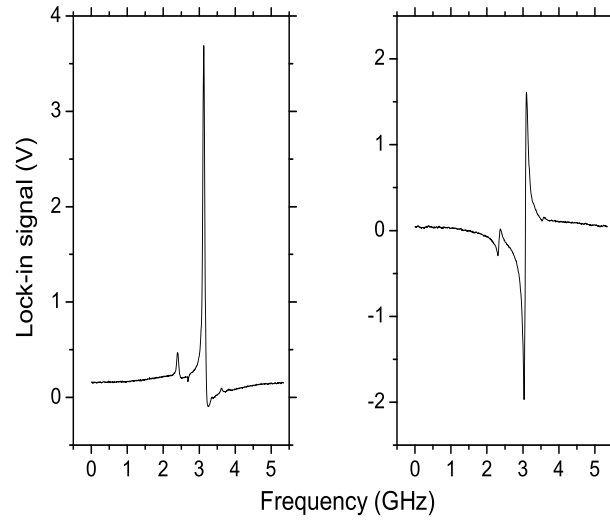


Figure 3.6: Laser induced dichroism (left) and laser induced birefringence (right) signals. The slight dispersive shape of the dichroism signal is due to a small misalignment of the PBS.

laser induced birefringence signal (Fig. 3.6, right).

The birefringence signals from both schemes are shown in Fig. 3.7. The appearance of a Doppler pedestal when velocity changing collisions are present indicates that the anisotropy in magnetic sublevels induced by the pump beam can survive collisions. With a circularly polarized pump beam, the atoms are pumped to the extreme magnetic sublevels ($M=-J$ or $M=J$). Assuming that a collision with an Ar-atom can not induce a large change in orientation of the Fe atom, the Fe atoms will remain partly polarized and the medium will remain anisotropic. In contrast, with a linear pump beam an incomplete transfer to the low- M sublevels will be accomplished. It appears that this anisotropy is less robust against collisions with Ar-atoms.

The minimal measured width of the Doppler-free signals was 33 ± 3 MHz. Attempts were made to reduce this width. Using a beam splitter to reflect the pump beam into the discharge cell, the offset angle between pump and probe beam was nominally reduced to zero. However, the width was not significantly reduced. No significant broadening of the signals could be measured between 1 and 2 Torr Ar pressure, so pressure broadening cannot explain the width of the signals. Another broadening effect in hollow cathode discharges is Stark-broadening, due to transient electric field variations in the discharge. Also the presence of non-uniform magnetic fields in our ferromagnetic hollow cathode discharge could broaden the signals significantly. Power broadening, wavefront imperfections in the beams and very small angle elastic collisions are small effects, which would broaden the signals in the order of 5 MHz.

In the signals of Fig. 3.6 or 3.7, the contributions of other isotopes of Fe are visible. The element Fe has 4 stable isotopes, with natural abundances of: 5.8 percent ^{54}Fe , 91.8 percent ^{56}Fe , 2.1 percent ^{57}Fe , and 0.3 percent ^{58}Fe . The smaller signal below resonance was, considering the natural abundances, the contribution of ^{54}Fe . The corresponding

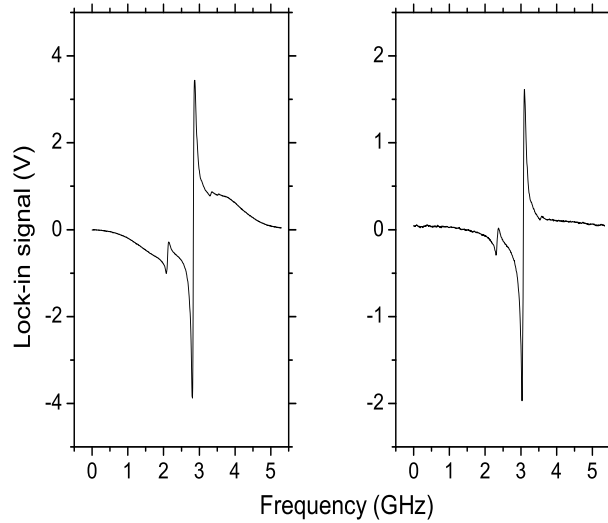


Figure 3.7: Left: Birefringence signal from the polarization spectroscopy scheme with circular pump. Right: Birefringence signal of polarization spectroscopy scheme with circular probe.

measured isotope shift is -725 ± 10 MHz with respect to the ^{56}Fe transition. The tiny signal above resonance is a contribution from ^{57}Fe , with a corresponding measured shift of 495 ± 10 MHz with respect to the ^{56}Fe transition. Isotope ^{57}Fe has nuclear spin of $I=\frac{1}{2}$ thus, this isotope is a fermion with the hyperfine structure of ground and excited levels ($F=\frac{7}{2}, \frac{9}{2}$) and ($F=\frac{9}{2}, \frac{11}{2}$), respectively. Five contributions of ^{57}Fe should be present in the signal, including two cross-over resonances. Only one component was observed: The other contributions were either too small or they overlapped with the other dispersive signals. To measure the isotope shift of ^{57}Fe the shifts of all components should be measured. The contribution from ^{58}Fe was too small to measure.

The laser was locked on the zero-crossing of the dispersive signal by integration-only feedback to the laser external frequency control input. In both polarization spectroscopy schemes the frequency of the laser can be tuned by optical or electronic means. By changing the polarization of the probe beam an imbalance in the two polarization components of the probe beam can be induced, which shifts the dispersive signal up or down and thus shifts the zero-crossing point. Electronically, the frequency can be detuned by applying an offset on the integrator. We have used the latter technique. The laser stability was determined by measuring the amplitude of the dispersive error signal, which was related to the frequency deviation with a previous calibration frequency scan. We measured the amplitude of the dispersive error signal obtained with a circularly polarized pump beam to be larger than with a linearly polarized pump beam, which is favorable for locking. Figure 3.8 shows the effect of locking on the laser frequency by measuring the amplitude of the dispersive signal as a function of time. Typically, the laser lock was stable within 0.2 MHz for hours.

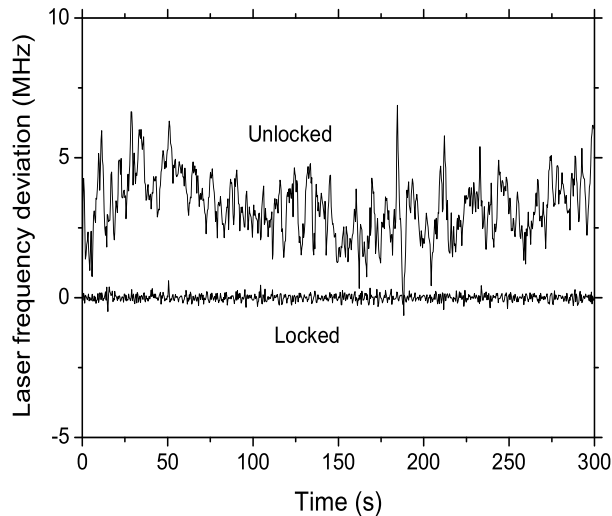


Figure 3.8: The effect of the locking circuit on the long-term stability of the laser frequency. The lock point was chosen on the zero-crossing of the dispersive signal.

5 Conclusions

We have built an Fe-Ar hollow cathode discharge cell to lock a frequency doubled Ti:S laser to the 372 nm $^5D_4 \rightarrow ^5F_5$ transition of ^{56}Fe by means of polarization spectroscopy. Ground state densities in the order of 10^{18} m^{-3} were reached with temperatures of 600 to 700 K. In a standard oven, 1500 K would be necessary to reach a comparable density. Both polarization and saturated absorption spectroscopy showed comparable signal-to-noise levels. The signal-to-noise level of polarization spectroscopy is limited by detection noise. In the polarization spectroscopy scheme with circular pump and linear probe a Doppler pedestal induced by velocity changing collisions remained present. To overcome this problem, we used a scheme with a circular probe and linear pump beam. The minimal measured Doppler-free width was 33 ± 3 MHz. Two signals from other Fe isotopes were measured. The signal corresponding to the ^{54}Fe isotope was shifted by -725 ± 10 MHz with respect to the ^{56}Fe transition frequency. The contribution of one of the hyperfine transitions of ^{57}Fe was shifted by 495 ± 10 MHz with respect to the ^{56}Fe transition frequency. The laser was locked by integrating the dispersive signal. The laser remained locked well within 0.2 MHz for hours.

Acknowledgement

This work is financially supported by the Dutch Foundation for Fundamental Research on Matter (FOM).

References

- [1] E. te Sligte, R.C.M. Bosch, B. Smeets, P. van der Straten, H.C.W. Beijerinck, and K.A.H. van Leeuwen, *Proc. Nat. Acad. Sci.* **99**, 6509 (2002).
- [2] V. Natarajan, R.E. Behringer, and G. Timp, *Phys. Rev. A* **53**, 4381 (1996).
- [3] G. Timp, R.E. Behringer, and D.M. Tennant, J.E. Cunningham, *Phys. Rev. Lett.* **69**, 1636 (1992).
- [4] J.J. McClelland, R.E. Scholten, E.C. Palm, and R.J. Celotta, *Science* **262**, 877 (1993).
- [5] U. Drodofsky, J. Stuhler, B. Brezger, Th. Schulze, M. Drewsen, T. Pfau, and J. Mlynek, *Microelectron. Eng.* **35**, 285 (1997).
- [6] R. Gupta, J.J. McClelland, Z.J. Jabbour, and R.J. Celotta, *Appl. Phys. Lett.* **67**, 1378 (1995).
- [7] U. Drodofsky, J. Stuhler, Th. Schulze, M. Drewsen, B. Brezger, T. Pfau, and J. Mlynek, *Appl. Phys. B: Photophys. Laser Chem.* **65**, 755 (1997).
- [8] R.W. McGowan, D.M. Giltner, and S.A. Lee, *Opt. Lett.* **20**, 2535 (1995).
- [9] R.C.M. Bosch, H.C.W. Beijerinck, P. van der Straten, and K.A.H. van Leeuwen, *Eur. Phys. J. Appl. Phys.* **18**, 221 (2002).
- [10] R.E. Scholten, R. Gupta, J.J. McClelland, R. Celotta, M.S. Levenson and M.G. Vangel, *Phys. Rev. A* **55**, 1331 (1997).
- [11] H.M. Crosswhite, *J. Res. NBS (U.S.)* **79a**, 17 (1975).
- [12] W. Demtröder, *Laser Spectroscopy*, Springer-Verlag, 505 (1981).
- [13] Ph. Dabkiewicz, and T.W. Hänsch, *Opt. Comm.* **38**, 351 (1981).
- [14] S. Kroll, and A. Persson, *Opt. Comm.* **54**, 277 (1985).
- [15] L. Gianfrani, O. Monda, A. Sasso, M.I. Schisano, G.M. Tino, and M. Inguscio, *Opt. Comm.* **83**, 300 (1991).
- [16] Cathodeon Ltd.: <http://www.cathodeon.com>, or Hamamatsu: <http://www.hamamatsu.com>.
- [17] P.W. Milonni, and J.H. Eberly, *Lasers*, John Wiley and Sons, Inc., 101-111 (1988).
- [18] B.E. Warner, K.B. Persson, and G.J. Collins, *J. Appl. Phys.* **50**, 5694 (1979).
- [19] C. Delsart, and J.C. Keller, *Doppler-Free Laser Induced Dichroism and Birefringence, Laser Spectroscopy III*, Proceedings of the 3rd intern. Conf., Jackson Lake 1977, Springer Series in Optical Sciences Vol. 7, 154 (1977).

Chapter 4

Laser cooling simulation based on the semiclassical approach

We investigate the region of validity of the semiclassical approach to simulating laser cooling. We conclude that for the commonly used $\pi^x\pi^y$ polarization gradient configuration the semiclassical approach is only valid for transitions with recoil parameters ε_r on the order of 10^{-4} or less. For the standard laser cooling transitions only the transitions in Rb and Cs satisfy this condition. For the Doppler and $\sigma^+\sigma^-$ polarization gradient configuration the semiclassical approach is valid for most of the commonly used transitions; however, the expected gain in execution speed compared to quantum Monte-Carlo calculations has only been realized in part. A drastic reduction in calculation time is to be expected by implementing an analytical approach to the long-term contribution of the diffusion coefficient.

¹To be published: B. Smeets, R.W. Herfst, E. te Sligte, P. van der Straten, H.C.W. Beijerinck, K.A.H. van Leeuwen, J. Opt. Soc. Am. B

1 Introduction

Laser cooling is a widely spread technique in atomic physics. Many new fields of fundamental and applied physics, like BEC, atom interferometry, and nanofabrication by atom lithography, could be explored using laser cooling to manipulate the motion of atoms, slowing and cooling them down to a few μK . In order to investigate atom lithography with Fe [1,2] we want to simulate laser collimation of an Fe atomic beam.

For simulating laser cooling, a variety of approaches can be used. The most rigorous fully quantummechanical approaches take the quantum-mechanical nature of the center of mass motion as well as the random nature of spontaneous emission into account. They are either based on the density matrix or on the Monte-Carlo wavefunction formalism. In general, these approaches result in excellent agreement with experiments; however, they are computationally very intensive.

Simple semiclassical approaches in which the atoms are treated as classical point particles subject to averaged dipole and radiation forces derived from rate equations allow for quick calculations [3]. However, these models lack the ability to calculate more complex laser cooling schemes, depending on coherence between atomic states, like the $\sigma+\sigma-$ polarization gradient configuration.

Nienhuis *et al.* [4] developed a semiclassical model based on an operator description, in which the motion of the atoms is treated classically, but the evolution of the atomic states is governed by the Optical Bloch Equations. In this approach, the motion of the atom is described by a Brownian motion due to force fluctuations resulting from the random nature of the photon recoil. For velocities $v \gg v_{rec}$, with $v_{rec} = \hbar k/m$ the recoil velocity, these jumps can be neglected. The atomic velocity distribution is then governed by the Fokker-Planck equation. On the other hand, for velocities on the order of the recoil velocity, the motion of the atoms is strongly influenced by these velocity jumps. The velocity dependence of the dissipative force scales with the Doppler velocity $v_D = \Gamma/k$, with Γ the natural linewidth and $k = 2\pi/\lambda$ the wavevector of the light. If k and Γ are such that the resulting velocity distribution is on the same order as the recoil velocity $v_{rec} = \hbar k/m$, the semiclassical approach loses its validity. The recoil parameter $\varepsilon_r = v_{rec}/2v_D = \hbar k^2/2m\Gamma$, which includes all the relevant atomic properties, is thus a measure of the validity of the semiclassical approach. In Table I, a list with the commonly used atom species on which laser cooling is applied is shown. Since the recoil parameter is inversely proportional with the mass m , lighter elements can be expected to have a smaller range in which the SC-model is valid. Also, elements with long-lived excited states or more energetic optical transitions are less suitable to simulate with the SC-model.

A simulation was developed by Hoogerland *et al.* [5] where atomic trajectories were calculated and the operator description of Nienhuis *et al.* [4] was used to calculate the force at each point. In this paper we describe a newly developed simulation program based on the semiclassical approach, where the atomic motion is governed by the Fokker-Planck equation, and we investigate the influence of the recoil parameter. An existing quantum Monte-Carlo (QMC) model is used to validate the resulting velocity distributions calculated with the semiclassical (SC) model. In Section 2 the theory of both models is described. Section 3 describes the implementation of the SC-model. Results are given in Section 4, followed by the conclusions in Section 7.

Table I: Recoil parameters of the transitions of some of the commonly used atomic species in experiments with laser cooling techniques.

Atom	transition	I	λ (nm)	Γ (2π)MHz	$\varepsilon_r(10^{-3})$
^1H	$1^2\text{S}_{1/2} - 2^2\text{P}_{3/2}$	1/2	121.57	99.58	134.5
$^4\text{He}^*$	$2^3\text{S}_1 - 2^3\text{P}_2$		1083.33	1.62	26.2
$^4\text{He}^*$	$2^3\text{S}_1 - 3^3\text{P}_2$		388.98	1.49	221
^7Li	$2^2\text{S}_{1/2} - 2^2\text{P}_{3/2}$	3/2	670.96	5.92	10.7
^{23}Na	$3^2\text{S}_{1/2} - 3^2\text{P}_{3/2}$	3/2	589.16	10.01	2.5
^{39}K	$4^2\text{S}_{1/2} - 4^2\text{P}_{3/2}$	3/2	766.70	6.09	1.43
^{52}Cr	$a^7\text{S}_3 - z^7\text{P}_4$		425.55	5.01	4.23
^{56}Fe	$a^5\text{D}_4 - z^5\text{F}_5$		371.99	2.58	9.98
^{85}Rb	$5^2\text{S}_{1/2} - 5^2\text{P}_{3/2}$	5/2	780.24	5.98	0.65
^{133}Cs	$6^2\text{S}_{1/2} - 6^2\text{P}_{3/2}$	7/2	852.35	5.18	0.4

2 Theory

2.1 Semiclassical model

The semiclassical approach is based on the operator description of laser cooling by Nienhuis *et al.* [4]. Interaction of the atoms with the light field is treated quantum mechanically and the motion of the atoms classically. During the cooling process the atoms undergo small velocity jumps $\hbar k/M$, where k is the wave number of the radiation, and M is the atomic mass. When the final velocity distribution is much broader than such a velocity jump, the evolution of the velocity distribution $\mathcal{W}(\mathbf{v})$ is governed by the Fokker-Planck equation:

$$\frac{\partial}{\partial t}\mathcal{W}(\mathbf{v}) = -\frac{1}{M}\frac{\partial}{\partial \mathbf{v}} \cdot \mathbf{F}(\mathbf{v})\mathcal{W}(\mathbf{v}) + \frac{1}{M^2}\frac{\partial^2}{\partial \mathbf{v}\partial \mathbf{v}} : \overleftrightarrow{\mathbf{D}}(\mathbf{v})\mathcal{W}(\mathbf{v}). \quad (4.1)$$

Here

$$\mathbf{F}(\mathbf{v}) = \langle \mathbf{f}(\mathbf{v}) \rangle \quad (4.2)$$

is the velocity-dependent force on the atoms and $\overleftrightarrow{\mathbf{D}}$ is the momentum diffusion tensor, which can be expressed as the integrated autocorrelation function of the force:

$$2\overleftrightarrow{\mathbf{D}}(\mathbf{v}) = \int_0^\infty d\tau [\langle \mathbf{f}(t)\mathbf{f}(t+\tau) \rangle - \langle \mathbf{f}(t) \rangle \langle \mathbf{f}(t+\tau) \rangle + \langle \mathbf{f}(t+\tau)\mathbf{f}(t) \rangle - \langle \mathbf{f}(t+\tau) \rangle \langle \mathbf{f}(t) \rangle]. \quad (4.3)$$

The radiation field is described by the classical electric field

$$\mathbf{E}(\mathbf{r}, t) = \mathbf{E}_+(\mathbf{r}) \exp(-i\omega t) + \mathbf{E}_-(\mathbf{r}) \exp(i\omega t). \quad (4.4)$$

In the rotating-wave approximation the atom-field coupling is governed by the Rabi-operator

$$\mathcal{R} = \mu_{\text{eg}} \cdot \mathbf{E}_+/\hbar, \quad (4.5)$$

which generalizes the Rabi frequency. The internal state of the atom is described by the density matrix $\sigma(t)$ in the rotating frame. The evolution of σ is given by the Optical Bloch Equations (OBE):

$$\begin{aligned}
\frac{d\sigma_{gg}}{dt} &= \Gamma \sum_{\beta} \mathcal{Q}_{\beta}^{\dagger} \sigma_{ee} \mathcal{Q}_{\beta} + i\mathcal{R}^{\dagger} \sigma_{eg} - i\sigma_{ge} \mathcal{R} \\
\frac{d\sigma_{ee}}{dt} &= -\Gamma \sigma_{ee} + i\mathcal{R} \sigma_{ge} - i\sigma_{eg} \mathcal{R}^{\dagger} \\
\frac{d\sigma_{ge}}{dt} &= -\left(\frac{\Gamma}{2} + i\delta\right) \sigma_{ge} + i\mathcal{R}^{\dagger} \sigma_{ee} - i\sigma_{gg} \mathcal{R}^{\dagger} \\
\frac{d\sigma_{eg}}{dt} &= -\left(\frac{\Gamma}{2} - i\delta\right) \sigma_{eg} + i\mathcal{R} \sigma_{gg} - i\sigma_{ee} \mathcal{R},
\end{aligned} \tag{4.6}$$

where Γ is the spontaneous emission rate and $\delta = \omega - \omega_0$ the detuning of the light frequency ω from the atomic resonance frequency ω_0 . The operators \mathcal{Q}_{β} are the dimensionless dipole operators of which the matrix elements are equal to the Clebsch-Gordan coefficients:

$$\langle eJ_e m_{J_e} | \mathcal{Q}_{\beta} | gJ_g m_{J_g} \rangle = C_i. \tag{4.7}$$

The electric field and thus the Rabi-operators \mathcal{R} and \mathcal{R}^{\dagger} are taken at the time dependent position $\mathbf{r}(t) = \mathbf{r}_0 + \mathbf{v}t$. This approach is justified when $|\mathbf{v}|$ is much larger than the recoil velocity $\hbar k/M$.

The velocity dependent diffusion tensor $\overleftrightarrow{\mathbf{D}}$ has two components, one due to fluctuations of the force from the driving field (stimulated term, $\overleftrightarrow{\mathbf{D}}_{st}$) and another due to coupling of the atom to the vacuum field (spontaneous term, $\overleftrightarrow{\mathbf{D}}_{sp}$). The spontaneous term is equal to

$$\overleftrightarrow{\mathbf{D}}_{sp} = \frac{1}{2} \int d\hat{n} g(\hat{\mathbf{n}}) (\hbar \mathbf{k})^2 \hat{\mathbf{n}} \hat{\mathbf{n}}, \tag{4.8}$$

where

$$g(\hat{\mathbf{n}}) = \frac{3\Gamma}{8\pi} \sum_{\hat{\mathbf{u}} \perp \hat{\mathbf{n}}} \text{Tr} \hat{\mathbf{u}}^* \cdot \mathbf{Q}^{\dagger} \bar{\sigma}_{ee} \mathbf{Q} \cdot \hat{\mathbf{u}} \tag{4.9}$$

is the rate of spontaneous emission per unit solid angle in the direction of the unit vector $\hat{\mathbf{n}}$. The summation in Eq. 4.9 runs over two independent polarization directions $\hat{\mathbf{u}}$ orthogonal to the emission direction $\hat{\mathbf{n}}$. The bar above σ_{ee} refers to steady state situation. The vector operator \mathbf{Q} has three components, which in Cartesian coordinates are:

$$\mathcal{Q}_x = \frac{-1}{\sqrt{2}}(\mathcal{Q}_1 - \mathcal{Q}_{-1}), \quad \mathcal{Q}_y = \frac{-1}{i\sqrt{2}}(\mathcal{Q}_1 + \mathcal{Q}_{-1}), \quad \mathcal{Q}_z = \mathcal{Q}_0. \tag{4.10}$$

The force operator resulting from the driving field is given by $\mathbf{f}^{st} = \hbar(\nabla \mathcal{R} + \nabla \mathcal{R}^{\dagger})$. To calculate the stimulated term ($\overleftrightarrow{\mathbf{D}}_{st}$) it is convenient to introduce the evolution operator $U(t + \tau, t)$, which is defined by

$$\sigma(t + \tau) = U(t + \tau, t) \sigma(t). \tag{4.11}$$

This means that at a given time t the operator $U(t+\tau, t)$ takes the argument and uses the OBE to calculate its value of it at $t+\tau$. With this convention the correlation functions are equal to

$$\langle \mathbf{f}^{st}(t)\mathbf{f}^{st}(t+\tau) \rangle = \text{Tr}U(t+\tau)[\bar{\sigma}(t)\mathbf{f}^{st}(t)]\mathbf{f}^{st}(t+\tau), \quad (4.12)$$

$$\langle \mathbf{f}^{st}(t+\tau)\mathbf{f}^{st}(t) \rangle = \text{Tr}\mathbf{f}^{st}(t+\tau)U(t+\tau)[\mathbf{f}^{st}(t)\bar{\sigma}(t)]. \quad (4.13)$$

From Eq. 4.3 the stimulated diffusion can be calculated using these correlation functions.

2.2 Quantum Monte-Carlo model

The Quantum Monte-Carlo (QMC) model is based on Mollow's treatment of resonant light scattering [6]. A detailed description of the model for arbitrary light fields is given by Dum *et al.* [7]. What follows is a summary of the important features. The numerical implementation of the QMC-model is described by Hoogerland *et al.* [5]. In contrast with the SC-model the kinetic energy is included in the Hamiltonian, which implies that the wave function describes not only the internal states of the atom but also its center-of-mass motion. For an atom in a light field, the total Hamiltonian \hat{H} is given by:

$$\hat{H} = \frac{\hat{p}^2}{2M} + \hat{H}_{0A} + \hat{H}_{0F} + \hat{H}_I(t), \quad (4.14)$$

with \hat{p} the momentum of the atom and M the mass. The operator $\hat{H}_{0A} = \hbar\omega_{eg}\hat{a}^\dagger\hat{a}$ is the Hamiltonian of the free atom, where $\hat{a} = |g\rangle\langle e|$ and $\hat{a}^\dagger = |e\rangle\langle g|$ are the atomic lowering and raising operators, respectively. The kets $|g\rangle$ and $|e\rangle$ are the time-independent ground and excited states, respectively. The operator \hat{H}_{0F} represents the Hamiltonian of the radiation field. In the dipole approximation the interaction Hamiltonian \hat{H}_I is given by:

$$\hat{H}_I(t) = -\mu_{eg}^* \cdot \hat{\mathbf{E}}^\dagger \hat{a} + H.C. \quad (4.15)$$

with μ_{eg} the atomic dipole matrix and $\hat{\mathbf{E}}$ the electric field operator. The laser light field can be represented by a complex vector $\varepsilon_c(\mathbf{r}, t)$, which is for a plane wave in the z -direction $\varepsilon_c(z, t) = \varepsilon_0 \exp[i(kz - \omega t)]$. At the start ($t=0$) we assume all modes of the light field are empty, except the laser mode. We expand the full wave function of atoms and light field $\Psi(\mathbf{r}, t)$ in partial wave functions $\Psi^n(\mathbf{r}, t)$ each with n spontaneously emitted photons:

$$\Psi(\mathbf{r}, t) = \Psi^0(\mathbf{r}, t) + \sum_{n=1}^{\infty} \Psi^n(\mathbf{r}, t). \quad (4.16)$$

For the partial wave function $\Psi^0(\mathbf{r}, t) = C_g^0(\mathbf{r}, t)|g, \{0\}\rangle + C_e^0(\mathbf{r}, t)|e, \{0\}\rangle$ a set of Schrödinger-like equations can be derived. The modulus $|\Psi^0(t)|^2 = |C_g^0(t)|^2 + |C_e^0(t)|^2$ is the probability that no spontaneous emissions has occurred until time t . The loss of probability $1 - |\Psi^0(t)|^2$ is equal to the photon waiting-time distribution $W(t)$, which is given by:

$$1 - |\Psi^0(t)|^2 = \int_0^t W(t')dt' = \Gamma \int_0^t |C_e^0(t')|^2 dt' \quad (4.17)$$

In a Monte-Carlo simulation this photon waiting-time distribution can be used to calculate the time at which a photon is spontaneously emitted by picking a random number $\Upsilon \in [0, 1]$ and solving the equation:

$$1 - |\Psi^0(t)|^2 = \Upsilon \quad (4.18)$$

At this moment the model assumes no further interaction with the spontaneously emitted photon and the atom starts over in the zero-photon ground state with C_g^0 normalized to 1 and all other C 's are zero. In the case of a two-level atom in a travelling wave laser field, the complete time evolution of the coefficients C_g^0 and C_e^0 is given by Mollow [6]; it has been applied to a Monte-Carlo simulation of cooling processes [8, 9] and generalized by Dum *et al.* [7] and Dalibard *et al.* [10] to an arbitrary light field and magnetic atomic substructure.

The momentum in the direction of the laser field is treated quantum mechanically with operator \hat{p} and eigenstates $|p\rangle$. The motion perpendicular to the laser field is treated classically. To include magnetic substructure, the partial wave function Ψ^0 is expanded in time-independent states $|\alpha, m_\alpha\rangle$ and the product wave function is represented by $|\alpha, m_\alpha, p\rangle$, with $\alpha = e, g$. If there is no spontaneous emission, the atomic momentum is quantized as $|p_0 + j\hbar k\rangle$ with $p_0 = \hbar k_0$ the initial momentum and j an integer number with j even or odd for the ground states or excited states respectively. We now have a family F_{p_0} of states that are internally coupled only by stimulated processes. The states of this family are denoted by $|\alpha, m_\alpha, j\rangle$ and have coefficients $C_{\alpha m_\alpha}^j$. Spontaneous emission will transfer an atom to another family $F_{p'_0}$.

The equations of motion for the coefficients $C_{\alpha m_\alpha}^j(t)$ for a family with initial momentum $p_0 = \hbar k_0$ are in a one-dimensional laser configuration in the z direction given by

$$i\hbar \frac{d}{dt} C_{gm_g}^j(t) = \left[\frac{\hbar^2}{2M} (jk + k_0)^2 \right] C_{gm_g}^j(t) + \sum_{q=\pm 1} \frac{\hbar \Omega_{eg}^*}{2} \langle j_g m_g 1q | j_e (m_g - q) \rangle [\epsilon_q^{+*} C_{e(m_g - q)}^{j+1}(t) + \epsilon_q^{-*} C_{e(m_g - q)}^{j-1}(t)] \quad (4.19)$$

$$i\hbar \frac{d}{dt} C_{em_e}^j(t) = \left[\frac{\hbar^2}{2M} (jk + k_0)^2 - \hbar(\Delta + i\Gamma/2) \right] C_{em_e}^j(t) + \sum_{q=\pm 1} \frac{\hbar \Omega_{eg}}{2} \langle j_g (m_e + q) 1q | j_e (m_e) \rangle [\epsilon_q^+ C_{g(m_e + q)}^{j-1}(t) + \epsilon_q^- C_{g(m_e + q)}^{j+1}(t)] \quad (4.20)$$

The Rabi frequency $\Omega_{eg} = \Gamma_{eg} \sqrt{I/(2I_0)}$ with I_0 the saturation intensity. The relative strengths of the orthogonal circular polarization components $+1$ and -1 of the individual laser beams in the $+$ and $-$ directions are denoted by $\epsilon_{\pm 1}^\pm$.

3 Implementation of the semiclassical model

The velocity dependent force is calculated by first assuming a constant velocity. The density matrix evolves according to Eq. 4.6, until steady state is reached. Then $\text{Tr}(\sigma \mathbf{f})$ is evaluated and averaged while the atom moves over one wavelength. In Fig. 4.1 the calculated force is shown for different J -values in a crossed linear polarization configuration ($\pi^x \pi^y$). The maximum force increases with larger J -values and the slope of the force

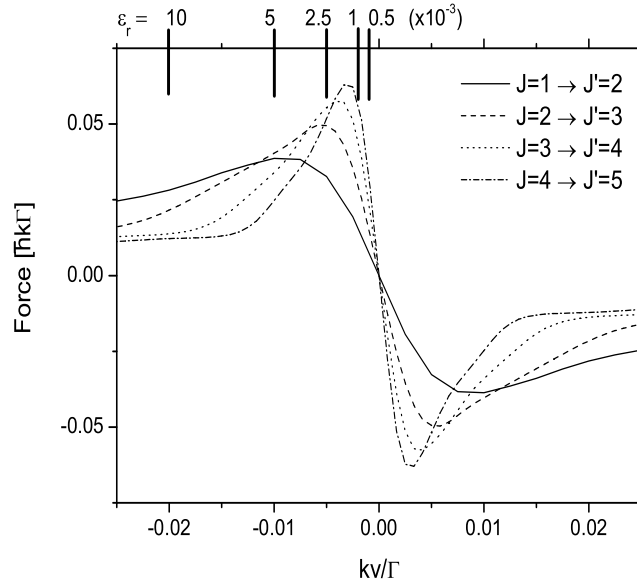


Figure 4.1: Sub-Doppler force for different J -values in the crossed linear polarization configuration, calculated with the SC-method. The saturation parameter $s=2$, and detuning $\delta=-2\Gamma$.

becomes steeper resulting in stronger damping, but it acts on a smaller velocity range compared to smaller J -values.

The diffusion coefficient is calculated by evaluating the integral of Eq. 4.3 for different velocities. The spontaneous and stimulated part are calculated separately. The averaging over a wavelength of the spontaneous part proceeds in the same way as the force. For the stimulated part the integrand is first evaluated with $\langle \mathbf{f}^{st}(t+\tau) \rangle = \text{Tr}U(t+\tau)[\sigma(t)]\mathbf{f}^{st}(t+\tau)$. Since the evolution of the autocorrelation uses the same differential equations as the density matrix [4], the timescale on which the diffusion coefficient converges is the same as the timescale to reach steady state for the density matrix. The integrand of the stimulated part of the diffusion coefficient in a $\pi^x\pi^y$ configuration is shown in Fig. 4.2. The rapidly decaying part on the timescale of Γ^{-1} is a result of the spontaneous decay of the excited state. The slowly decaying part is the contribution from the optical pumping rate i.e., the rate of transfer between the lower-level magnetic substates. This pumping rate decreases with $(J(J+1))^{-1}$ resulting in a proportionally longer calculation time for higher J -values and in decay times longer than the interaction time when simulating laser cooling of atomic beams. After integration the stimulated part of the diffusion coefficient is averaged over a wavelength by choosing several transversal positions within a wavelength for $\bar{\sigma}(t)$. In Fig. 4.3 the stimulated and spontaneous part of the diffusion coefficient are shown for a $\pi^x\pi^y$ polarization configuration and for a $J = 1 \rightarrow J' = 2$ transition. Empirically, we observe that the diffusion coefficient does not deviate more than 0.2% between calculations with different transversal positions when the number of positions over which is averaged is at least 16.

The force and diffusion coefficient scale with $\hbar k\Gamma$ and $(\hbar k)^2\Gamma$, respectively. We can use

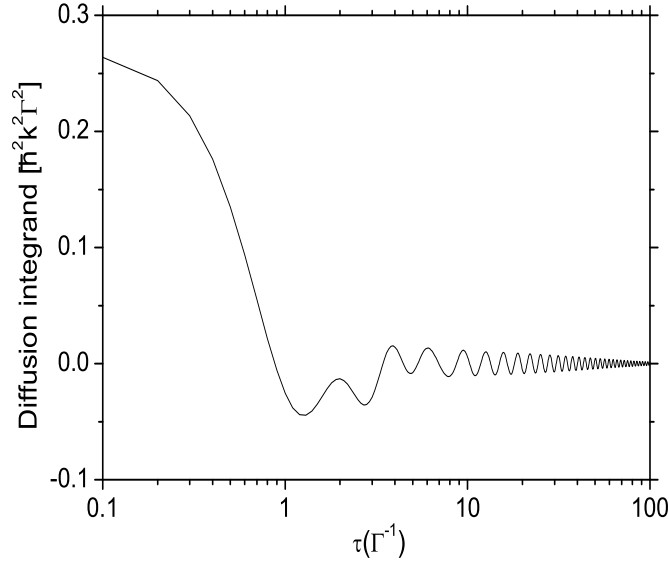


Figure 4.2: Integrand of the stimulated part of the diffusion coefficient for $J = 1 \rightarrow J' = 2$. The part due to spontaneous decay of the excited state decays on a timescale of Γ^{-1} . The part due to pumping over the ground state sublevels decays on a timescale of $100\Gamma^{-1}$. The decay rate of the latter part will decrease with $(J(J+1))^{-1}$. The transverse velocity in this particular case is $v = \Gamma/k$.

the following transformation: $t' = \Gamma t$, $v' = kv_z/\Gamma$, $\mathcal{F} = \vec{F}_z/(\hbar k\Gamma)$ and $\mathcal{D} = \overleftarrow{D}_{zz}/(\hbar^2 k^2 \Gamma)$. The dimensionless Fokker-Planck equation then becomes

$$\frac{\partial}{\partial t'} W(v', t') = -2\varepsilon_r \frac{\partial}{\partial v'} \mathcal{F}(v') W(v', t') + 4\varepsilon_r^2 \frac{\partial^2}{\partial v'^2} \mathcal{D}(v') W(v', t'). \quad (4.21)$$

The FP-equation now scales with ε_r . The larger the recoil parameter, the more dominant the diffusion will be in the cooling process. All the simulations are initialized with a flat velocity distribution.

4 Results

In Fig. 4.1 the recoil velocity is indicated for different recoil parameters ε_r . For most of the $\pi^x \pi^y$ sub-Doppler force profiles the capture velocity is on the same order as the recoil velocity. In that range the validity of the SC-model is questionable. To investigate this effect the velocity distributions obtained with the semiclassical calculations are compared with the distributions resulting from the QMC-model. All distributions are calculated with a $J = 1 \rightarrow J' = 2$ transition to limit the calculation time to approximately 3 hours on a Pentium IV 2 GHz for both models. The distributions are shown in Fig. 4.4. Each of the distributions consists of a broad background, which is the Doppler cooled part and a peak on top which is the sub-Doppler cooled part. With decreasing recoil parameter the distributions of both models show better resemblance. The semiclassical distributions

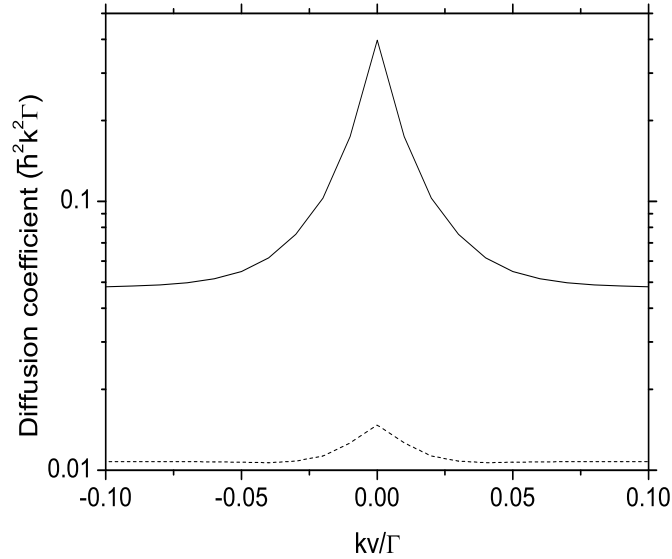


Figure 4.3: Stimulated (full line) and spontaneous (dotted line) part of the diffusion coefficient for crossed linear polarizations for a saturation parameter $s = 2$ and a detuning $\delta = -2\Gamma$.

show a dip in the middle of the distribution, becoming sharper and deeper when the recoil parameter is increased. With larger recoil parameters, the diffusion coefficient becomes dominant in the FP-equation. The sharp peak in the diffusion coefficient near $v = 0$ for a $\pi^x\pi^y$ polarization configuration as shown in Fig. 4.3, results in the dip in the middle of the velocity distribution where the force is smaller. One could think of expanding the FP-equation to higher order terms. At these high recoil parameters, the contribution of a third order term, which scales with ε_r^3 , will not be negligible and will balance the high diffusion near $v = 0$. This would solve the problem of the dip in the velocity distribution. However, at these large recoil parameters, the recoil velocity becomes important resulting in incorrect distributions even with the inclusion of higher order terms, since the velocity range where the sub-Doppler force is active will then be on the order of the recoil velocity. Larger J -values will further decrease the validity range since the force acts on even smaller velocity ranges (Fig. 4.1). A small, very sharp feature is present at recoil parameters $\varepsilon_r = 0.001$ and 0.0005 . This is due to a numerical artefact of the calculation near $v = 0$. At these low velocities the force is very weak, and even small numerical errors in the calculation of the force near $v = 0$ show up in the final distribution.

The Doppler cooled part of both velocity distributions shows striking resemblance. The velocity range on which the Doppler force acts is much larger than the recoil velocity and the corresponding diffusion coefficient is low enough for the FP-equation to be valid for all the recoil parameters in Fig. 4.4.

For the elements in Table I, only Cesium and Rubidium have low enough recoil parameters to simulate a crossed linear polarization configuration without showing a dip in the middle of the resulting velocity distribution. However, for these alkali atoms hyperfine splitting

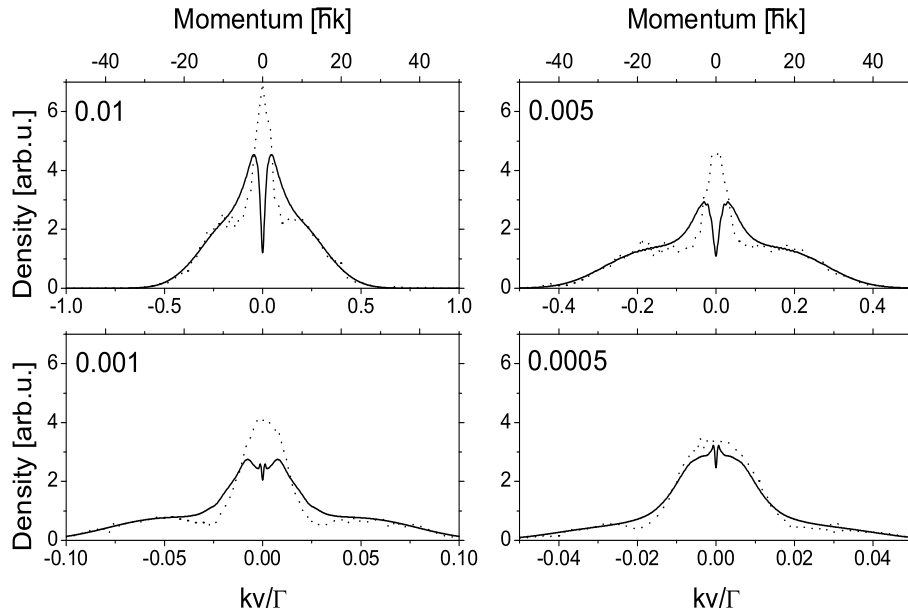


Figure 4.4: Velocity distributions for different recoil parameters $\varepsilon_r = \hbar k^2/2m\Gamma=0.01$ down to 0.0005 as indicated in the figure, with saturation parameter $s=2$, and detuning $\delta = -2\Gamma$ for a $J = 1 \rightarrow J' = 2$ transition. The full lines are the SC-data, the dotted lines are QMC-data.

should be included, which for Cs and Rb implies transitions with F -values larger than 1, reducing the allowed velocity range.

In Fig. 4.5 the velocity distributions for a $\sigma^+\sigma^-$ configuration with $\varepsilon_r = 0.005$ of both models are shown. The match between both models is better than in the equivalent situation in the crossed linear polarization case. The dip in the middle of the SC-distributions due to imbalance between force and diffusion in the FP-equation is absent due to a much lower diffusion as shown in Fig. 4.6. Also, the damping is weaker, and the capture velocity is larger at the same laser settings. The capture velocity of the $\sigma^+\sigma^-$ force is much larger than the recoil velocity. For this situation, the SC-distribution is much smoother than the QMC-distribution for equal computation time. This implies that the QMC-simulation should be executed with more atoms to obtain better statistics, which puts the SC-simulation in an advantage regarding the computation time for the $\sigma^+\sigma^-$ case.

5 Concluding remarks

Laser cooling is simulated by a newly developed simulation based on a semiclassical approach. Intrinsically, this method has the potential of being much faster than an existing QMC-model. At this stage this potential is only realized for the $\sigma^+\sigma^-$ configuration. However, in order to save drastically on calculation time for both $\sigma^+\sigma^-$ and $\pi^x\pi^y$ polarization configurations, the slowly decaying part of the diffusion integrand can be very well

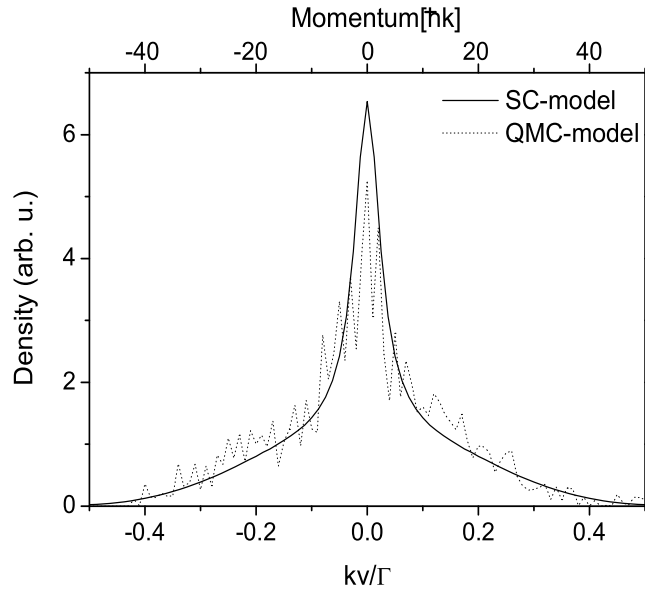


Figure 4.5: Velocity distribution for the $\sigma^+\sigma^-$ configuration. Saturation parameter $s=2$, detuning $\delta = -2\Gamma$, and recoil parameter $\varepsilon = 0.005$.

approximated analytically by a decaying sine of the form $A = \exp(-\gamma t) \sin(\beta t + \phi)$. This can be analytically integrated to $(\beta \cos \phi + \gamma \sin \phi)/(\beta^2 + \gamma^2)$. The analytical approximation could be very useful especially for simulating laser cooling of transitions with large J -values. We estimate a 20-times improvement in calculation time for a $J = 1 \rightarrow J' = 2$ transition and even a 100-times improvement for a $J = 4 \rightarrow J' = 5$ transition when this approximation is used.

For simulations of the $\pi^x\pi^y$ configuration the SC-model gives comparable results with respect to the QMC-model only for low recoil parameters. For high recoil parameters there are two problems: the Fokker-Planck equation should be expanded to higher order terms and the SC-approach, which does not take the recoil velocity into account, is not sufficient, since the velocity range on which the sub-Doppler cooling force acts, becomes on the order of the recoil velocity.

Of the most commonly used atomic species in laser cooling experiments, only Rb and Cs have low enough recoil parameters to be able to simulate a crossed linear polarization configuration ($\pi^x\pi^y$) with the SC-approach.

Due to the much lower diffusion coefficient near $v = 0$ for the $\sigma^+\sigma^-$ polarization configuration compared to the $\pi^x\pi^y$ configuration, the SC-model is valid for much larger recoil parameters. In the $\sigma^+\sigma^-$ configuration the SC-model results in smoother distributions compared to the QMC-model for equal calculation times. For Doppler cooling both models give equal results over a wide recoil parameter range.

In conclusion, the simulation based on the semiclassical approach of Nienhuis *et al.* [4] described in this paper can be used to simulate laser cooling for Doppler cooling and in the $\sigma^+\sigma^-$ configuration over a wide recoil parameter range, with a calculation time advantage

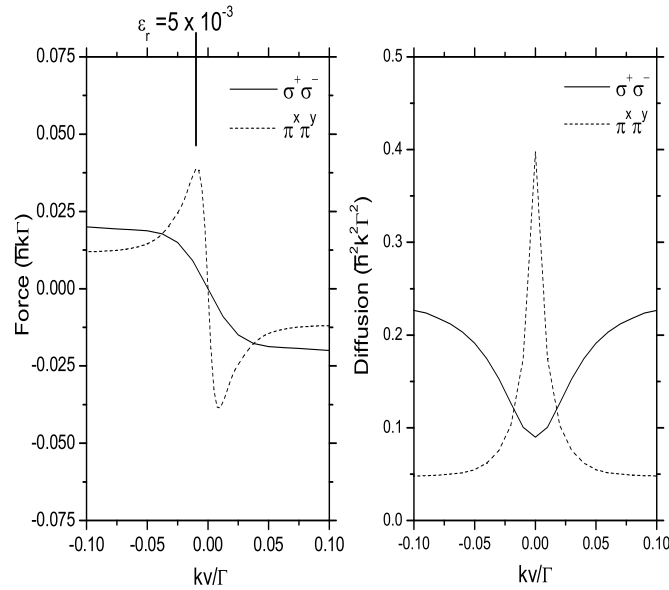


Figure 4.6: Force and diffusion profile for $\pi^x \pi^y$ and $\sigma^+ \sigma^-$ configuration. The recoil velocity for this particular recoil parameter is indicated.

over a full quantum Monte-Carlo model. For the $\pi^x \pi^y$ polarization configuration this simulation gives only comparable results to the quantum Monte-Carlo model when recoil parameters are on the order of 10^{-4} or less.

Acknowledgments

This work is financially supported by the Dutch Foundation for Fundamental Research on Matter (FOM). The authors would like to thank E.D.J. Vredenburg for his work on the QMC-simulation.

References

- [1] E. te Sligte, B. Smeets, K. M. R. van der Stam, R. W. Herfst, P. van der Straten, H. C. W. Beijerinck, and K. A. H. van Leeuwen, *Appl. Phys. Lett.* **85**, 4493 (2004)
- [2] G. Myszkiewicz, J. Hohlfeld, A. J. Toonen, A. F. Van Etteger, O. I. Shklyarevskii, W. L. Meerts, Th. Rasing, and E. Jurdik, *Appl. Phys. Lett.* **85**, 3842 (2004)
- [3] E.J.D. Vredenburg, and K.A.H. van Leeuwen, *Am. J. Phys.* **71**, 760 (2003)
- [4] G. Nienhuis, P. van der Straten, and S-Q. Shang, *Phys. Rev. A* **44**, 462 (1991)
- [5] M.D. Hoogerland, H.F.P. de Bie, H.C.W. Beijerinck, E.J.D. Vredenburg, K.A.H. van Leeuwen, P. van der Straten, and H.J. Metcalf, *Phys. Rev. A* **54**, 3206 (1996)

-
- [6] B.R. Mollow, Phys. Rev. A **12**, 1919 (1975)
- [7] R. Dum, P. Zoller, and H. Ritsch, Phys. Rev. A **45**, 4879 (1992)
- [8] R. Blatt, W. Ertmer, P. Zoller, and J.L. Hall, Phys. Rev. A **34**, 3022 (1986)
- [9] M.D. Hoogerland, M.N.H. Wijnands, H.J. Senhorst, H.C.W. Beijerinck, and K.A.H. van Leeuwen, Phys. Rev. Lett. **65**, 1559 (1990)
- [10] J. Dalibard, Y. Castin, and K. Mølmer, Phys. Rev. Lett. **68**, 580 (1992)

Chapter 5

Laser collimation of an Fe atomic beam on a leaky transition

We report on results of the first laser collimation of a thermal beam of Fe atoms on the leaky ${}^5\text{D}_4 \rightarrow {}^5\text{F}_5$ transition, with both parallel linear $\pi^x\pi^x$ and crossed linear $\pi^x\pi^y$ laser polarization configuration. The measured atomic beam divergence is compared to a rate equation (RE) model and a quantum Monte-Carlo (QMC) model. The experimental values for the divergence are limited by the finite laser linewidth, which is comparable to the natural linewidth of the Fe atom. In general, flux decreases with higher intensities, showing the effect of the leaky transition. At the best beam collimation $\alpha_{RMS} = 0.17$ mrad which is for a detuning of $\delta = -\Gamma$ and a saturation parameter of $s = 6$, the flux decreased to approximately 70%. Highest flux was measured for a detuning of $\delta = -2\Gamma$ and $s = 4$, reaching 135% of the uncooled value. From our measurements we estimate the total leak rate to be $1/(240 \pm 40)$, which is in good agreement with the literature value of $1/244$. The crossed linear polarization configuration is the best choice, with a slightly better collimation but the same atomic beam flux. Plugging of the largest leak would increase the flux to at least 80% of the closed transition value, resulting in better contrast for atom lithography.

¹Published as: B. Smeets, R.W. Herfst, L.P. Maguire, E. te Sligte, P. van der Straten, H.C.W. Beijerinck, K.A.H. van Leeuwen, Appl. Phys. B **80**, 833

1 Introduction

Collimation of atomic beams by laser cooling has become an important technique in the preparation of experiments in various fields of atomic physics. An interesting application is atom lithography. The idea of atom lithography is the focussing of atoms by a standing light wave onto a substrate, which generates nanosized periodic structures with a perfect periodicity. This technique has been applied successfully to sodium [1], chromium [2, 3], aluminum [4], ytterbium [5] beams. Recently also iron nanolines are produced by atom lithography [6, 7], which opens the way to direct deposited ferromagnetic nanostructures. In order to create the narrowest possible structures, the atomic beam should be collimated. Starting from an effusive beam source, collimation can be achieved mechanically by using two apertures. However, this straightforward technique results in a drastic loss of flux. Laser cooling provides a solution: by transverse cooling of the atomic beam, the collimation can be increased without flux loss. The basic idea of laser cooling is that atoms are cooled by the dissipative force, arising from the interaction between atoms and counter-propagating laser beams detuned below resonance. When both beams have identical polarization, the cooling is based on the Doppler effect. Cooling arises from the fact that atoms absorb more photons from the laser beam that propagates in the direction opposite to their own motion. This is often referred to as Doppler cooling. Two counter-propagating laser beams with orthogonal linear polarization give rise to the so-called Sisyphus cooling. This can drastically increase the effectiveness of the cooling, reaching temperatures well below the limit of Doppler cooling. For a review on laser cooling, see Ref. [8].

We present the first laser collimation of an atomic Fe beam for use in atom lithography of ferromagnetic structures. Iron is the most accessible ferromagnetic element for laser-focused deposition. The most practical transition of Fe for laser cooling is the $372.099 \text{ nm } ^5\text{D}_4(3d^6 4s^2) \rightarrow ^5\text{F}_5(3d^6 4s 4p)$ transition, with a lifetime of 61.73 ns ($\Gamma = 2.58(2\pi) \text{ MHz}$), since it can be accessed by a frequency doubled Titanium:Sapphire (Ti:S) laser. The use of this transition exhibits one problem; this transition is not closed. An excited Fe atom can spontaneously decay to three long-lived ($\tau > 1 \text{ s}$) metastable states besides the ground state (Fig. 5.1). The total probability of decay to those states is $1/244$ as given by the NIST manual (Ref. [9]). Thus, on average after 244 spontaneous emissions, the atom will escape from the laser cooling cycle and will no longer interact with the light. A solution for leaky transitions are repumper lasers tuned to the wavelengths with the largest leak rate, which continuously transfer the leaked atoms back to the excited state, and hence back in the cooling cycle. The largest leak in Fe can be closed with light of $\lambda = 501 \text{ nm}$, reducing the leak rate to $1/1400$. At this moment, no compact commercially available laser produces this wavelength. For this purpose, a frequency doubled Ti:S laser or diode laser tuned to 1002 nm can be used. Therefore, we have opted not to use a repumper laser. In this paper, we investigate what can be achieved with laser cooling in the presence of the leaks.

These leaks have two important consequences. First, laser cooling has to be achieved with a restricted number of photons. Therefore, cooling to the equilibrium temperature limit cannot be achieved. Second, a significant fraction of the atomic beam will leave the cooling region in a metastable state. These atoms are not focused by the standing light

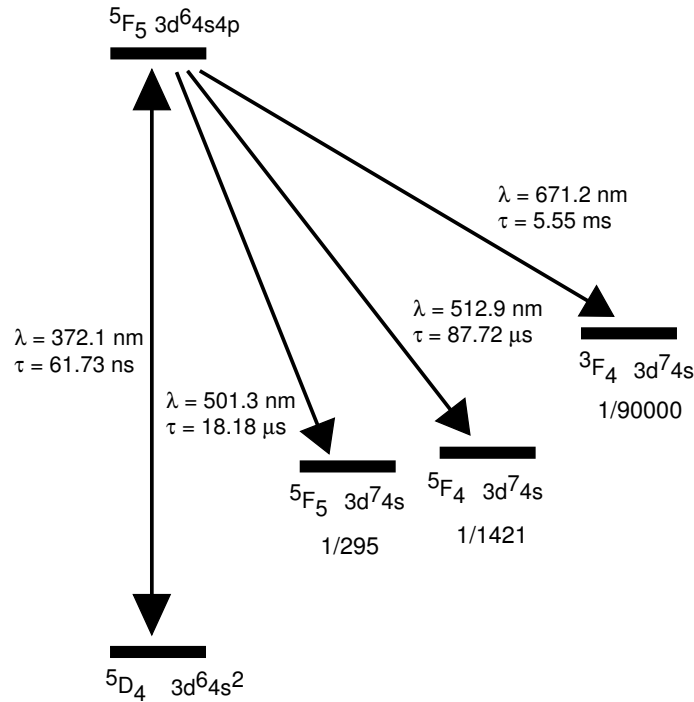


Figure 5.1: Energy level diagram of the ${}^5D_4 \rightarrow {}^5F_5$ transition, including the three leaks to metastable states.

wave and contribute to a background flux that limits the contrast of the atomic beam focusing. In the case of Fe this would lead to a large ferromagnetic background layer, which prohibits the fabrication of separated nanomagnets.

In this paper we explore experimentally and theoretically 1D laser collimation of an Fe atomic beam with both $\pi^x\pi^x$ (parallel linear polarizations) and $\pi^x\pi^y$ (crossed linear polarizations) laser beam configurations. In particular we look at the obtained divergence of the atomic beam, and the effect of the leaky transition on the atomic beam flux for several laser intensities and detunings. Our results show that laser collimation on a leaky transition seriously decreases the useful flux compared to a closed transition collimation. This will eventually lead to a thick uniform layer of Fe atoms on the same order of magnitude as the height of the laser focused structures. A tradeoff between collimation, resulting in narrow structures, and useful flux, implying good structure to background ratio, should be made. In Section 2, the experimental setup is described. The simulation methods are explained in Section 3. Section 4 will deal with the results, followed by the conclusions in Section 5.

2 Experimental setup

In Fig. 5.2 a schematic view of the setup is given. The Fe beam is produced using an Al_2O_3 crucible with an orifice of 1 mm heated by a carbon spiral heater [10]. The operating temperature of the source is typically 2000 K. At that temperature, the Knudsen number is $K_n = 4$, thus a Maxwell-Boltzmann distribution can be assumed. The average longitudinal velocity of the Fe atoms is $(8k_B T/\pi M)^{1/2} = 870$ m/s. The Fe beam intensity

is typically $I_{Fe} = 2.5 \times 10^{16} \text{ s}^{-1}\text{sr}^{-1}$. This value is almost a factor of 10 lower than in the setup used in [7], where the source is operated at 2150 K. However for the present series of measurements the absolute value of the beam intensity is of less importance than for deposition experiments. The atomic beam is further defined by a 0.5 mm diameter skimmer, 150 mm downstream from the nozzle. The isotope ^{56}Fe has a natural abundance of 91.8 %, of which at a temperature of 2000 K, some 50 % is still in the $^5\text{D}_4$ ground state. Hyperfine structure is absent in ^{56}Fe , since the nuclear spin is zero.

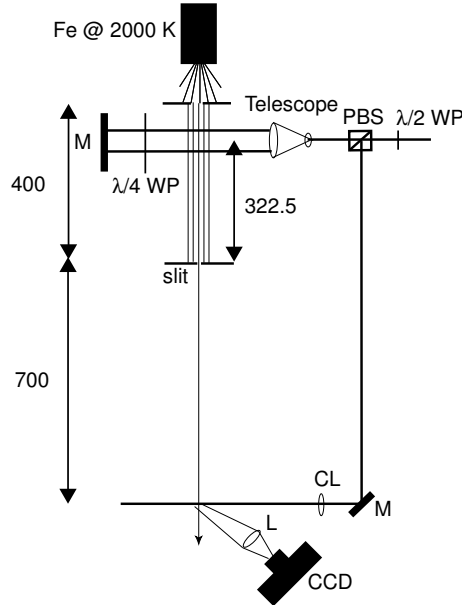


Figure 5.2: Schematic view of the setup. The Fe atoms that emerge from a crucible heated to 2000 K, pass through a skimmer of 0.5 mm diameter and are laser cooled by a telescopically enlarged laser beam with a waist of 60 mm truncated to 45 mm in the longitudinal direction of the atomic beam, 50 mm downstream from the skimmer. A slit of $10 \mu\text{m}$ is placed in the atomic beam 400 mm downstream from the skimmer to measure the divergence of the atomic beam. A highly saturated probe beam excites the Fe atoms 700 mm downstream from the slit. The resulting fluorescence is imaged with a CCD camera, looking from the top in the figure, to obtain a spatial profile of the atomic beam.

The 372 nm light is generated by a frequency doubled Ti:S laser (Coherent 899-21), pumped by an Ar-ion laser (Coherent Innova 200). This laser is locked to the $^5\text{D}_4 \rightarrow ^5\text{F}_5$ transition by polarization spectroscopy on an Fe-Ar hollow cathode discharge within 0.2 MHz [11], as determined from the error-signal. However, this signal is filtered by a lock-in amplifier with an output time constant of 100 ms. Therefore all components of the laser FM noise above 1.6 Hz will be not included in this figure and the actual FM noise will be larger than 0.2 MHz. We estimate the laser linewidth of our UV laser to be around 1 MHz RMS, based on the specifications of the Ti:S laser. This is close to half the natural linewidth of the $^5\text{D}_4 \rightarrow ^5\text{F}_5$ transition.

Laser cooling is performed 50 mm downstream from the skimmer. For laser cooling a Gaussian laser beam with a waist ($1/e^2$ radius) of 60 mm is truncated to an interaction region of 45 mm along the atom beam. Therefore, the intensity of the laser beam decreases by 30 % at the edges of the interaction region in the longitudinal direction. Transversely to the atomic beam, the laser beam has a waist of 0.75 mm, creating an interaction region

in which the intensity decreases by 10 % at the edges of the atomic beam. A quarter-wave plate is placed in front of the back-reflecting mirror, in order to create the $\pi^x\pi^y$ polarization configuration.

The atoms are detected 1.1 m downstream from the skimmer by light induced fluorescence. The fluorescence resulting from a highly saturated probe beam is imaged by a CCD (Apogee 47P) camera. In order to reduce the focal depth, the probe beam is focused to a directed light sheet with waists of $50 \mu\text{m}$ and 1 mm perpendicular to and in the axial direction of the atomic beam, respectively. The magnification of our imaging setup is $1/1.45$. The pixel size of our CCD camera is $10 \mu\text{m}$, resulting in an imaging resolution of $7 \mu\text{m}$.

The divergence of the laser cooled atomic beam is measured by means of a $10 \mu\text{m}$ slit placed 400 mm downstream from the skimmer. The fact that the slit is positioned a certain distance from the skimmer imposes an upper limit on the measurable divergence. The maximum divergence that can be measured is calculated from the size of the atomic beam after the laser cooling section, which is approximately equal to the size of the skimmer (0.5 mm), and the distance from the center of the laser cooling section to slit (322.5 mm). This limits the maximum measurable divergence to approximately 0.35 mrad RMS. The angular resolution of our detection system is 0.01 mrad .

In Fig. 5.3 a typical measurement is shown. The image captured with the CCD camera was line-averaged over the size of the probe laser beam in the axial direction of the atomic beam. The uncooled atomic beam is compared with an example of a laser cooled atomic beam, with saturation parameter $s = I/I_0 = 4$, with saturation intensity $I_0 = 62 \mu\text{W}/\text{mm}^2$, and laser detuning $\delta = -\Gamma$ for the $\pi^x\pi^y$ configuration.

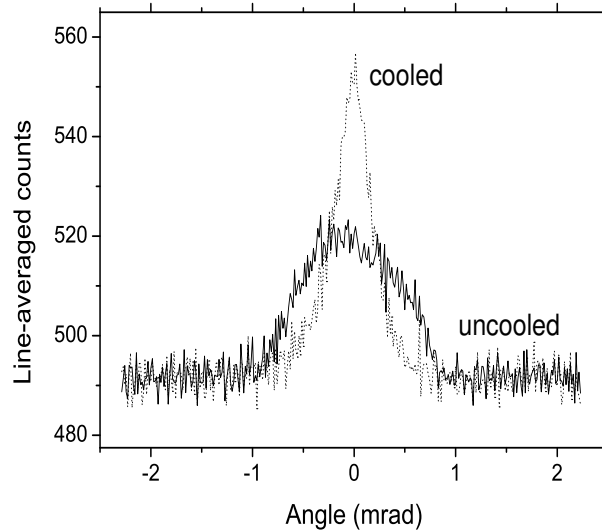


Figure 5.3: Example of an angular distribution image with an exposure time of the CCD camera of 10 s. One image is captured without laser cooling beams (straight line), the other one with laser cooling (dotted line), with a saturation parameter of $s = I/I_0 = 4$ and a detuning $\delta = -\Gamma$ for the $\pi^x\pi^y$ configuration. The width of the uncooled beam is geometrically limited to 0.35 mrad RMS.

3 Simulations

To investigate the role of the leaky transition, we have simulated the collimation experiment using two different models: a rate-equation model (RE) and a quantum monte-carlo model (QMC). Here, we briefly describe these models.

3.1 Rate equation (RE) model

This program keeps track of all the velocity changes due to absorptions and spontaneous emissions of photons. The actual absorption from a particular laser beam is determined by a Monte-Carlo method based on the rate of absorption for each laser beam [12]:

$$R = \frac{s\Gamma}{2(1 + s + (2\delta/\Gamma)^2)}, \quad (5.1)$$

with Γ the natural linewidth of the specific atomic species, s the saturation parameter which is given by the ratio of the laser intensity I to the saturation intensity I_0 of the particular transition, and $\delta = \omega_l - \omega_{eg}$ the detuning from the resonance frequency. Absorption of photons will be in the direction of the laser beam \hat{k} , in contrast spontaneous emission will occur in a random direction according to the dipole radiation distribution. This leads to a net momentum transfer into the direction of the laser beam resulting in a force:

$$\mathbf{F} = R\hbar\mathbf{k}. \quad (5.2)$$

An atom moving with a velocity \mathbf{v} is Doppler shifted with $-\mathbf{k} \cdot \mathbf{v}$, obtaining an effective detuning of $\delta_{eff} = \delta - \mathbf{k} \cdot \mathbf{v}$. Cooling occurs when an atom is irradiated by two identical laser fields with opposite directions $\pm\hat{k}$. The magnitude of the resulting force is then $F = -\beta v_{\perp}$, with β the damping coefficient, and $v_{\perp} = \hat{k} \cdot \mathbf{v}$, the velocity of the atom parallel to the laser beams.

The simulation proceeds as follows: At each point of the trajectory of the atom, the absorption rate from the specific ground state magnetic sublevel of the atom at that point is calculated. Then a small time interval dt is chosen such that the probability of absorbing a photon dP is small. A random pick from a Poisson distribution with average dP decides how many photons are absorbed. Normally this number is zero, but there is a small chance that one photon is absorbed in the time interval dt . The velocity of the atom is changed, accordingly to the recoil momentum of the absorbed photon. The atom is now in the excited state and will spontaneously decay back to the ground state. In which magnetic substate of the ground state the atom ends up depends on the square of the Clebsch-Gordan coefficient for emitting a photon with a particular polarization. A random pick, weighted accordingly, will decide to which sublevel of the ground state the atom will decay. The atom will now move unperturbed during a time interval dt , independent of whether a photon was absorbed or not. At this point, the process starts over again.

The program computes, for each laser intensity and detuning, 5000 atomic trajectories, with a Maxwell-Boltzmann longitudinal velocity distribution, which scales as $v^3 e^{-\frac{mv^2}{2kT}}$ conforming to the temperature of the Fe source. The experimental geometry is taken into

account. The initial transverse velocity for each atom is randomly chosen in a range of -6 m/s to 6 m/s. This range is chosen to be wider than the capture range of the cooling force (as they are the only atoms to be affected) but not so wide as to lead to excessive computation time. For atoms in the excited state, an extra decay channel is introduced with a total probability of $1/244$ representing the leak channel. After decay these atoms do not interact with the light field and follow their path with a constant velocity.

3.2 Quantum Monte-Carlo (QMC) model

The quantum Monte-Carlo (QMC) model is based on Mollow's treatment of resonant light scattering [13]. A detailed description of the model for arbitrary light fields is given by Dum *et al.* [14]. What follows is a summary of the important features. In contrast with the other simulation models the kinetic energy is included in the Hamiltonian, which implies that the wave function describes not only the internal states of the atom but also its center-of-mass motion. For an atom in a light field, the total Hamiltonian \hat{H} is given by:

$$\hat{H} = \frac{\hat{p}^2}{2M} + \hat{H}_{0A} + \hat{H}_{0F} + \hat{H}_I(t), \quad (5.3)$$

with \hat{p} the momentum of the atom and M the mass. The operator $\hat{H}_{0A} = \hbar\omega_{eg}\hat{a}^\dagger\hat{a}$ is the Hamiltonian of the free atom with $\hat{a} = |g\rangle\langle e|$ and $\hat{a}^\dagger = |e\rangle\langle g|$ the atomic lowering and raising operators, respectively. The kets $|g\rangle$ and $|e\rangle$ are the time independent ground and excited state respectively. The operator \hat{H}_{0F} represents the Hamiltonian of the free radiation field. In the dipole approximation the interaction Hamiltonian \hat{H}_I is given by:

$$\hat{H}_I(t) = -\mu_{eg}^* \cdot \hat{\mathbf{E}}^\dagger \hat{a} + H.C. \quad (5.4)$$

with μ_{eg} the atomic dipole matrix and \hat{E} the electric field operator. Mollow showed that a single mode coherent light field can be treated classically when all the other modes of the light field are empty for $t \rightarrow -\infty$. Therefore, the light field can be represented by a complex vector $\varepsilon_c(\mathbf{r}, t)$, which is for a plane wave in the z -direction $\varepsilon_c(z, t) = \varepsilon_0 e^{i(kz - \omega t)}$. At the start ($t = 0$) we assume all light modes are empty, except the laser mode. We split the wave function $\Psi(\mathbf{r}, t)$ into n partial wave functions $\Psi^n(\mathbf{r}, t)$, each with n spontaneously emitted photons:

$$\Psi(\mathbf{r}, t) = \Psi^0(\mathbf{r}, t) + \sum_{n=1}^{\infty} \Psi^n(\mathbf{r}, t). \quad (5.5)$$

For the partial wave function $\Psi^0(\mathbf{r}, t) = C_g^0(\mathbf{r}, t)|g, \{0\}\rangle + C_e^0(\mathbf{r}, t)|e, \{0\}\rangle$ a set of Schrödinger like equations can be derived. The modulus $|\Psi^0(t)|^2 = |C_g^0(t)|^2 + |C_e^0(t)|^2$ is the probability that no spontaneous emissions has occurred until time t . The loss of probability $1 - |\Psi^0(t)|^2$ is equal to the photon waiting-time distribution $W(t)$, which is given by:

$$1 - |\Psi^0(t)|^2 = \int_0^t W(t') dt' = \Gamma \int_0^t |C_e^0(t')|^2 dt' \quad (5.6)$$

In a Monte-Carlo simulation this photon waiting-time distribution can be used to calculate the time at which a photon is spontaneously emitted by picking a random number $\Upsilon \in$

[0..1] and solving the equation:

$$1 - |\Psi^0(t)|^2 = \Upsilon \quad (5.7)$$

At this moment, we assume no further interaction with the spontaneously emitted photon, and start over in the zero-photon ground state with $C_g^0 = 1$ and all other C 's are zero. In the case of a two-level atom in a travelling wave laser field, the complete time evolution of the coefficients C_g^0 and C_e^0 is given by Mollow [13]; it has been applied to a Monte-Carlo simulation of cooling processes [15–17] and generalized by Dum *et al.* [14] and Dalibard *et al.* [18] to an arbitrary light field and magnetic atomic substructure.

The momentum in the direction of the laser field is treated quantum mechanically with operator \hat{p} and eigenstates $|p\rangle$. The motion perpendicular to the laser fields is treated classically. To include magnetic substructure, the partial wave function Ψ^0 can be expanded in time-independent states $|\alpha, m_\alpha\rangle$ with coefficients $C_{\alpha m_\alpha}$ ($\alpha = e, g$). The product wave function is represented by $|\alpha, m_\alpha, p\rangle$. If there is no spontaneous emission, the atomic momentum is quantized as $|p_0 + j\hbar k\rangle$ with $p_0 = \hbar k_0$ the initial momentum and j an integer number. We now have a family F_{p_0} of states that are internally coupled only by stimulated processes. The states of this family are denoted by $|\alpha, m_\alpha, j\rangle$ and have coefficients $C_{\alpha m_\alpha}^j$. The momentum eigenvalues are $p_0 + j\hbar k$ with j even or odd for the ground states or excited states respectively. Spontaneous emission will transfer an atom to another family $F_{p'_0}$.

The equations of motion for the coefficients $C_{\alpha m_\alpha}^j(t)$ for a family with initial momentum $p_0 = \hbar k_0$ are in a one-dimensional laser configuration in the z direction given by

$$i\hbar \frac{d}{dt} C_{gm_g}^j(t) = \left[\frac{\hbar^2}{2M} (jk + k_0)^2 \right] C_{gm_g}^j(t) \quad (5.8)$$

$$+ \frac{\hbar\Omega_{eg}^*}{2} \langle j_g m_g 1 1 | j_e(m_g - 1) \rangle [\epsilon_1^{+*} C_{e(m_g-1)}^{j+1}(t) + \epsilon_1^{-*} C_{e(m_g-1)}^{j-1}(t)]$$

$$+ \frac{\hbar\Omega_{eg}^*}{2} \langle j_g m_g 1 - 1 | j_e(m_g + 1) \rangle [\epsilon_{-1}^{+*} C_{e(m_g+1)}^{j+1}(t) + \epsilon_{-1}^{-*} C_{e(m_g+1)}^{j-1}(t)]$$

$$i\hbar \frac{d}{dt} C_{em_e}^j(t) = \left[\frac{\hbar^2}{2M} (jk + k_0)^2 - \hbar(\Delta + i\Gamma/2) \right] C_{em_e}^j(t) \quad (5.9)$$

$$+ \frac{\hbar\Omega_{eg}}{2} \langle j_g(m_e + 1) 1 1 | j_e(m_e) \rangle [\epsilon_1^+ C_{g(m_e+1)}^{j-1}(t) + \epsilon_1^- C_{g(m_e+1)}^{j+1}(t)]$$

$$+ \frac{\hbar\Omega_{eg}}{2} \langle j_g(m_e - 1) 1 - 1 | j_e(m_e) \rangle [\epsilon_{-1}^+ C_{g(m_e-1)}^{j-1}(t) + \epsilon_{-1}^- C_{g(m_e-1)}^{j+1}(t)]$$

The Rabi frequency $\Omega_{eg} = \Gamma_{eg} \sqrt{I/(2I_0)}$ with I_0 the saturation intensity. The relative strengths of the orthogonal circular polarization components $+1$ and -1 of the individual laser beams in the $+$ and $-$ directions are denoted by $\epsilon_{\pm 1}^\pm$.

For simulation of the experiment, a transverse momentum range from -80 to $+80 \hbar k$ ($80 \hbar k = 1.5$ m/s) is chosen, limited by the computation time since it goes quadratic in momentum range. For each laser intensity and detuning we simulate 1000 atoms each starting out as a plane atomic wave, thus with a single velocity. The interaction time is divided into small intervals. For simplicity the interaction time is fixed, assuming a single longitudinal velocity equal to the average longitudinal velocity corresponding to the temperature in the Fe source. This assumption does not result in significant

differences compared to the situation of a Maxwell-Boltzmann distribution. This was checked by running the program for different interaction times and averaging the resulting momentum distributions, weighted according to a Maxwell-Boltzmann distribution. Each time a spontaneous emission takes place, the excited atom can decay to a metastable state with a probability of $1/244$. The simulation only follows the atoms in momentum space, neglecting information about experimental geometry.

3.3 Implementation

Both simulations are performed with a monochromatic light field. However, experimentally, the laser linewidth is of the same order as the natural linewidth of Fe. This is included in the simulations by assuming a Gaussian laser linewidth, with an RMS width of $\Gamma/2$. For each laser intensity, the RMS divergence of the atomic beam was quadratically averaged for 5 detunings, each weighted according to the Gaussian linewidth distribution. The calculated RMS atomic beam divergence was masked with a Gaussian transmission function with a RMS divergence of 0.35 mrad, being the geometrical limit of the experimental setup. In Fig. 5.4, the effect of the averaging on the resulting divergence of the atomic beam is visible for an average detuning of $\delta = -\Gamma/2$ as a function of laser intensity. From the large difference in the divergence obtained with the RE model and the QMC model for high intensities, it is clear that the RE model does not include all stimulated diffusion effects of atom-laser interactions. As can be seen from the QMC results, the contribution of the sub-Doppler cooling force is small due to the small capture range of this force in the case of Fe. This is a known effect for atoms with a small natural linewidth in combination with a large recoil velocity [19]. The discrepancy between the averaged and the monochromatic results is largest at low intensities: the atomic beam has a larger divergence for the other laser detunings included in the laser linewidth resulting in a larger average divergence. For high intensities, the difference is smaller, since cooling is efficient over a larger detuning range. The striking difference between the RE model and the QMC model for high intensity in the monochromatic case is almost entirely absent in the averaged results.

4 Results and Discussion

The atomic beam divergence was measured for a $\pi^x\pi^x$ and a $\pi^x\pi^y$ polarization configuration, for saturation parameters ranging from $s = 1/2$ to $s = 6$, and for three detunings: $\delta = -\Gamma/2$, $\delta = -\Gamma$, and $\delta = -2\Gamma$. These measurements are compared to the results from the simulation models.

In Fig. 5.5 the atomic beam divergences obtained from measurements and simulations are shown. The left column are results for the $\pi^x\pi^x$ configuration. The experimental error-bars are on the order of the symbol size. Despite the rather crude implementation of the laser linewidth, the agreement between measurement and simulation is satisfying, implying that the cooling is mainly limited laser to natural linewidth ratio of ≈ 1 . For a detuning of $\delta = -2\Gamma$ the measured atomic beam divergence is consistently lower than the simulated data. This could be attributed to a slight overestimation of the detuning in the

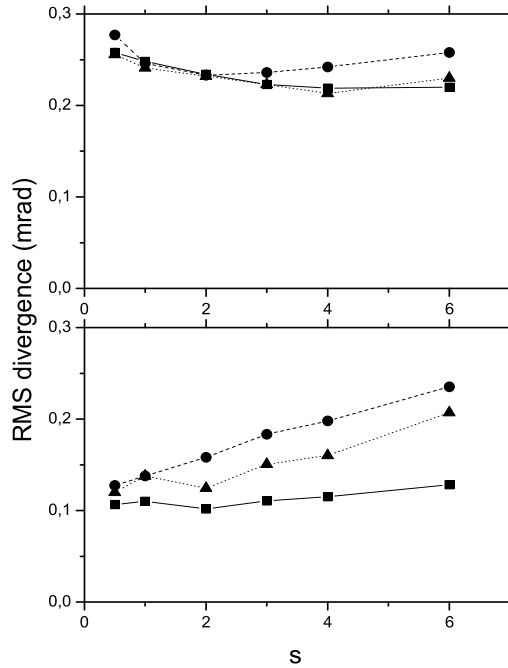


Figure 5.4: The effect of the averaging of five detunings on the simulated divergence of the atomic beam for an average detuning of $\delta = -1/2\Gamma$ as a function of laser intensity. The squares are results obtained with the RE model in the $\pi^x\pi^x$ polarization configuration. The circles and triangles are QMC simulations with a $\pi^x\pi^x$ and a $\pi^x\pi^y$ polarization configuration, respectively. In the upper graph, the atomic beam divergence convoluted with the laser linewidth is shown. In the lower graph, the simulated atomic beam divergence with a monochromatic light field is shown.

experiment. The lower beam divergence simulated with the QMC model compared to the RE model for the $\delta = -2\Gamma$ case is due to the narrow momentum range over which the QMC program simulates, resulting in a smaller momentum range than the cooling force capture range. In the RE simulation atoms are also captured from outside the capture range of the cooling force. These atoms are not as cold, resulting in a larger atomic beam divergence. In the right column, results for the $\pi^x\pi^y$ configuration are shown. This time, only QMC results are included, since the RE model cannot simulate this configuration. We achieved best collimation at an (average) detuning of $\delta = -\Gamma$ in the $\pi^x\pi^y$ configuration: $\alpha_{RMS} = 0.17$ mrad.

In Fig. 5.6 the measured relative fluxes of ground state Fe atoms through the $10 \mu\text{m}$ slit are shown and compared to the RE model. This flux measurement shows the effect of the leaky transition and is useful for optimizing laser parameters, balancing flux and collimation. Since the RE model is the only model that follows the atomic trajectories in momentum space and in real space, the flux was calculated from the RE simulation by placing a virtual slit at the position of the $10 \mu\text{m}$ slit in the real experiment. To obtain acceptable statistics, this virtual slit was $250 \mu\text{m}$ wide in stead of $10 \mu\text{m}$. As the virtual slit is half the source size, this does not affect the relative flux gain. The effect of the laser linewidth was included by averaging the flux obtained from monochromatic simulations

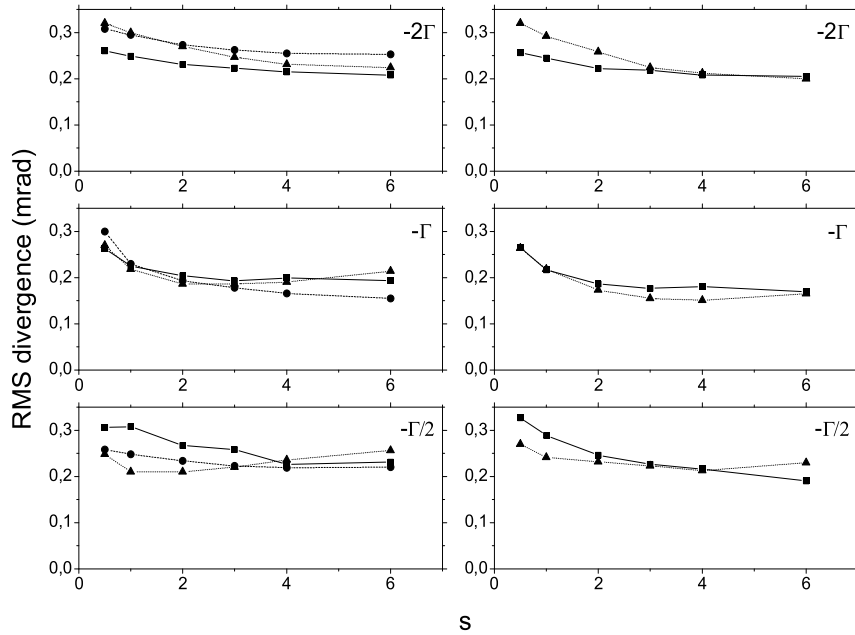


Figure 5.5: The atomic divergence obtained from measurements and simulations. In the left column results for the $\pi^x \pi^x$ configuration are shown. The squares are the measurements, the circles the RE model, and the triangles the QMC model. In the right column, results for the $\pi^x \pi^y$ configuration are shown.

at five different detunings. The measured fluxes are in reasonable agreement with the simulated data. Both in measurements and simulations, the effect of the leak is clearly visible: for a closed transition there is always flux gain for negative detuning. In contrast we lose up to 65% of our flux at high intensity and small detuning.

Comparing the two laser polarization configurations, no significant difference was measured, meaning the excited state fraction during the interaction with the light is comparable in both cases. This puts the $\pi^x \pi^y$ configuration in advantage over the $\pi^x \pi^x$ case, since it collimates the atomic beam slightly better, without extra loss of flux. A large detuning is favorable, since flux gain is largest. In this case atoms are pushed into the relevant window due to the larger capture range of the cooling force, although this also implies a less efficient atomic beam collimation. A small detuning $\delta = -\Gamma/2$, the optimal value for Doppler cooling with monochromatic light and no leak channel, is not an optimal choice; the flux is lowest and collimation of the atomic beam is not optimal. The best beam collimation ($\alpha_{RMS} = 0.17$ mrad) is reached for $\delta = -\Gamma$ and $s = 6$ in the $\pi^x \pi^y$ configuration. At these settings the flux decreases to 70% of the value without laser cooling. Highest flux gain is reached for a detuning of $\delta = -2\Gamma$: up to 135% of the non-cooled value.

To estimate the measured leak rate, we performed simulations at different leak rates. We compared these results with the measured fluxes for $s = 6$, since for high intensity the flux is less dependent on experimental parameters. This resulted in a leak rate of $1/(240 \pm 40)$, which is in agreement with the leak rate of $1/244$, given in Ref. [9].

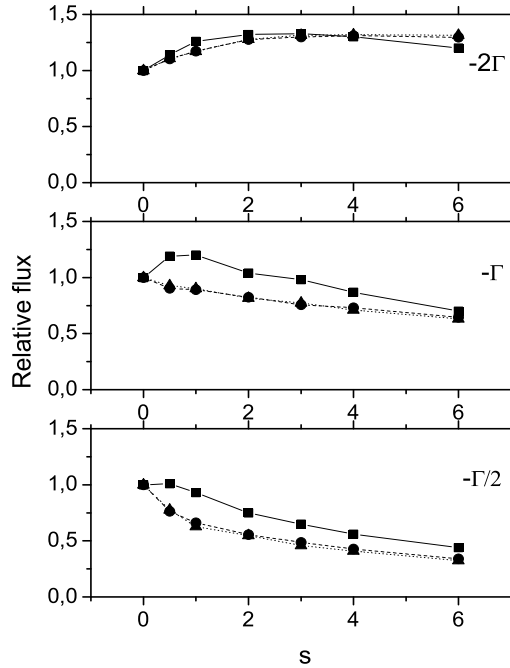


Figure 5.6: The measured relative fluxes through the $10 \mu\text{m}$ slit, compared to the rate equation model. The squares are the RE simulations, the circles the measurements with the $\pi^x\pi^x$ polarization configuration, and the triangles the measurements with the $\pi^x\pi^y$ configuration. This flux measurement shows the effect of the leaky transition and is useful for optimizing laser parameters, balancing flux and collimation.

In Fig. 5.7 the relative flux obtained with the RE model for a monochromatic light field with and without leak channel are compared, for a detuning of $\delta = -\Gamma$. With increasing saturation parameter, the loss of flux due to the leak becomes even more pronounced, resulting in a loss of a factor 3 at $s = 6$. The plugging of the largest leak with a 501 nm repumper results in a gain in flux up to a factor of approximately 2.5 at $s = 6$. The remaining flux loss is mainly due to decay to the ${}^5\text{F}_4$ with a leak rate of $1/1420$. Decay to the ${}^3\text{F}_4$ state is too slow to have any significant effect on the flux. Assuming a excited state fraction of 50% for high saturation parameters, a simple model $e^{-\frac{t_{int}}{244\tau_{eff}}} = 0.18$, with $t_{int} = \frac{870}{0.045}$ s the atom-light interaction time and $\tau_{eff} = 2/\Gamma$ the effective absorption rate for high s , gives a lower limit of the ratio between flux with and without leak. For the data in Fig. 5.7 this ratio is 0.35 for high saturation intensity.

5 Conclusions

In conclusion, we have collimated a thermal beam of Fe atoms by laser cooling on a leaky transition. Both parallel linear ($\pi^x\pi^x$) and crossed linear ($\pi^x\pi^y$) laser polarization configurations are used. The experimental values for the atomic beam divergence are compared to a rate equation and quantum Monte-Carlo model. The collimation was limited by the finite laser linewidth, which was comparable to the natural linewidth of

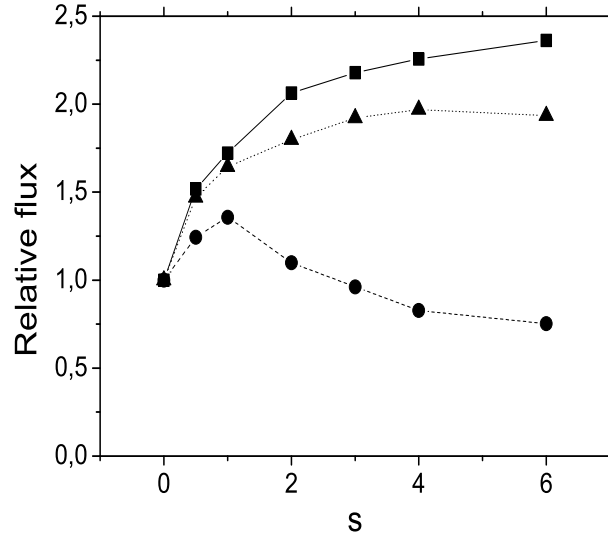


Figure 5.7: The relative flux for a detuning of $\delta = -\Gamma$ obtained with the RE model. The squares are flux values without leak channel. The circles are values with a leak rate of $1/244$. The triangles represent the flux with the largest leak plugged.

the Fe atom. In general, flux decreased with higher intensities, showing the effect of the leaky transition. A collimation of $\alpha_{RMS} = 0.17$ mrad could be achieved, however the flux decreased to approximately 70% of the non-cooled value. Highest flux was measured for a detuning of $\delta = -2\Gamma$, reaching 135% of the non-cooled value. The difference between both polarization configurations is small. The crossed linear polarization configuration gives the same flux, but slightly better collimation. Plugging of the largest leak would increase the flux to 80% of the closed transition value for $s = 6$ or even higher for lower intensities, resulting in better contrast for atom lithography. From our measurements we estimate the leak rate to be $1/(240 \pm 40)$, which is in good agreement with a $1/244$ leak rate found in the literature.

Acknowledgement

This work is financially supported by the Dutch Foundation for Fundamental Research on Matter (FOM). The authors would like to thank E.J.D. Vredenburg for his work on both simulation programs, and R.E. Scholten for lending his CCD camera for all the measurements included in this paper.

References

- [1] G. Timp, R.E. Behringer, and D.M. Tennant, J.E. Cunningham, Phys. Rev. Lett. **69**, 1636 (1992).
- [2] J.J. McClelland, R.E. Scholten, E.C. Palm, and R.J. Celotta, Science **262**, 877 (1993).

-
- [3] U. Drodofsky, J. Stuhler, Th. Schulze, M. Drewsen, B. Brezger, T. Pfau, and J. Mlynek, *Appl. Phys. B: Photophys. Laser Chem.* **65**, 755 (1997).
- [4] R.W. McGowan, D.M. Giltner, and S.A. Lee, *Opt. Lett.* **20**, 2535 (1995).
- [5] R. Ohmukai, S. Urabe, and M. Watanabe, *Appl. Phys. B*, **77**, 415-419 (2003).
- [6] E. te Sligte, B. Smeets, K. M. R. van der Stam, R. W. Herfst, P. van der Straten, H. C. W. Beijerinck, and K. A. H. van Leeuwen, *Appl. Phys. Lett.* **85**, 4493 (2004).
- [7] G. Myszkiewicz, J. Hohlfeld, A. J. Toonen, A. F. Van Etteger, O. I. Shklyarevskii, W. L. Meerts, Th. Rasing, and E. Jurdik, *Appl. Phys. Lett.* **85**, 3842 (2004).
- [8] H. J. Metcalf, and P. van der Straten, *Laser Cooling and Trapping*, Springer-Verlag New York (1999).
- [9] NIST Atomic Spectra Database, http://www.physics.nist.gov/cgi-bin/AtData/main/_asd.
- [10] R.C.M. Bosch, H.C.W. Beijerinck, P. van der Straten, and K.A.H. van Leeuwen, *Eur. Phys. J. Appl. Phys.*, **18**, 221 (2002). The atomic beam source described in this paper is used in thermal mode.
- [11] B. Smeets, R.C.M. Bosch, P. van der Straten, E. te Sligte, R.E. Scholten, H.C.W. Beijerinck, K.A.H. van Leeuwen, *Appl. Phys. B*, **76**, 815 (2003).
- [12] E.J.D. Vredenburg, and K.A.H. van Leeuwen, *Am. J. Phys.* **71**, 760 (2003).
- [13] B.R. Mollow, *Phys. Rev. A*, **12**, 1919 (1975).
- [14] R. Dum, P. Zoller, and H. Ritsch, *Phys. Rev. A* **45**, 4879 (1992).
- [15] R. Blatt, W. Ertmer, P. Zoller, and J.L. Hall, *Phys. Rev. A* **34**, 3022 (1986).
- [16] M.D. Hoogerland, M.N.H. Wijnands, H.J. Senhorst, H.C.W. Beijerinck, and K.A.H. van Leeuwen, *Phys. Rev. Lett.* **65**, 1559 (1990).
- [17] M.D. Hoogerland, H.F.P. de Bie, H.C.W. Beijerinck, E.J.D. Vredenburg, K.A.H. van Leeuwen, P. van der Straten, and H.J. Metcalf, *Phys. Rev. A* **54**, 3206-3218 (1996).
- [18] J. Dalibard, Y. Castin, and K. Mølmer, *Phys. Rev. Lett.* **68**, 580 (1992).
- [19] P.D. Lett, W.D. Phillips, S.L. Rolston, C.E. Tanner, R.N. Watts, and C.I. Westbrook, *J. Opt. Soc. Am. B*, **6**, 2084 (1989).

Chapter 6

Fe nanolines without laser cooling

Using direct-write atom lithography, Fe-nanolines are deposited with a pitch of 186 nm, a FWHM width of 50 nm, and a height of up to 6 nm. These values are achieved by relying on geometrical collimation of the atomic beam, thus without using laser cooling techniques. This opens the way for applying direct-write atom lithography to a wide variety of elements. The experimental nanolines are compared with simulations for two situations: one with the standing light wave passing just above the substrate, and one where the standing light wave is cut in half by the substrate. Discrepancy between measurements and simulations is present for situations where the standing light wave is cut in half by the substrate. We attribute this effect to diffraction of the laser beam. The height of the lines amounts to 50 % of the total deposited layer thickness at the largest laser intensity. In a MOKE (Magneto-Optical Kerr effect)-setup we were able to verify that the deposited Fe-layer is ferromagnetic. Magnetic anisotropy is detected, however, the anisotropy is present over the entire sample, not only where the lines are grown and is thus not an indication of the presence of the modulation. We tried to measure the magnetic anisotropy due to the presence of the nanolines with a MFM (Magnetic Force Microscope), without success. In contrast, the magnetization of background-free nanolines, deposited through a mechanical mask with a pitch of 744 nm and a FWHM of 150 nm, is visualized by MFM. This shows that size and background of the standing wave produced nanolines limits the ability to measure the influence of the nanolines on the magnetization of the Fe-layer.

1 Introduction

In direct-write atom lithography, also known as laser-focused deposition, atoms are focused into a periodic pattern by a standing light wave. This technique has been applied to Na, [1], Cr [2, 3], Al [4], Yb [5], and recently to Fe [6, 7]. Just as for the case of focusing light, a well collimated beam is crucial for atom lithography. An atomic beam arriving at the lens with a local angular spread will result in broadening of the deposited features. To obtain a well collimated atomic beam, laser cooling techniques are generally used. However, effective laser cooling requires a closed transition. For numerous elements a closed transition is not accessible with present lasers, or hyperfine splitting is present, and the use of several repumping lasers becomes a necessity. For Fe, an accessible closed transition from the ground state does not exist, resulting in the loss of focusable atoms when applying laser cooling [8].

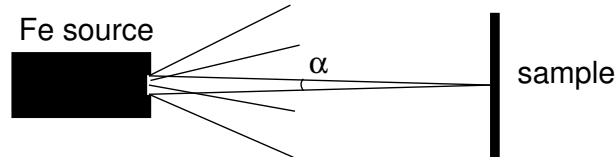


Figure 6.1: Geometrical collimation. Only atoms within the angle α , defined by the nozzle size and the distance between source and sample, are relevant.

It is because of these drawbacks that we decided to laser focus Fe without the use of any laser collimation techniques, simply relying for this part on geometrical collimation (Fig. 6.1). We will show, that in this way periodic grids of Fe nanolines with a FWHM of 55 nm, a height of up to 6 nm, and a period of 186 nm are deposited. Thus, we prove that atoms can be focused without using laser cooling techniques for the collimation. This makes the technique suitable for atom lithography of atoms with transitions of sufficient strength. Especially for atom lithography of technologically relevant elements like Ga [9], In [10], and Si [11], for which laser collimation imposes large experimental difficulties, this would be a step forward. Also, laser focusing of molecules is feasible this way.

In Sect. 2 the theory of SW-focusing is described, which is used in a simulation of the properties of the nanolines (Sect. 3). In Sect. 4 the experimental setup used for atom lithography is described. The experimental results of atom lithography without laser collimation are compared with the outcome of the simulations in Sect. 5. The effect of the modulated Fe flux on the magnetic properties of the nanolines are discussed in Sect. 6. The flux modulation induces magnetic anisotropy in the direction perpendicular to the nanolines. Also, the possibility to magnetize the individual structures is investigated. The conclusions are listed in Sect. 7.

2 Theory

Our simulation is based on the dressed state model introduced by Dalibard and Cohen-Tannoudji [12]. In this model one considers the eigenstates of the complete atom-light

field system. The total Hamiltonian of an atom in a light field is given by:

$$H = H_{atom} + H_{light} + H_{int}, \quad (6.1)$$

with H_{atom} the Hamiltonian of the free atom and H_{light} the Hamiltonian of the light field. H_{int} represents the interaction Hamiltonian. The eigenenergies of this system are given by:

$$\begin{aligned} E_{n,+} &= (n+1)\hbar\omega_L - \frac{\hbar\Delta}{2} + \frac{\hbar\Omega}{2}, \\ E_{n,-} &= (n+1)\hbar\omega_L - \frac{\hbar\Delta}{2} - \frac{\hbar\Omega}{2}, \end{aligned} \quad (6.2)$$

with n the number of photons in the light field, ω_L the frequency of the light field, $\Delta = \omega_L - \omega_0$ the detuning of the light field from the atomic resonance ω_0 . The frequency separation between the dressed states Ω is given by:

$$\Omega = \sqrt{\omega_R^2 + \Delta^2}, \quad (6.3)$$

with $\omega_R = \Gamma\sqrt{I/2I_s}$ the Rabi-frequency, where Γ represents the natural linewidth, I the light intensity, and I_s the saturation intensity. The dressed states are a linear superposition of the ground and excited states:

$$\begin{aligned} |n, +\rangle &= \cos(\theta)|e, n\rangle + \sin(\theta)|g, n+1\rangle, \\ |n, -\rangle &= -\sin(\theta)|e, n\rangle + \cos(\theta)|g, n+1\rangle. \end{aligned} \quad (6.4)$$

Here θ is defined by:

$$\cos(2\theta) = -\Delta/\Omega. \quad (6.5)$$

In our simulation, atoms are treated as classical point particles. The energy shift of the atoms as a function of the light field intensity I and detuning Δ is:

$$U = \pm \frac{\hbar}{2} \sqrt{\frac{I(\mathbf{r})}{2I_s} \Gamma^2 + \Delta^2} - \frac{\hbar\Delta}{2}, \quad (6.6)$$

where the sign is that of the dressed state the atom is currently in. Calculating the trajectory of an atom through a light mask is now a matter of integrating its Newtonian equation of motion using the potential U above.

We describe our light mask as a one-dimensional Gaussian standing wave along the x -axis with a waist w , obtained by superposition of two travelling waves:

$$I(\vec{r}) = I_0 \sin^2(kx) \exp\left(-2\frac{z^2}{w^2}\right). \quad (6.7)$$

Here $k = 2\pi/\lambda$ is the wavenumber of the travelling wave and the propagation direction of the atoms is assumed to be along the z -axis. The central intensity is given in terms of the travelling wave power P of the laser by $I_0 = 8P/\pi w^2$.

As the atoms' kinetic energy is much larger than the potential height of the light mask we can neglect its effect on the longitudinal motion. We thus concentrate on the atoms' lateral motion, which is far slower and governed by the one-dimensional equation of motion:

$$F_x = -\frac{\partial U}{\partial x} = m \frac{\partial^2 x}{\partial t^2}. \quad (6.8)$$

Outside the standing wave the intensity I of the light is zero and the ground state is $|+\rangle$ for $\Delta > 0$ and $|-\rangle$ for $\Delta < 0$. Unless they undergo a spontaneous or non-adiabatic (NA) transition, they will stay in their initial state, and their trajectory can be calculated by integrating Eq. 6.8.

The effects of spontaneous emission are included in the model by evaluating the probability that an atom has undergone spontaneous emission at given intervals. The transition rates between the dressed states due to spontaneous emission are given by:

$$\Gamma_{+-} = \Gamma \cos^4 \theta \quad (6.9)$$

$$\Gamma_{-+} = \Gamma \sin^4 \theta, \quad (6.10)$$

with θ defined in Eq. 6.5. The probability of a dressed state transition due to spontaneous emission is given by $\tau\Gamma_{+-}$ or $\tau\Gamma_{-+}$, depending on the initial dressed state, with τ the width of the time step in the integration.

Non-adiabatic transitions occur when the atom moves too fast, or in other words, the eigenstates (dressed states) change too fast, for the internal state of the atom to follow. The atom is transferred from one dressed state to the other. They are most likely to occur when atoms cross a node. In our model we state that they occur exclusively when an atom crosses a node. An estimate for the upper limit of the NA transition probability can be found in Ref. [13]:

$$P_{+\rightarrow-} \leq \max \left\{ \frac{|\langle n, -; \mathbf{r}(t) | \frac{d}{dt} | n, +; \mathbf{r}(t) \rangle|^2}{|\Omega(\mathbf{r}(t))|^2} \right\}. \quad (6.11)$$

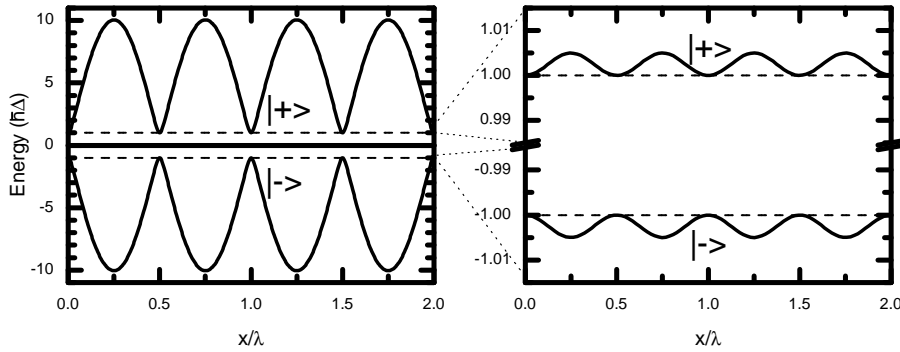


Figure 6.2: *Left*: Dressed state potentials for $\omega_R/|\Delta| = 100$. Dashed lines indicate zero-intensity levels. Note the difference in shape between the potential minima for $|+\rangle$ and $|-\rangle$ states. *Right*: Same, for $\omega_R/|\Delta| = 0.01$ [14]. In this case both potentials are equivalent.

A calculation of the upper limit of the NA transition probability when an atom moves over a node is given in Ref. [14]:

$$P_{i \rightarrow j} \lesssim \left| \frac{\mathbf{k} \cdot \mathbf{v}}{2} \frac{\omega_{R,max}}{\Delta^2} \right|^2, \quad (6.12)$$

with $\omega_{R,max}$ the Rabi-frequency at regions of highest intensity in the standing light wave, i.e., in the anti-nodes. In the calculation, the upper limit (6.12) is taken as an estimate of the transition probability. In our model we set the NA transition probability to unity if this value is larger than one, else we set it to zero. With $\omega_R/\Delta = 100$, $v_{\parallel} = 0.4$ m/s, and $|k| = 2\pi/(372 \times 10^{-9})$ m⁻¹ this upper limit amounts to 0.13, so the NA transition probability is set to zero in the simulation.

Before we show the results of these semiclassical simulations, we discuss the potential that is used. The left part of Fig. 6.2 displays the potential for the case of a very strong light field, where $\omega_R/|\Delta| = 100$. The case of a very weak light field with $\omega_R/|\Delta| = 0.01$ is displayed to the right. Both potentials are very different in shape as well as in magnitude. In the strong field limit, the potential minima of the $|+\rangle$ state differ radically in shape from those of the $|-\rangle$ state. The minima of the $|-\rangle$ state are smooth, broad and parabolic over a large range around the minima. Using such a potential is a way to avoid non-parabolic aberrations in the atom focusing process. On the other hand, the minima of the $|+\rangle$ state are unparabolic, looking more like a V-shaped potential. The result of this shape is that the oscillation period of the atoms in the potential depends on the starting point of the oscillation. This V-shaped potential creates focal lines rather than focal points, as the starting position of the atoms in the potential is homogeneously distributed. Hence, the formation of structures should be far less sensitive to the experimental parameters.

The potential for a weak standing wave is sine-like. The difference in shape between the $|+\rangle$ and $|-\rangle$ state minima has vanished, and focusing is expected to proceed in a similar fashion for both states. For positive detuning, the atoms start out in the $|+\rangle$ state, and due to the low spontaneous emission rate, they stay in that state. Hence the atoms get focused in the potential minima by a sine-like potential. For negative detuning, the same story applies, except that the sine-like potential now focuses the atoms in the intensity maxima.

3 Simulation

For the calculation we start with 10000 atoms that are homogeneously distributed over a single wavelength in the x -direction. The transverse velocity distribution of the uncooled beam emerging from a round nozzle is approximated by a Gaussian. The longitudinal velocity distribution of the atomic beam is that of an effusive beam, i.e., a Maxwell-Boltzmann distribution. The longitudinal velocities are assigned in a regular sequence conforming to the chosen distribution; all other parameters are chosen randomly for each trajectory.

We incorporate the magnetic substructure of the transition used by assigning each atom to a random substate, after which the calculation is performed using the appropriate Clebsch-Gordan coefficient for each atom. We assume that the light is linearly polarized.

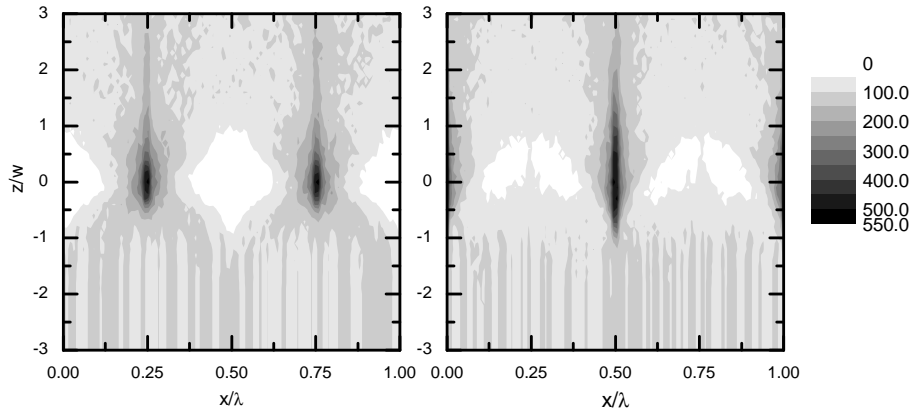


Figure 6.3: Flux distribution of an atomic beam passing from below through a strong light mask $\omega_R/|\Delta| = 100$. *Left:* $\Delta < 0$ generates focal points, i.e., the size of the focus is approximately one beam waist in the z -direction. *Right:* $\Delta > 0$ results in focal lines, i.e., the focus is spread over more than two beam waists. This difference in flux distribution is due to the difference in potential as shown on the left side of Fig. 6.2.

The equation of motion of every atom is integrated over a set distance, before we check for spontaneous and NA transitions. The effect of both transitions is to change from one dressed state to the other. The possibility that atoms, which undergo a spontaneous emission, decay to a different magnetic substate, is neglected. We make a histogram of the atomic flux distribution at set intervals.

To demonstrate the difference in focusing between the negative and positive detuning, we simulate with a perfectly collimated atom beam that interacts with a strong standing wave. The longitudinal velocity distribution is taken to be at $T=2000$ K. The light mask is a one dimensional standing light wave with a power for each of the counter-propagating beams of 50 mW in a 50 μm radius beam waist at a detuning $|\Delta|$ of $150(2\pi)$ MHz (58 Γ). For these experimental parameters $\omega_R/|\Delta| \approx 100$. The results are shown in Fig. 6.3. Interaction with a red-detuned standing wave generates focal points, as shown on the left. The blue-detuned standing wave gives rise to focal lines, as shown on the right. For blue detuning, some 4500 dressed state-changing spontaneous emissions occur, meaning that the majority of atoms does not undergo any spontaneous emission. For red detuning, some 7000 dressed state-changing spontaneous emissions occur, reflecting the fact that atoms are attracted to intensity maxima in this case, where the absorption rate is higher. The strength of the lenses varies per atom. This is due mainly to the spread in Clebsch-Gordan coefficients for the Fe atoms; secondarily, the longitudinal velocity spread of the Fe atoms also contributes. The relatively long z -range over which atom focusing occurs for the blue detuned case stands out.

4 Experimental setup

In Fig. 6.4 a schematic overview of the experimental setup is given. An Fe atomic beam is produced using an Al_2O_3 crucible with a nozzle diameter of 1 mm heated to a temperature of 2000 K by a carbon spiral heater [15], resulting in a typical Fe density in the source of $n_{Fe} = 4 \times 10^{20} \text{ m}^{-3}$. At this temperature the Fe-beam intensity is typically $I_{Fe} =$

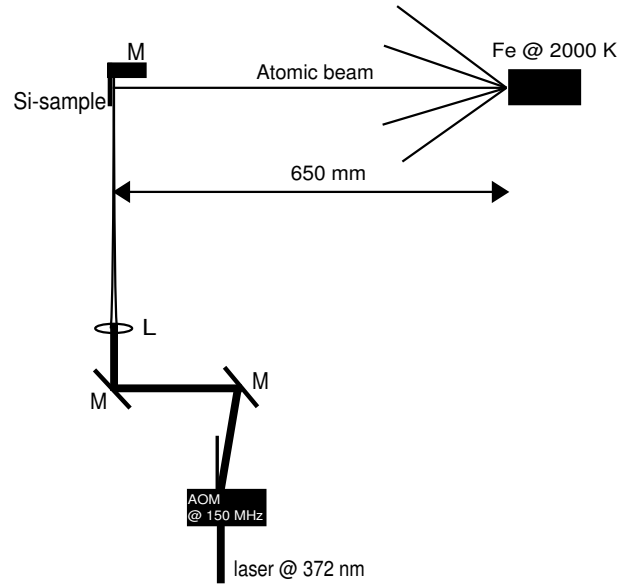


Figure 6.4: Scheme of the setup. Fe atoms emerge from an Al_2O_3 crucible at a temperature of 2000 K. The atoms are focused 650 mm downstream by a standing light wave detuned $150(2\pi)$ MHz from resonance by an AOM.

$2.5 \times 10^{16} \text{ s}^{-1}\text{sr}^{-1}$, and the average longitudinal velocity is $(8k_B T/\pi M)^{1/2} = 870 \text{ m/s}$. The isotope ^{56}Fe has a natural abundance of 91.8 %, of which at a temperature of 2000 K ≈ 50 % is still in the $^5\text{D}_4$ ground state. Hyperfine structure is absent in ^{56}Fe , since the nuclear spin is zero.

The $^5\text{D}_4 \rightarrow ^5\text{F}_5$ ($\Gamma = 2.58(2\pi)$ MHz) atomic transition at 372 nm is suitable for the SW-focusing of Fe atoms. A Ti:S laser, frequency doubled with an LBO-crystal in a ring cavity, is used for this purpose. This laser system is locked to the transition using a hollow cathode discharge cell, described in [16], and Chapter 3.

The Fe atoms are deposited on a native oxide Si[100] substrate, 650 mm downstream from the nozzle, resulting in a deposition rate of 3 nm/hour, determined by deposition through a mechanical mask (Section 5). The Si samples can be 3 to 8 mm wide and 2

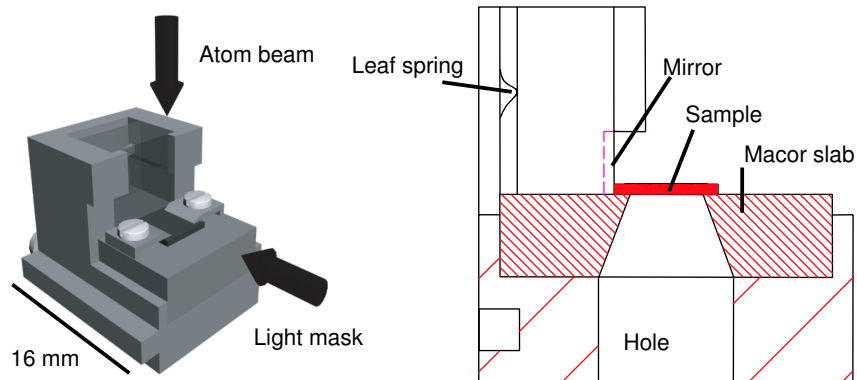


Figure 6.5: Left: sample holder. Right: cross section of sample holder. The Si sample is clamped to a macor isolator that is screwed to the steel frame. The mirror is pressed to the frame by a spring.

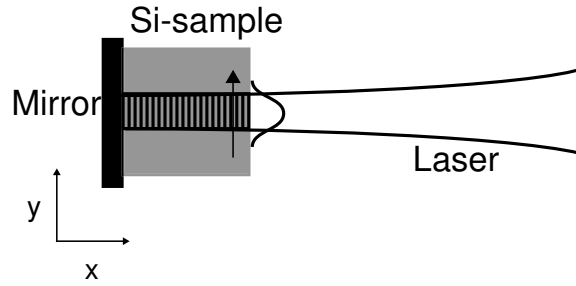


Figure 6.6: The height and width of the nanolines are investigated as a function of position along the nanolines. Since the laser beam is Gaussian, each position corresponds to a specific light intensity.

to 10 mm long. The Si sample is clamped on a compact sample holder (Fig. 6.5), on which also an $8 \times 8 \times 3$ mm mirror is mounted. These sample holders can easily be removed from the deposition chamber and stored in a load lock by a magnetic translator so that the alignment of sample and mirror, which have to be perpendicular to each other within 1 mrad, can be done *ex vacuo*. The pressure in the deposition chamber is typically 1×10^{-8} mbar.

An Acousto-Optical Modulator (AOM) is used to detune the light $150(2\pi)$ MHz from resonance. To create the standing light wave, the laser beam is focused to a waist of $50 \mu\text{m}$ parallel to the atomic beam and $80 \mu\text{m}$ perpendicular to the atomic beam, located at the surface of the sample holder mirror. The light is linearly polarized.

To prevent Fe from oxidizing, a Ag capping layer of approximately 5 nm is deposited using an effusive source operated at a typical temperature of 1140 K, resulting in a deposition rate of 0.15 nm/min.

5 Results

We investigate the height and width of the nanolines as function of overall position along a direction perpendicular to the propagation direction of the light, i.e., intensity along

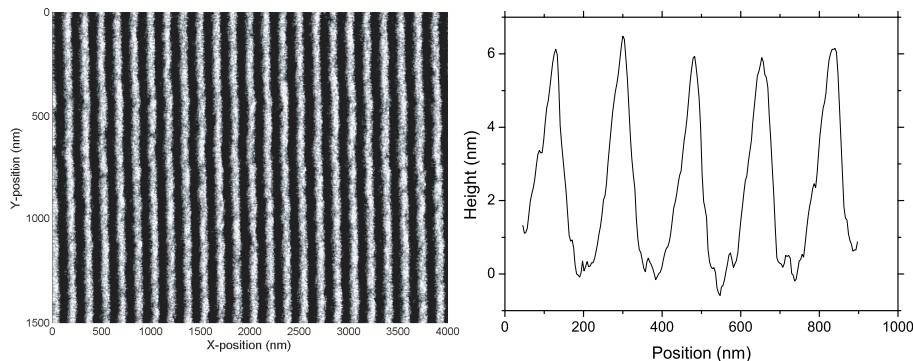


Figure 6.7: *Left*: $4 \times 1.5 \mu\text{m}$ AFM-scan of the nanolines. *Right*: $1 \mu\text{m}$ line-scan, averaged over 40 nm in the Y-direction. The deposition time is 2 hours. The height of the structures in this image is 6 nm and their FWHM width approximately 60 nm. The laser power is $P=50$ mW, 10 % of the laser beam is cut-off by the Si substrate.

the standing light wave parallel to the mirror and substrate (Fig. 6.6). Since we have an AOM with a fixed RF-frequency at $150(2\pi)$ MHz, our measurements are limited to blue and red detuned focusing at this frequency shift from resonance.

In Fig. 6.7 a $4 \times 1.5 \mu\text{m}$ AFM scan of the nanolines is shown. In 2 hours deposition time we grow structures up to heights of 6 nm. The distance between the 1 mm diameter nozzle of the crucible and the substrate is 650 mm. Therefore, the collimation of the Fe atomic beam amounts to 0.4 mrad RMS. The width of the lines is calibrated by comparing the average of the widths of the peaks in a $1 \mu\text{m}$ line-scan to the pitch of the modulation, which amounts to $\lambda/2=186$ nm.

Lines are deposited with the standing light wave cut in half by the substrate. In this case, however, diffraction of the laser beam by the substrate may cause problems. Therefore we have also deposited nanolines with the laser beam passing just above the substrate, cutting only slightly in the tail of the Gaussian beam. Both cases are schematically drawn in Fig. 6.8. In Fig. 6.9 a typical height profile is shown. For high intensities, the height of the nanolines is largely independent on the light intensity both in experiment and simulation: the height profile does not follow the Gaussian shaped laser intensity profile, but it has a broad flat top. The height of the potential shown in Fig. 6.2, and described in Eq. 6.6 follows the square-root of the intensity. Also, at low intensities the atoms are not yet focused at the 50 % cut-off position ($z = 0$ in Fig. 6.3). Increasing the intensity will move the focus over the $z = 0$ point towards negative z -values. Since the lens, especially in the blue detuned case has a large focal depth, the atoms remain focused at the $z = 0$ position, even for higher intensities, resulting in the flat top of the height profile. At low intensities, the measurements deviate somewhat from the simulations, probably due to non-Gaussian tails in the spatial profile of the laser beam used in the experiment.

The width of the structures as function of the position on the substrate is shown in Fig. 6.10. We have chosen the simulation parameters such that they give a good representation of the experimental conditions, however, diffraction due to the cut-off is not included in the simulation. Also, slight misalignments of the laser beam are not included in the simulation.

For high intensities, blue detuning results in slightly narrower lines compared to red detuning in the experiment. This difference is more pronounced in the simulations, and results from different focusing potentials (Fig. 6.2). The match between measured and simulated widths is better in the 10 % cut-off configuration than in the 50 % cut-off

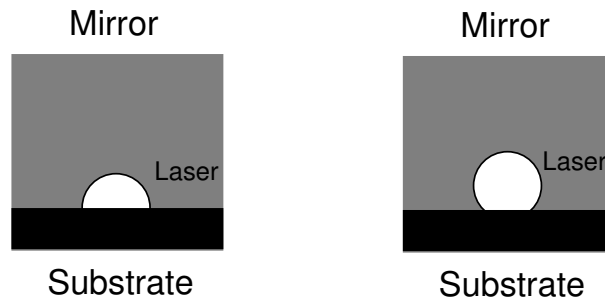


Figure 6.8: The cut-off of the laser beam by the substrate. *Left*: The laser beam is cut in half by the substrate. (50 % cut-off) *Right*: Only 10 % of the laser beam is cut off by the substrate. (10 % cut-off)

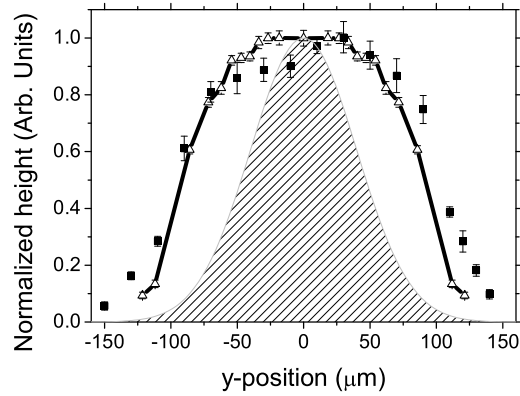


Figure 6.9: Typical height profile as a function of position along the lines for a blue detuned 50 % cut-off laser beam. Both simulation data and experimental data are normalized to their maximal height. The squares are the measurements, the triangles are the simulation. The patterned profile reflects the dependence of the standing wave intensity on position. The laser power is $P=50$ mW.

configuration. Diffraction of the laser beam is not included in the simulation, apparently resulting in an underestimate of the nanoline widths in the 50 % cut-off simulation.

For further analysis of the Fe nanolines regarding for instance their magnetic properties, a good knowledge of the background layer thickness is necessary. To measure the ratio between the background layer and the height of the lines, Fe is deposited through a mechanical mask. The mask is made by e-beam lithography of a SiN membrane. Lines have been etched in the membrane with a width of about 150 nm and a period of 744 nm over an area of $250 \times 250 \mu\text{m}$. The mask is pressed onto the substrate with only a metal foil of $100 \mu\text{m}$ as spacer between the bottom of the mask and the front of the substrate. Deposition through such a mask results in background-free nanolines, and thus gives a direct measurement of the total deposited layer thickness. A SEM-scan of the mask and an AFM-scan of the Fe-lines grown through the mask are shown in Fig. 6.11. The FWHM width of the structures is about 150 nm. The height of these lines are compared to the height of the focused nanolines for equal Fe atomic beam flux and deposition times. In our experiment the ratios for all experimental conditions are close to 50 % for the lines at the top of the height profile.

Table I: Simulation results of the ratio of the height of the lines to the average layer thickness.

	red	blue
50% cut-off	125%	125%
10% cut-off	60%	70%

In Table I the ratio between simulated line heights at the top of the laser intensity, which is close to maximal height, and the thickness of the unmodulated deposited layer are listed. In the calculation of the ratio we assume that 50 % of the atoms are in the $^5\text{D}_4$ ground state, which is the thermal occupation of the ground state at a source temperature of

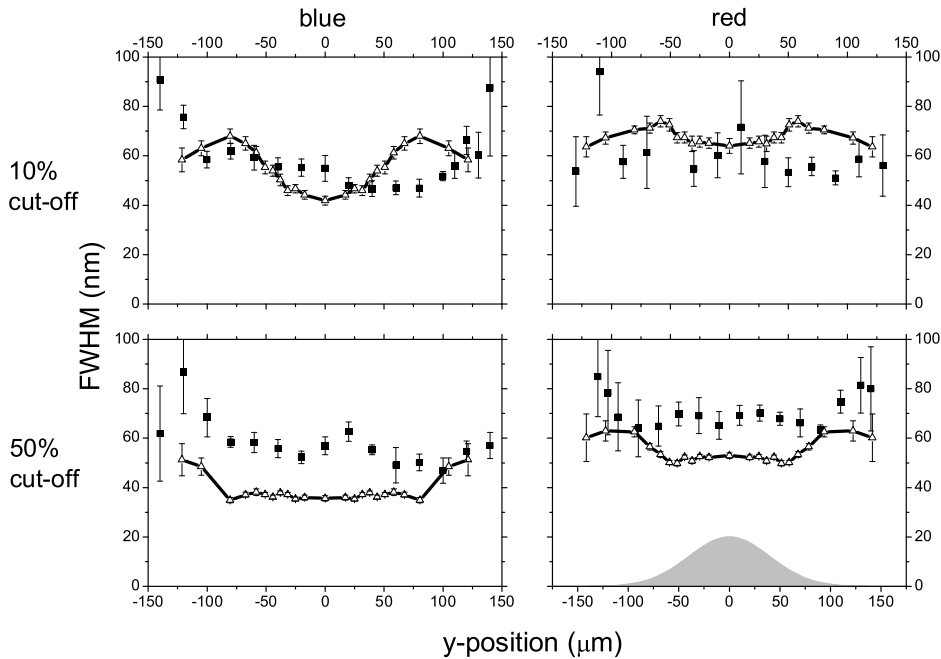


Figure 6.10: FWHM of the lines as a function of position along the lines for blue and red detuning. The squares are the measurements. Simulations are indicated by the triangles. In the lower right graph, the laser intensity profile as used in the simulations is shown.

2000 K. For the 10 % cut-off setting this is close to the predicted value. For the 50 % cut-off case, the experimental ratio is much lower than the simulated ratio. This discrepancy between measurement and simulation for the 50 % cut-off case is also present in the widths of the lines: the width of the simulated nanolines is smaller than the width of the deposited nanolines. This means that the quality of the deposited nanolines in the 50 % cut-off case is much lower than what can ideally be achieved. We attribute this to a large diffraction of the laser beam in the 50 % cut-off case which is not included in the simulations.

6 Magnetic properties of nanolines

The tool for studying magnetism on the nanoscale is the Magnetic Force Microscope (MFM), which can be used to probe the magnetization of individual lines. The effect of their presence on the global magnetization of the layer can be measured by using the Magneto-Optical Kerr Effect (MOKE). More specific, the magnetic anisotropy that occurs due to their presence can be measured with MOKE [14]. We show results for both cases.

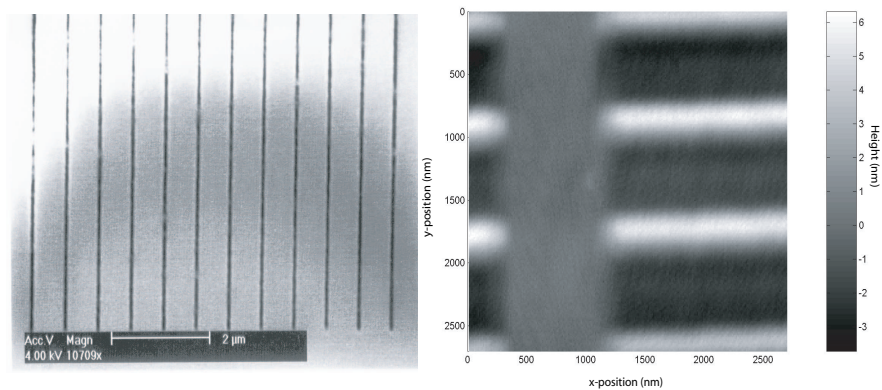


Figure 6.11: *Left*: SEM-scan of the SiN mask. The pitch of the lines is 744 nm. *Right*: AFM-scan of the deposited Fe-lines through the mask (90 degrees rotated). Deposition time is two hours.

MOKE

In the MOKE setup the polarization of a linearly polarized HeNe-laser beam is rotated (Kerr-rotation) upon reflection from the surface of a magnetized layer. The HeNe-laser beam has a waist on the order of $100\ \mu\text{m}$. A sample with nanolines up to 8 nm high and unmodulated Fe-layer thickness of about 16 nm, is placed in a in-plane variable magnetic field. The magnetic field is ramped from $-0.4\ \text{T}$ to $0.4\ \text{T}$. After each ramp the sample is moved by $20\ \mu\text{m}$ perpendicular to the magnetic field direction, and this over a total displacement of 2 mm. We make sure that we scan over the area with the nanolines. To detect magnetic anisotropy, two series of measurements are made: one with the magnetic field parallel to the nanolines, the other with the magnetic field perpendicular to the lines. In Fig. 6.12 a typical measurement is shown. Rotating the sample clearly makes a difference. The coercivity field H_c is larger for a magnetic field orientation perpendicular to the lines. For the magnetic field orientation parallel to the lines the coercivity field equals $14 \pm 1\ \text{mT}$, for the perpendicular orientation the coercivity field amounts to $28 \pm 1\ \text{mT}$. This is lower than the 90 mT reported in [14], most likely due to a different thickness of the Fe layer. The difference in remanence between both orientations is approximately $0.06\ M_s$. This magnetic anisotropy is present over the entire sample and not only where the lines are focused by the standing light wave. It is thus most likely not a manifestation of the presence of the nanolines but of a preferred crystalline orientation of the deposited Fe layer probably along a specific axis of the native oxide Si[100] substrate.

MFM

With the MFM the magnetic properties of the individual lines can be measured. An MFM is basically an atomic force microscope (AFM) with a magnetic tip, which interacts with the magnetic field of the nanostructures. During an MFM-scan the distance between tip and surface is set at 200 nm to distinguish between van der Waals-forces and magnetic forces. Typically, the magnetic domain on the MFM-tip is on the order of 50 nm limiting the resolution of an MFM approximately to this value. The resolution of the MFM is thus basically equal to the width of our nanolines. In Fig. 6.13 AFM- and MFM-scans at a

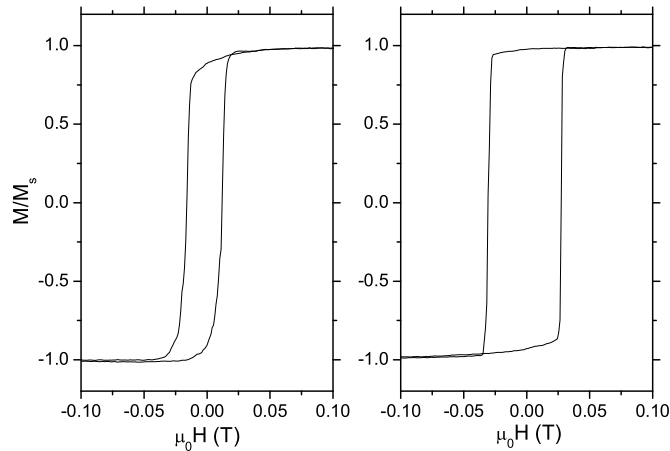


Figure 6.12: Magnetization normalized to the saturation magnetization M_s measured by MOKE. *Left*: Magnetic field parallel to the lines. *Right*: Magnetic field perpendicular to the lines in the plane of the substrate.

magnetic field of 0.01 T perpendicular to the lines are shown, both for SW-focused lines as for lines made by deposition through masks. The magnetic field is chosen perpendicular to the nanolines, since we expect the exchange and magnetic dipole contributions in this configuration to be much larger than in the case of a parallel magnetization of the nanolines [14].

In the MFM-image of the SW-focused lines features are visible which are far below the resolution of the MFM. These features are thus not a likely result of magnetic interaction. Since they have the same structure as the features in the AFM image, we assume this is a signature of the topography of the surface. For the mechanical mask depositions the MFM-scan shows the expected signature of magnetic properties of the individual lines. In this case the separation (744 nm) and width (150 nm) are much larger than the MFM resolution. Also, these lines have no Fe-background, so they act like individual magnets. Their magnetization is oriented along the direction of the applied magnetic field.

7 Conclusions

By direct-write atom lithography Fe-nanolines are deposited with a pitch of 186 nm and a FWHM width of 50 nm, without the use of laser collimation techniques. Sufficient collimation is obtained by strong geometrical collimation: a relatively large distance (650 mm) between Fe-source and sample compared to the 1 mm source nozzle. In this way the divergence of the atoms arriving at the sample is reduced to 0.4 mrad RMS.

Experiments and simulations are performed with the focusing standing light wave cut in half by the substrate and with a 10 % cut-off by the substrate. Experiments and simulations are in good agreement with respect to the height of the nanolines. The experimental width of the nanolines and simulations are in good agreement for the 10 % cut-off case. For the 50 % cut-off case the measured width of the lines is larger than

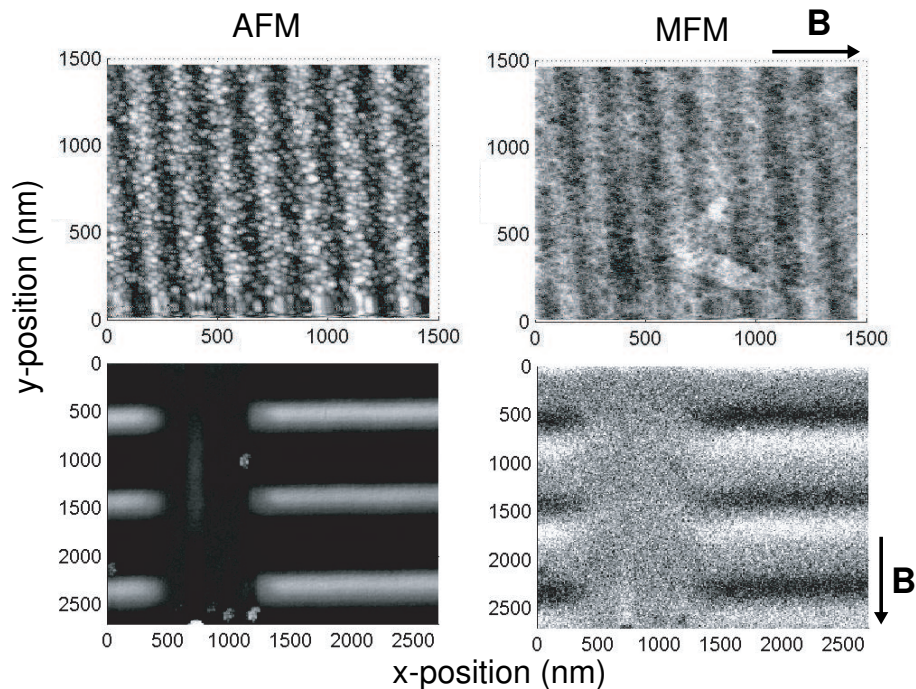


Figure 6.13: AFM- and MFM-scans of both SW-focused lines (*top images*) and lines made by deposition through mechanical masks (*bottom images*). Arrows indicate the orientation of the external magnetic field. The gray-scale represents the height for the AFM-scans, and the magnetization for the MFM-scans.

the simulated value. Also, the measured height of the lines versus average deposited layer thickness ratio is lower than in the simulations in that case. We attribute this discrepancy to diffraction of the light beam by the substrate and small misalignments of the SW. With a MOKE-setup we could verify that the deposited Fe-layer is ferromagnetic. Magnetic anisotropy could be detected, however the anisotropy is present over the entire sample, not only where lines are deposited. We suggest this anisotropy is more a consequence of a preferred crystalline orientation. Magnetization of the individual lines could not be measured by MFM. We attribute this to the resolution of the MFM, which is on the order of the width of the nanolines, and to the large Fe background. Background-free nanolines are deposited with SiN mechanical masks. With an MFM, magnetization of such lines is visualized.

Acknowledgement

This work is financially supported by the Dutch Foundation for Fundamental Research on Matter (FOM). Thanks to Leon van Dijk for analyzing the lines, and Corine Fabrie, Oleg Kurnosikov, and Henk Swagten for the MOKE and MFM measurements and useful discussions.

References

- [1] G. Timp, R.E. Behringer, and D.M. Tennant, J.E. Cunningham, Phys. Rev. Lett. **69**, 1636 (1992).
- [2] J.J. McClelland, R.E. Scholten, E.C. Palm, and R.J. Celotta, Science **262**, 877 (1993).
- [3] U. Drodofsky, J. Stuhler, Th. Schulze, M. Drewsen, B. Brezger, T. Pfau, and J. Mlynek, Appl. Phys. B **65**, 755 (1997).
- [4] R.W. McGowan, D.M. Giltner, and S.A. Lee, Opt. Lett. **20**, 2535 (1995).
- [5] R. Ohmukai, S. Urabe, and M. Watanabe, Appl. Phys. B, **77**, 415-419 (2003).
- [6] E. te Sligte, B. Smeets, K. M. R. van der Stam, R. W. Herfst, P. van der Straten, H.C.W. Beijerinck, and K.A.H. van Leeuwen, Appl. Phys. Lett. **85**, 4493 (2004).
- [7] G. Myszkiewicz, J. Hohlfeld, A.J. Toonen, A.F. Van Etteger, O.I. Shklyarevskii, W.L. Meerts, Th. Rasing, and E. Jurdik, Appl. Phys. Lett. **85**, 3842 (2004).
- [8] B. Smeets, R.W. Herfst, L.P. Maguire, E. te Sligte, P. van der Straten, H.C.W. Beijerinck, K.A.H. van Leeuwen, Appl. Phys. B **80**, 833 (2005).
- [9] S.J. Rehse, K.M. Bockel, and S.A. Lee, Phys. Rev. A **69**, 063404 (2004).
- [10] H. Leinen, D. Glässner, H. Metcalf, R. Wynands, D. Haubrich, and D. Meschede, Appl. Phys. B, **70**, 567 (2000).
- [11] T. Fujii, H. Kumagai, K. Midorikawa, and M. Obara, Opt. Lett, **25**, 14571459 (2000).
- [12] J. Dalibard and C. Cohen-Tannoudji, J. Opt. Soc. Am. B **2**, 1707 (1985).
- [13] A. Messiah, *Mécanique Quantique II*, Dunod, Paris (1964).
- [14] E. te Sligte, *Atom Lithography of Iron*, Ph.D. Thesis, TU/e (2005).
- [15] R.C.M. Bosch, H.C.W. Beijerinck, P. van der Straten, and K.A.H. van Leeuwen, Eur. Phys. J. Appl. Phys., **18**, 221 (2002). The atomic beam source described in this paper is used in thermal mode.
- [16] B. Smeets, R.C.M. Bosch, P. van der Straten, E. te Sligte, R.E. Scholten, H.C.W. Beijerinck, K.A.H. van Leeuwen, Appl. Phys. B **76**, 815 (2003).

Chapter 7

Efficient blue light generation in Rb

We demonstrate continuous coherent blue laser light production using a five-level lasing-without-inversion scheme in rubidium vapor. Two low-power lasers (15 mW) at 780 nm and 776 nm induce a strong atomic coherence in the 5S-5P-5D states. The atoms decay to the 6P excited state from which stimulated emission to the ground state produces a coherent beam of blue (420 nm) light of 40 μW , several times greater than previously reported. Also, this scheme is more efficient by several orders of magnitude compared to conventional frequency up-conversion in non-linear crystals.

¹This experiment was performed in the optics group of R.E. Scholten, School of Physics, University of Melbourne.

1 Introduction

Nonlinear interactions of light and atoms can be enhanced dramatically through appropriate control of the quantum state of the atoms, in particular through coherent superposition of the unperturbed atomic eigenstates [1]. Electromagnetically induced transparency (EIT) [2] and lasing without inversion [3] are practical examples of such control which have attracted considerable interest. Recently, Zibrov *et al.* showed that efficient cw frequency up-conversion is possible in a ^{87}Rb -vapor [4], by creating a large coherence on a two-photon cascade transition. Compared to conventional frequency up-conversion in non-linear crystals, this scheme is more efficient by several orders of magnitude at incident powers on the order of 10 mW. Atomic coherence could conceivably be used to produce light for atom imaging, laser cooling, or plugging leaky transitions.

We have extended the Zibrov scheme by producing coherent blue radiation using a five-level scheme in ^{85}Rb vapor. The relevant levels are shown in Fig. 7.1. Two low-power lasers at 780 nm and 776 nm induce a strong atomic coherence in the 5S-5P-5D states. Due to this coherence, two coherent fields are generated at $5.5\ \mu\text{m}$ and 420 nm corresponding to the $6\text{P}_{3/2}$ - $5\text{D}_{5/2}$ and $5\text{S}_{1/2}$ - $6\text{P}_{3/2}$ transitions, respectively [4]. We are able to couple both ground-state hyperfine levels ($F=2,3$) by the two-photon transition to the 5D state. Coherent radiation on the $5\text{S}_{1/2}$ - $6\text{P}_{3/2}$ transition is generated when both lasers are tuned close to the two-photon resonance ($\delta_{780} = -\delta_{776}$) and the phases of both cascade paths match ($\mathbf{k}_{5.5} + \mathbf{k}_{420} = \mathbf{k}_{780} + \mathbf{k}_{776}$), with δ the detuning of the laser frequency from resonance, and \mathbf{k}_n the wavevector of the light. The refractive index of the Rb-vapor for both driving fields, and thus the phase matching is strongly dependent on the detuning of the driving fields from their single-photon resonance frequencies, and from the detuning of their sum frequency from the two-photon resonance. We show that coherent blue light generation is an interplay of large two-photon coherence and proper phase matching, reaching blue light powers several times greater than previously reported, up to $40\ \mu\text{W}$. In Sect. 2 the theory

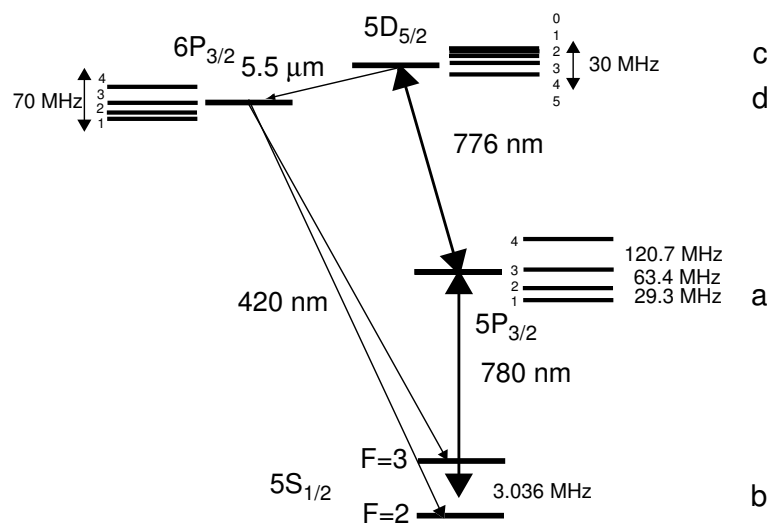


Figure 7.1: The relevant atomic levels in ^{85}Rb . Two low-power lasers at 780 nm and 776 nm induce a strong atomic coherence in the 5S(b)-5P(a)-5D(c) states. This coherence induces lasing on the $5.5\ \mu\text{m}$ and 420 nm transition.

of blue light generation is discussed. The experimental setup is described in Section 3. In Sect. 4 the results of the blue light generation are discussed. The conclusions are given in Sect.5.

2 Theoretical framework

To understand the origin of the coherent blue radiation, we consider interaction of the Rb-system with four optical fields. The crucial factor is the dipole forbidden two-photon coherence between state $|b\rangle$ and state $|c\rangle$, which is induced by the two driving fields. Ideally, when dephasing of the upper state $|c\rangle$ can be neglected, the atomic state can be written like:

$$|\phi\rangle = \cos\theta|b\rangle + \sin\theta|c\rangle, \quad (7.1)$$

if the sum frequency of both driving fields is tuned close to the two-photon transition. This state corresponds to maximal coherence $|\rho_{bc}|^2 = \rho_{bb}\rho_{cc}$ and results in a large population of the excited state $|c\rangle$. The coherence ρ_{bc} is actually a travelling wave $\rho_{bc} = \bar{\rho}_{bc} \exp(ik_{bc}z)$, with wavevector k_{bc} equal to the sum of the wavevectors of the driving fields modified with their refractive indices.

Consider two optical fields E_1 and E_2 , with E_1 tuned close to the 420 nm transition and E_2 close to the 5.5 μm transition. We consider the propagation of both fields in the coherently driven medium. For that purpose, the Maxwell-Bloch (MB) equations should be solved. The relevant MB-equations are [4]:

$$\frac{\partial E_1}{\partial z} = (\kappa_1 \frac{\rho_{dd} - \rho_{bb}}{\Gamma_{db}} + i\delta\mathbf{k})E_1 - \frac{\kappa_1}{\Gamma_{db}} \bar{\rho}_{cb} E_2^*, \quad (7.2)$$

$$\frac{\partial E_2^*}{\partial z} = (\kappa_2 \frac{\rho_{cc} - \rho_{dd}}{\Gamma_{dc}})E_2^* + \frac{\kappa_2}{\Gamma_{dc}} \bar{\rho}_{bc} E_1. \quad (7.3)$$

Here, ρ_{ii} are populations of atomic states and Γ_{ij} are complex relaxation rates of optical coherences. The quantity $\delta\mathbf{k} = \mathbf{k}_1 + \mathbf{k}_2 - \mathbf{k}_{bc}$ is the wavevector mismatch. Terms proportional to populations describe linear gain and loss as well as phase shifts. Terms proportional to coherences are creating nonlinear cross coupling between fields. The quantities $\kappa_1 = 3N\lambda_1^2\gamma_{d\rightarrow b}/(4\pi)$, and $\kappa_2 = 3N\lambda_2^2\gamma_{c\rightarrow d}/(4\pi)$ are the coupling constants of the corresponding transitions, with $\gamma_{i\rightarrow j}$ the decay rates of the corresponding transitions, and N the Rb atom number density. Since E_1 is in the blue and E_2 in the infrared, $\kappa_2 \gg \kappa_1$. Studying the eigenvalues of two normal modes corresponding to the MB-equations can result in interesting insight in the propagation of the two fields. When absorption of the driving fields can be neglected, the eigenvalues of the MB-equations are [4]:

$$\Lambda_{1,2} = a \mp \left[a^2 - \frac{\kappa_1\kappa_2}{\Gamma_{dc}\Gamma_{db}} |\rho_{bc}|^2 - \kappa_2 \frac{\rho_{cc} - \rho_{dd}}{\Gamma_{dc}} (\kappa_1 \frac{\rho_{dd} - \rho_{bb}}{\Gamma_{db}} + i\delta k) \right]^{1/2}, \quad (7.4)$$

where $a = [\kappa_1(\rho_{dd} - \rho_{bb})/\Gamma_{db} + i\delta k + \kappa_2(\rho_{cc} - \rho_{dd})/\Gamma_{dc}]/2$.

In the idealized limit with all intermediate level populations taken zero, i.e., $\rho_{aa} = \rho_{dd} = 0$, coherence is maximal ($|\rho_{bc}|^2 = \rho_{bb}\rho_{cc}$), and $\delta\mathbf{k} = 0$. The last condition can easily be achieved due to the large dispersion near two-photon resonance. The two eigenvalues

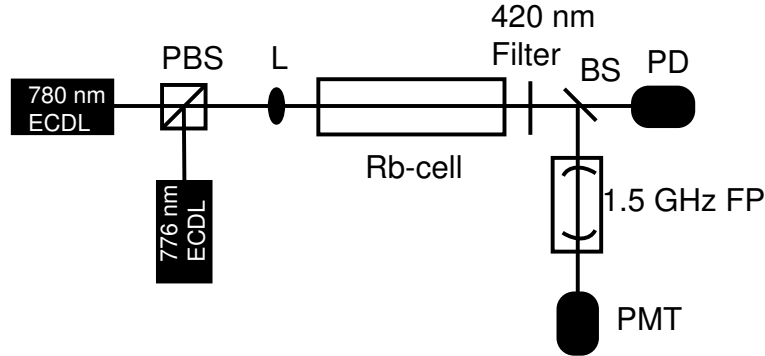


Figure 7.2: Schematic view of the setup. Two low-power external-cavity co-propagating diode lasers are coupled into a Rb vapor cell by a $f=200$ mm lens(L). The IR-light is filtered out and the blue light is analyzed by a photodiode (PD) and a scanning Fabry-Perot etalon (FP). The transmission of the etalon is measured with a photomultiplier tube (PMT).

then become $\Lambda_1 = 0$, and $\Lambda_2 = a$. The fact that the first eigenvalue is zero represents the unperturbed propagation of the two fields through the phase-coherent medium, equivalent to electromagnetically induced transparency (EIT). Stability is ensured by large absorption of the second eigenmode ($\text{Re}(\Lambda_2) < 0$). However, such a unperturbed propagation is unstable in a cascade medium. With $\Gamma_{ij} = (\gamma_{ij}^2 + \Delta_{ij}^2)/\gamma_{ij}$, the real part of the second eigenvalue $\text{Re}(\Lambda_2)$ is equal to:

$$\text{Re}(\Lambda_2) = \frac{\kappa_2 \gamma_{dc}}{\gamma_{dc}^2 + \Delta_{dc}^2} \rho_{cc} - \frac{\kappa_1 \gamma_{db}}{\gamma_{db}^2 + \Delta_{db}^2} \rho_{bb} > 0, \quad (7.5)$$

where Δ_{ij} is the detuning from the resonance frequency of transition $|j\rangle \rightarrow |i\rangle$. When the sum of the two linear gain coefficients for the 420 nm and 5.5 μm light respectively is larger than zero, two properly phased pairs of fields can be exponentially amplified. In other words, light amplified by a phase-insensitive gain mechanism on the $|c\rangle \rightarrow |d\rangle$ transition beats with the two-photon coherence ρ_{bc} , generating coherent radiation near resonance with the $|d\rangle \rightarrow |b\rangle$ transition. Since $\kappa_2 \gg \kappa_1$ this gain can be very large. In our setup, only driving fields are present, thus the seed blue light is generated spontaneously. In our case fields E_1 and E_2 are initially components of the spontaneously emitted radiation at 420 nm and 5.5 μm , respectively.

3 Setup

Figure 7.2 shows a schematic view of the experimental arrangement. Two low-power external-cavity infrared diode lasers co-propagate through a 100 mm long heated rubidium vapor cell, with natural isotopic abundance of ^{85}Rb and ^{87}Rb and no buffer gas. The power in each laser beam is approximately 15 mW, focused to a beam waist of 50 μm . The laser wavelengths are close to the 5S–5P (780 nm) and 5P–5D (776 nm) transitions. With the lasers tuned to the two-step excitation resonance, strong blue fluorescence is observed, indicating significant excitation to the long-lived upper 5D level (lifetime $\tau_{5D} = 240$ ns). The atoms decay via the 6P intermediate state to the ground state ($\tau_{6P} = 112$ ns) emitting 420 nm blue fluorescence. The frequency of the 780 nm laser is determined by saturated

absorption on another Rb vapor cell. The frequency of the 776 nm laser is measured by counter-propagating 780 nm and 776 nm light beams, with an intensity $I \approx I_s$, through another Rb-vapor cell and detecting the blue fluorescence with a photomultiplier tube (PMT). In such a counter-propagating setup, blue fluorescence is only detected when both lasers are tuned such that their sum frequency equals the two-photon resonance frequency, i.e., when both lasers have opposite detuning with respect to their single photon resonances. The frequency resolution is approximately the linewidth of the 5S–5P transition ($\Gamma_{5P} \approx 6(2\pi)$ MHz). The first Rb vapor cell can be heated uniformly up to 250 °C to increase the Rb vapor density. After infrared light is filtered out, the intensity of the blue light is measured with a photodiode. To study the frequency components of the blue light a confocal Fabry-Perot etalon is used with a FSR of 1.50 ± 0.03 GHz. The length of the FP-cavity is scanned by mounting one of the mirrors on a piezo stack. The transmission of the etalon is measured with a photomultiplier tube (PMT).

4 Results and discussion

In Fig. 7.3 the coherent blue output is shown as a function of the detuning of the 780 nm laser. The spatial profile of this blue beam is Gaussian, determined by the shape of the pump beams. Frequency reference for the 780 nm laser is obtained by saturated absorption on a separate Rb cell: at 0 and 3 GHz the 780 nm laser is coupled to the F=3 and F=2 hyperfine level of the ground state, respectively. Coherent blue output is not only observed near the single-photon resonances of both IR lasers (Output (1) and (4)), but also at frequencies in between the single-photon resonances of the two ground state hyperfine levels. Moreover, to obtain high blue output powers at these frequencies, the 776 nm laser should be tuned such that the sum frequency of both IR lasers is close to the two-photon transition. This suggests that output (2) is a coupling to the F=3 hyperfine level of the ground state, since the 776 nm is approximately -2 GHz detuned, and output (3) is a coupling to the F=2 hyperfine level of the ground state, since the 776 nm laser in that case is 1 GHz detuned from the 5P–5D transition. Since both transitions are highly saturated, we assume that the driving fields are coupled to all possible hyperfine levels of the excited states.

Coherent blue output is only present in broad frequency windows of the 780 nm laser. Blue output is strongly dependent on phase matching, since the two-photon coherence $\rho_{bc} = \bar{\rho}_{bc} \exp(ik_{bc}z)$ is a travelling wave, and thus dependent on the wavevectors of both IR lasers. Close to resonance, the refractive index is dispersive and depends strongly on detuning. When the wavevector of the coherence between the ground state and the $6P_{3/2}$ state ($\mathbf{k}_{420} = \mathbf{k}_{780} + \mathbf{k}_{776} - \mathbf{k}_{5,5}$) match with the wavevector of the amplified 420 nm light, strong coherent blue light is expected. As an example, a simple calculation of the dispersion of the refractive index is made for the 780 nm light. In Fig. 7.4 the phase of the 780 nm light is shown as a function of detuning for the two-level 5S–5P system. Power broadening and Doppler broadening are included. The refractive index is proportional to this phase. Although the refractive index of the 776 nm and effects of the two-photon transition are disregarded, this figure is a good representation of the strong dependence of the phase matching on detuning. Apart from the single photon resonances, the phase

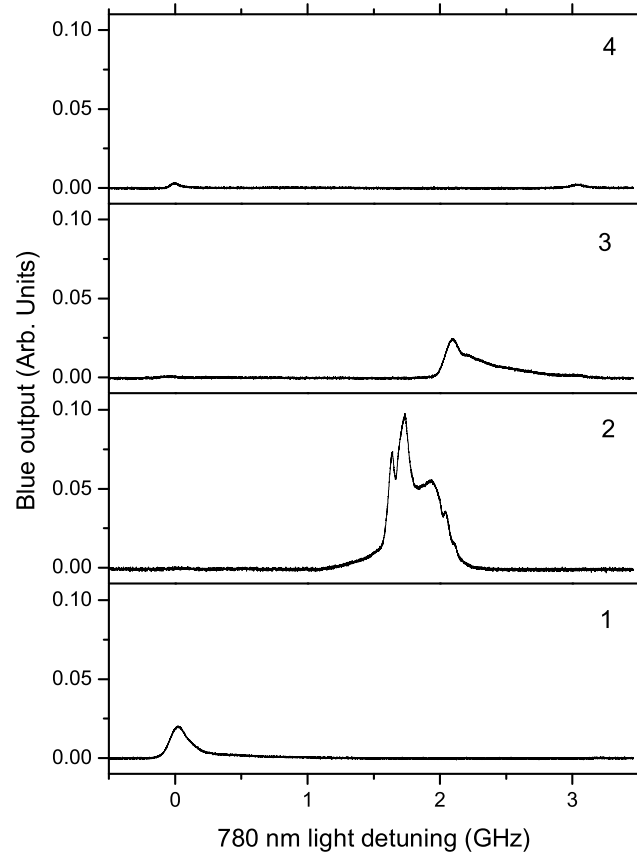


Figure 7.3: Blue output as a function of the 780 nm laser detuning. (1) is the blue light output when both IR lasers are close to their single photon resonances. This output is maximal when the temperature of the Rb vapor is approximately 150 °C. (2) is present when $\delta_{776} \approx -2$ GHz. This output has its largest amplitude when $T \approx 200$ °C. (3) is the blue output with $\delta_{776} \approx 1$ GHz and $T \approx 200$ °C. (4) is present when both IR lasers are close to resonance, and $T \approx 200$ °C. At this temperature small blue output is still present near the resonance frequency of the F=3 ground state hyperfine level, which coincides with output (1).

is also zero 2 GHz to the blue of the F=3 ground state hyperfine level resonance. At this detuning, blue output is large, which is most likely a result of a larger two-photon coupling, and better phase matching at this detuning. For this calculation we have assumed that the two-photon coherence is not optimal, i.e., population of the intermediate state $|a\rangle$ is not zero. Maximal two-photon coherence would result in strong blue output for all IR lasers detunings with their sum frequency close to two-photon resonance.

To study the degree of coherence and the spectral components of the blue radiation, a Fabry-Perot with a FSR of 1.5 GHz is used. This FSR is inconvenient since the ground state hyperfine splitting is 3 GHz, which makes it difficult to distinguish between hyperfine ground state levels. The etalon length should be decreased, preferably by more than a factor 2 to obtain a FSR higher than 3 GHz, which we could use to study all frequency shifts within one FSR. Because of difficulties in mode-matching the blue light and the

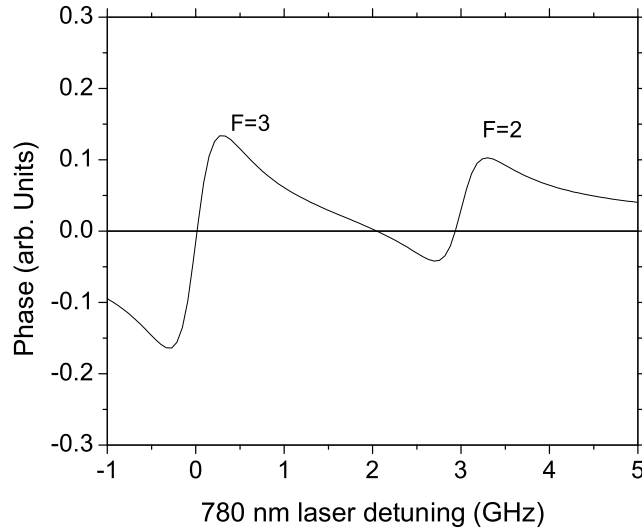


Figure 7.4: The phase of the 780 nm light as a function of its detuning. Power broadening and doppler broadening are included. The refractive index of the 780 nm light is directly proportional to this phase.

Fabry-Perot etalon, the distance between the mirrors is not changed and the 1.5 GHz etalon will be used to analyze the blue laser beam. The finesse of our etalon is approximately 100, which is sufficient to be able to resolve the largest hyperfine splittings of the upper levels.

In Fig. 7.5 the transmission of the FP etalon is shown for the most intense blue laser outputs. Blue outputs (1) and (2) of Fig. 7.3 consists mainly of one spectral component, with a small contribution of another line approximately 50 MHz shifted with respect to the main line. Outputs (3) and (4) seem to consist of only one spectral component with a broader transmission than the main transmission peak of output (1) or (2). This is possible when the frequency difference between two or more equally strong blue output lines can not be resolved by the etalon. This difference in spectra between on the one hand outputs ((1) and (2)), and on the other hand ((3) and (4)) is a consequence of the coupling to different hyperfine ground levels. Blue outputs (1) and (2) are due to a coupling of the $6P_{3/2}$ to the $F=3$ ground state and therefore is an amplification of spontaneous decay from hyperfine levels ($F=4,3,2$) of the $6P_{3/2}$ state. In contrast, blue output (3) and (4) are due to a coupling of the $6P_{3/2}$ to the $F=2$ ground state, and is an amplification of spontaneous emission from the hyperfine levels ($F=3,2,1$) of the $6P_{3/2}$ state. The frequency differences between the ($F=4,3$), ($F=3,2$), and ($F=2,1$) hyperfine levels of the $6P_{3/2}$ state are 39.275 MHz, 20.812 MHz, and 9.824 MHz, respectively [5]. This explains qualitatively why the frequency difference between lines coupled to the $F=2$ hyperfine level of the ground state is smaller than between lines coupled to the $F=3$ ground state hyperfine level.

Not only the spectral components of each blue output but also the mutual frequency shifts can be analyzed with the etalon. The shift between blue outputs (1) and (4) is

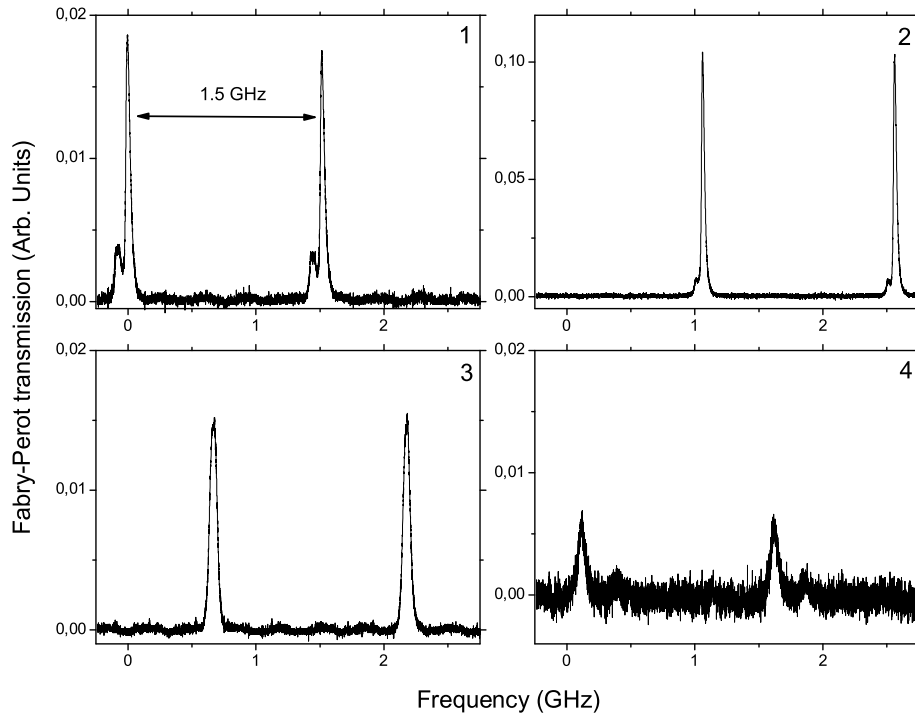


Figure 7.5: Fabry-Perot transmission while scanning the length of the cavity over almost two FSR. The transmission of the four most intense blue output beams is shown. The numbers correlate with the conditions given in Fig. 7.3.

$|\delta\nu \bmod 1.5 \text{ GHz}| = 0.1 \text{ GHz}$. Since they are both coupled to a different ground state hyperfine level, they should be shifted by 3 GHz, disregarding upper levels hyperfine splitting, which we can not determine with this etalon. We can assume this is the case. The off-resonance peaks (2) and (3) are shifted by $|\delta\nu \bmod 1.5 \text{ GHz}| = 1 \text{ GHz}$ and 0.6 GHz , respectively. Since the single-photon detunings are on the order of 1 GHz for both IR-lasers, the result of this detuning on the dressed state frequency shifts can not be neglected. We assume this results in strong frequency shifts compared to the on-resonance blue outputs.

Strong temperature dependence is also observed, especially for blue output (1) for which maximal output is measured at $T \approx 150 \text{ }^\circ\text{C}$. At higher T a sharp-edged decrease of blue side-fluorescence is observed near the back of the cell, moving to the front of the cell (i.e. towards the laser sources) when the temperature is increased. This stepwise decrease is shown in Fig. 7.6. Strong blue fluorescence is an indication of the presence of the $5.5 \mu\text{m}$ field. The higher the temperature the higher the Rb-density, and a larger absorption of the driving fields destroys the coherence, allowing generation of blue light only in the first couple of centimeters of the cell. When the gain stops, the blue light is not amplified, leading to lower output. For the blue output generated with driving fields off-resonance, the maximal output is measured at $T \approx 200 \text{ }^\circ\text{C}$. Although blue side-fluorescence is slightly

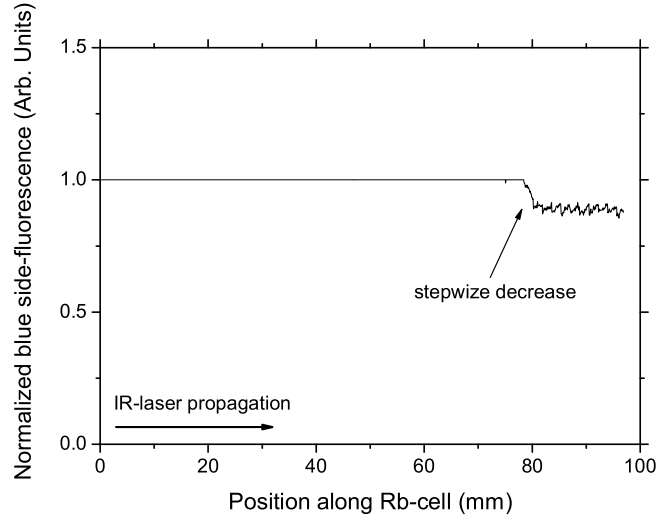


Figure 7.6: Stepwise decrease of side-fluorescence measured with a CCD-camera. A line profile over the blue side-fluorescence is shown. The CCD-pixels are saturated by the fluorescence emerging from the first part of the Rb-cell.

less than in the resonant case, the driving fields are less absorbed, allowing coherence over the entire length of the cell.

5 Conclusions

In conclusion, two infrared lasers at 780 nm and 776 nm create a large two-photon coherence in Rb resulting in up to $40 \mu\text{W}$ of coherent blue radiation, several times the power reached in the past. Blue output power is strongly dependent on the frequencies of the two IR-lasers due to phase matching. For better understanding the phase matching conditions, a thorough calculation of the phase matching of the two IR-lasers should be made.

The frequency spectrum of the blue light has been measured with a Fabry-Perot etalon (FSR ≈ 1.5 GHz). The blue output is highly coherent, spatially and temporally. We could distinguish between coupling to the $F=2$ and $F=3$ ground state hyperfine level. Furthermore, the blue output peaks, present when both IR-lasers are detuned from their single photon resonance, are frequency shifted compared to the on-resonance peaks.

This technique is a very efficient way to produce blue light, and can possibly replace frequency doubling crystals in the future. Other wavelengths can be produced in this way by studying cascade schemes in other elements.

References

- [1] M.D. Lukin, P.R. Hemmer, and M.O. Scully, *Adv. At., Mol., Opt. Phys.* **42**, 347 (2000).

- [2] D.J. Fulton, S. Shepherd, R.R. Moseley, B.D. Sinclair, and M.H. Dunn, Phys. Rev. A **52**, 2302 (1995).
- [3] E.S. Fry, X.Li, D. Nikonov, G.G. Padmabandu, M.O. Scully, A.V. Smith, F.K. Tittel, C. Wang, S.R. Wilkinson, and S. Zhu, Phys. Rev. Lett. **70**, 3235 (1993).
- [4] A.S. Zibrov, M.D. Lukin, L. Hollberg, and M.O. Scully, Phys. Rev. A **65**, 051801(R)(2002).
- [5] E. Arimondo, M. Inguscio, and P. Violino, Rev. Mod. Phys. **49**, 31 (1977).

Summary

Direct-write atom lithography is a technique in which highly periodic nanostructures are directly deposited on a substrate by patterning an atomic beam with a standing light wave, tuned near a resonance frequency of the corresponding atom.

In this thesis an extension of this technique for the production of ferromagnetic nanostructures is investigated. Of all ferromagnetic elements Fe is the most suitable to perform atom lithography. Light with a wavelength of 372 nm is needed to produce Fe nanostructures by atom lithography. Also, the atomic beam should be highly collimated, for which laser cooling is commonly used.

For this purpose, a frequency doubled Ti:S laser tuned to 744 nm is constructed, capable of producing more than 100 mW of light at a wavelength of 372 nm. Laser cooling requires a laser with a frequency stability better than the natural linewidth of the atom. To meet this requirement, the laser is locked on the atomic transition by means of polarization spectroscopy on a hollow cathode discharge cell. The discharge cell produces a sufficient density of ground state Fe atoms at a temperature which is more than a factor of two lower than the temperature necessary to produce that density in a thermal cell. With this technique the laser is locked stable within 0.2 MHz for hours.

A laser cooling simulation based on the semiclassical approach is presented. Although the intention was to simulate laser cooling of Fe with this code, for the commonly used $\pi^x\pi^y$ polarization gradient configuration an analysis of the simulation results shows that the semiclassical approach is only valid for transitions with recoil parameters ε_r on the order of 10^{-4} or less. For the standard laser cooling transitions only the transitions in Rb and Cs satisfy this condition. A drastic reduction in calculation time compared to quantum Monte-Carlo calculations is to be expected for these transitions by implementing an analytical approach to the long-term contribution of the diffusion coefficient. For Fe, full quantum Monte-Carlo calculations are necessary.

Laser cooling of Fe on the 372 nm transition has been studied experimentally. This transition, although the only one realistically available, is far from perfect for laser cooling, as it is not a fully closed transition: it has a leak ratio of approximately 1/240 to other states. Nevertheless, a collimation of $\alpha_{RMS} = 0.17$ mrad could be achieved by laser cooling. However, contrary to the normally obtained central beam flux increase, the ground state atom flux decreased to approximately 70 % of the non-cooled value.

Because of both the complexity of the laser cooling setup and the restrictions in performance, we have also attempted to produce Fe nanostructures without using laser cooling techniques, but simply relying on geometrical collimation of the atomic beam. In this way, Fe nanolines are deposited with a pitch of 186 nm, a FWHM width of 50 nm, and a height of up to 6 nm. This opens the way for applying direct-write atom lithography to a wide variety of elements. In a MOKE (Magneto-Optical Kerr effect)-setup we are able to verify that the deposited Fe-layer is ferromagnetic. However, the magnetic anisotropy due to the presence of the nanolines can not be detected with a MOKE-setup or a MFM (Magnetic Force Microscope). In contrast, the magnetization of background-free nanolines, deposited through a mechanical mask with a pitch of 744 nm and a FWHM of

150 nm, is visualized by MFM. This shows that size and background of the standing wave produced nanolines limits the ability to measure the influence of the nanolines on the magnetization of the Fe-layer.

At the University of Melbourne, a novel highly efficient technique for frequency up-conversion is studied. This technique is more efficient by several orders of magnitude compared to conventional frequency up-conversion in non-linear crystals. Up to 40 μW at a wavelength of 420 nm could be produced by two low-power lasers (15 mW) at 780 nm and 776 nm using a five-level lasing-without-inversion scheme in rubidium vapor.

Samenvatting

Met atoom lithografie worden strikt periodieke nanostructuren direct op een oppervlak geschreven. Dit gebeurt door een atoombundel te structureren d. m. v. een staande lichtgolf, die dicht bij de resonantiefrequentie van het atoom is afgestemd.

Dit proefschrift beschrijft de uitbreiding van deze techniek voor de productie van ferromagnetische nanostructuren. Van alle ferromagnetische elementen is ijzer het meest bruikbare in atoom lithografie. Voor de productie van ijzer nanostructuren m. b. v. atoom lithografie is licht nodig met een golflengte van 372 nm. Ook moet de atoombundel heel goed gecollimeerd worden. Daar zorgt laserkoeling voor.

Voor het bereiken van deze doelstellingen is een frequentieverdubbelde Ti:S laser ontwikkeld die meer dan 100 mW bij 372 nm produceert. Laserkoeling eist een frequentiestabiliteit van de laser die beter is dan de natuurlijke lijnbreedte van het atoom. Om dit te bereiken wordt de laser op de atomaire overgang gestabiliseerd met behulp van polarizatiespectroscopie op een holle kathode ontladingslamp. Deze lamp produceert voldoende ijzer atomen in de grondtoestand bij een temperatuur die meer dan een factor twee lager ligt dan de temperatuur nodig om dezelfde dichtheid te produceren door Fe thermisch te verdampen. Het resultaat is een laser die binnen 0.2 MHz gestabiliseerd is over een tijdsperiode van enkele uren.

Een laserkoeling simulatie is ontwikkeld, gebaseerd op de semiklassieke benadering. Hoewel het in de eerste plaats de bedoeling was om laser koeling van ijzer met dit programma te simuleren, laten de simulatieresultaten zien dat deze simulatie voor de gebruikelijke $\pi^x\pi^y$ configuratie enkel geldig is voor recoil parameters ε_r in de orde van 10^{-4} of kleiner. Enkel Cs en Rb voldoen aan deze voorwaarde. Door een analytische benadering van de lange-termijn contributie aan de diffusiecoëfficiënt in te voeren, wordt voor deze overgangen een drastische verkorting van de rekentijd verwacht in vergelijking met quantum Monte-Carlo berekeningen. Voor Fe blijven quantum Monte-Carlo berekeningen noodzakelijk.

Laserkoeling op de 372 nm overgang van Fe is experimenteel bestudeerd. Hoewel deze overgang de enig bruikbare overgang in Fe is, is deze overgang ver van perfect voor het laserkoelen van Fe omdat er een lek van 1/240 naar andere toestanden optreedt. Ongeacht het lek kan toch een collimatie van $\alpha_{RMS} = 0.17$ mrad bereikt worden. In tegenstelling tot de verwachte fluxwinst bij laserkoelen, daalt de flux van grondtoestand atomen tot 70 % van de initiële flux.

Door de complexiteit van de laserkoelingsopstelling en de beperkingen in prestatie hebben we geprobeerd Fe nanostructuren te groeien zonder gebruik te maken van laserkoeling, maar door te vertrouwen op de geometrische collimatie van het systeem. Op die manier zijn Fe nanolijnen gedeponed met een periode van 186 nm, een FWHM van 50 nm, en een hoogte van 6 nm. Dit maakt de weg vrij voor het gebruik van atoom lithografie voor een groot aantal elementen. In een MOKE (Magneto-Optische Kerr effect)-opstelling wordt geverifieerd dat de gedeponede ijzerlaag ferromagnetisch is. Desondanks, magnetische anisotropie als gevolg van de individuele lijnen kan echter niet aangetoond worden met de MOKE-opstelling of een magnetische kracht microscoop (MFM). In contrast wordt de magnetisatie van achtergrond-vrije nanolijnen, gedeponed door een mechanisch masker

met een periode van 744 nm en een FWHM van 150 nm, wel gevisualiseerd met behulp van een MFM. Dit toont aan dat de achtergrond en grootte van de nanolijnen het meten van de invloed van de nanolijnen op de magnetisatie van de Fe-laag bemoeilijken.

Aan de Universiteit van Melbourne is een vernieuwende techniek voor efficiënte frequentieverhoging bestudeerd. Deze techniek is vele grootte-orde efficiënter dan conventionele frequentieverhoging in niet-lineaire kristallen. Tot 40 μW aan licht bij 420 nm kon geproduceerd worden met twee laag-vermogen diode lasers (15 mW) met respectievelijke golflengtes van 780 nm en 776 nm door gebruik te maken van een laser-zonder-inversie systeem met vijf niveaus in een rubidium gas.

Dankwoord

Hoewel je tijdens een promotie eenzame uren in het lab of achter de pc doorbrengt, kan je een proefschrift niet zonder de hulp van anderen afwerken.

Veel dank ben ik verschuldigd aan mijn eerste promotor Ton van Leeuwen. Hij is een omuitputtelijke bron van kennis bij het oplossen van fysica- en computerproblemen. Mijn tweede promotor Herman Beijerinck dank ik voor zijn krachtdadige en toekomstgerichte aanpak en het verbreden van mijn visie, zowel op fysica als non-fysica gebied. Peter van der Straten, gedoopt tot copromotor, wil ik danken voor zijn enthousiasme tijdens zijn wekelijkse bezoeken, zijn kritische blik en het grondig lezen van dit proefschrift. Edgar Vredenburg dank ik voor de discussies over laserkoeling, zijn hulp in het lab en het werk aan de simulatieprogramma's die ik veelvuldig gebruikt heb tijdens mijn promotie.

Het belangrijkste voor een experimenteel promovendus is een werkende opstelling. Zonder Louis van Moll en Jolanda van de Ven zou de nano-opstelling nooit zo gesmeerd gelopen hebben. Voor de ontelbare uren dat ze in de werkplaats mijn soms onleesbare tekeningen tot iets bruikbaar hebben weten om te toveren ben ik hen erg dankbaar.

Met mijn collega-promovendus Edwin te Slighte heb ik vooral veel frustratie gedeeld in het opbouwen van de nano-opstelling. Ondanks niet werkende bronnen en kapotte lasers vond ik het een plezier om met je samen te werken.

Afstudeerder Rodolf Herfst ben ik veel dank verschuldigd voor zijn werk aan de laserkoeling simulatie. Ook wil ik Leon van Dijk bedanken voor zijn metingen aan de nanolijnen, Murat Bozkurt voor het werk aan de ontladingslamp en Richard van der Stam voor het ontwerp en de constructie van het depositievat en samplehouders. Mijn collega's bij AQT: Kenian Domen, Maarten Jansen, Bert Claessens, Erik van Kempen, Veronique Mogendorff, Bout Marcelis, Alquin Stevens, Gabriel Taban, Servaas Kokkelmans, Simon Kuppens en Wilbert Rooijackers dank ik voor de toffe en stimulerende sfeer.

Het was een plezier om de kamer van Rina Boom binnen te wandelen, zelfs nadat ze naar de verste uithoek van het gebouw verhuisd was. Mijn administratieve rompslomp handelde ze met de glimlach af.

I would like to thank Rob Scholten and Luke Maguire for their work on the nano-setup during their stay in Eindhoven. Thanks to them and all their colleagues my visit to the optics group at the University of Melbourne was a very pleasant experience.

Last but not least wil ik mijn ouders en Katrien bedanken voor de steun gedurende de voorbije vier jaar en voor de moeite om een 'saaie' natuurkundige sociale vaardigheden bij te brengen.

Curriculum Vitae

- 2 december 1978 Geboren te Lommel, België
- 1990-1996 Algemeen Secundair Onderwijs,
Sint-Lambertuscollege te Bilzen, België
- 1996-1998 Studie Natuurkunde,
Limburgs Universitair Centrum te Diepenbeek, België
- 1998-2001 Studie Technische Natuurkunde,
Technische Universiteit Eindhoven,
doctoraal examen juli 2001
- 2001-2005 Assistent-In-Opleiding,
Experimentele Atoomfysica en Quantumelektronica,
Faculteit Technische Natuurkunde,
Technische Universiteit Eindhoven